Modelling of Quasi Steady Detonations with Inert Confinement

Sarthak Lalchandani

Thesis submitted to the University of Ottawa
in partial fulfillment of the requirements for the
Master of Applied Science in Mechanical Engineering

Department of Mechanical Engineering
Faculty of Engineering
University of Ottawa

Abstract

In this thesis, we address the problem of steady propagation of a gaseous detonation weakly confined by an inert gas. The effect of the lateral divergence is modelled using Watt's Straight Streamline Approximation and a newly derived simpler nozzle model in a hydrodynamic average description. The prediction of the models was compared against the detonation velocity data obtained numerically by Mi et al and Reynaud et al. Very good agreement is found for weakly stable detonations at low activation energy with all models. These models, however, fail to capture the dynamics of unstable gaseous detonations characterized by delayed energy release, long induction lengths and higher activation energies. This inconsistency is treated by different models for the macroscopic kinetics: the underlying chemical kinetics model applicable for a laminar formulation, an effective kinetic rate adjustment to account for the detonation thickening owing to the cellular instability and a new ignition delay distribution model conditioned on the distribution of shock temperatures at the shock. The study illustrates that the reaction zone thickening of detonation waves and the delayed energy release are responsible for its limits. Future work should be extended to incorporate more accurate sub-cellular models to capture other effects, such as the ignition of gases via turbulent mixing in very irregular detonations.

Acknowledgements

I want to give my special thanks to my supervisor Dr Matei Ioan Radulescu, for giving me the chance to be part of his research team and for allowing me to conduct independent research. His mentoring, advice and guidance were essential for my improvement. His dedication to science and engineering set the bar high for us who worked with him.

I would also like to thank my co-supervisor, Dr Zekai Hong. He helped me keep my morale up for the overall length of my program and provided many good pieces of advice so that I keep working in the right direction.

My sincere thanks to all who helped me during my master's study. Special thanks to the Detonation and Reactive Dynamics Laboratory team for helping and continuously supporting me.

I would also like to thank the National Research Council of Canada (NRCC) for supporting this research financially.

Last but not least, I would like to thank my family for continuously supporting me and providing me with the utmost love and care.

Contents

List of Figures

List of Tables

Nomenclature

Acronyms

CDF Cumulative Density Function

CJ Chapman-Jouget

DSD Detonation Shock Dynamics

IGD Ignition Delay Model

NS Numerical Simulations

ODE Ordinary Differential Equation

OS Oblique Shockwave

PDE Pulse Detonation Engine

PDF Probability Density Function

PM Prandtl-Meyer Expansion

*Q*1*D* Quasi-one-dimensional

RDE Rotating Detonation Engine

SSA Straight Streamline Approximation

SSM Straight Streamline Model

VN von-Neumann

VSA Variational Streamline Approximation

WK Wood-Kirkwood

ZND Zel'dovich von-Neumann Döring

Subscripts

0 Initial state

1 Final state

avg Average value

cr Critical value

f Shock-front

i Inert layer

ig Ignition delay

n Normal component

r Reactive layer

s	Shockwave
t	Transverse component

Symbols

γ	Ratio of specific heats
λ	Reaction progress variable
ψ	Stream function
ρ	Density
d	Diameter
E_a	Activation energy
h	Height
k	Pre-exponential factor
M	Mach number
p	Pressure
Q	Heat release per unit mass of reactants
R	Gas constant of the mixture
T	Temperature
u	Transverse flow velocity

v Longitudinal flow velocity

Z Acoustic impedance ratio

Chapter 1

Introduction

1.1 Background

Detonation is a self-sustained combustion wave comprised of a supersonic shock wave travelling in the reactive medium followed by the region of exothermic chemical reactions [1]. Gaseous detonations travelling inside a tube or in a confined system, where the confiner is an inert gas, face energy losses. The losses can come from area increase of the reactive channel [2, 3], by the inclusion of a boundary layer in the reaction zone [4, 5], friction losses [6] and heat losses [7] to the confiner material. These losses manifested as lateral area divergence in the reaction zone of such detonations govern their propagation velocity and are responsible for their attenuation under critical conditions [8, 9]. The quantification of the losses is vital in achieving a steady detonation as it finds its applications in novel propulsion devices such as Rotating Detonation Engines (RDEs) or designing a

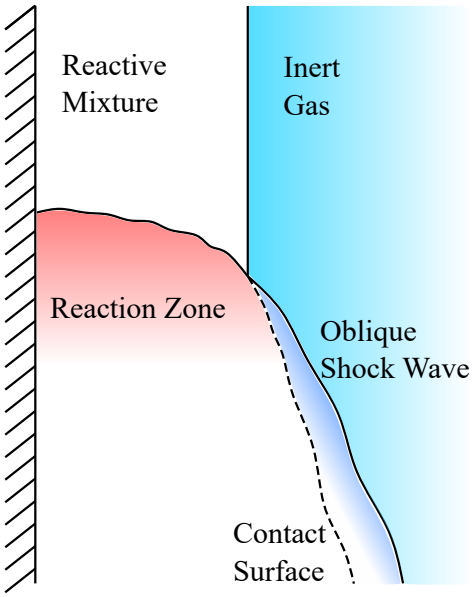

Figure 1.1: Schematic of a cellular detonation propagating in the weakly confined channel of a reactant mixture.

system where destructive vapor cloud explosions can be avoided. The complication arises in understanding their complicated dynamics as the multi-dimensional instabilities are generated due to the cellular structure of such detonations.

1.2 Problem Definition

The typical structure of a weakly confined gaseous detonation is shown in Figure 1.1. Here the shock front is advancing in the reactive mixture, followed by the reaction zone structure. The weak confinement allows the lateral deflection of the reacting gases due to the high pressure generated in the reaction zone. An oblique shock wave is formed inside the inert media to match the pressure on both sides

of the product-inert interface, labelled ”contact surface” in Figure 1.1.

The velocity with which a detonation travels is an important property that ultimately defines its strength. As explained, moderately confined detonations experience the expansion of reaction zone structure due to the weak confiner that decreases their velocity from the ideal Chapman-Jouget (CJ) velocity. The fraction of energy lost to the confiner increases as we decrease the charge width. The globally curved wavefront also aids in lateral flow divergence of reactants in the reaction zone structure. This work aims to model the effect of various parameters such as charge thickness and reactivity of mixture on the steady propagation velocity of weakly confined detonations by analytical models.

1.3 Motivation

A detonation wave consists of a lead shock and a reaction-zone structure. The chemical energy stored in the chemical bonds of the reactive material is transformed into the kinetic and internal energy of products. This rapid release of energy is the motivating idea behind the ongoing research and development of novel propulsion systems, such as Rotating Detonation Engines (RDEs) and Pulse Detonation Engines (PDEs) [10, 11, 12, 13, 14, 15, 16]. An RDE is a unique engine that utilizes an annular combustion chamber where a detonation wave travels circumferentially, as illustrated in Figure 1.2. As shown in Figure 1.3, the detonation wave in an RDE is laterally constrained by the previous cycle’s combustion products, leading to a complicated detonation/shock structure where the detona-

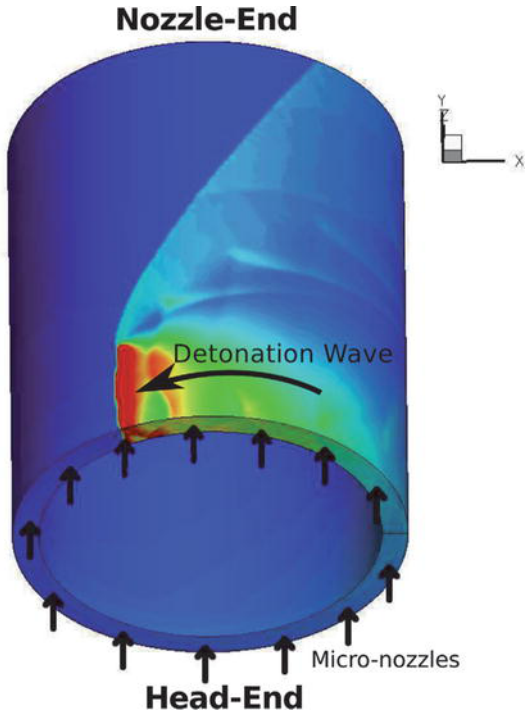

Figure 1.2: Sketch of a rotating detonation wave structure (from Reference [11]).

tion wave travels with a velocity deficit. The structure of the detonation wave restricted by the product gases resembles the problem of weakly confined detonations, as explained in section 1.2.

The use of hydrogen gas as a substitute for fossil fuels is growing daily. However, because hydrogen has low ignition energy and high reactivity, it is critical to understand its explosion safety. The unintentional release of light and flammable gas in a closed containment can result in the accumulation of a bed of reactive mixture at the top of the room, confined by air on its side. Ignition of such a reactive layer can result in deflagration-to-detonation transition (DDT), which can cause significant structural damage. Thus, it is critical to understand the underly-

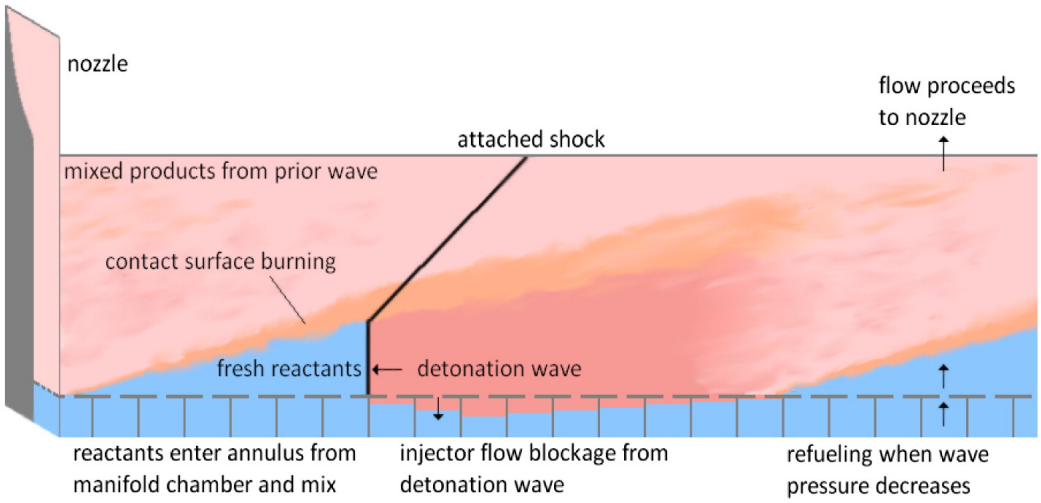

Figure 1.3: Sketch of a detonation wave travelling in an unwrapped RDE (from Reference [13]).

ing mechanisms that drive these weakly confined detonations, which can help in the designing of fail-safe strategies to avoid such incidents.

1.4 State-of-the-art

Eyring and colleagues [17] were among the first researchers to mathematically model the relationship between the velocity of a confined detonation wave propagating axially in a cylindrical charge with the charge's limited radius. Wood and Kirkwood were the first to propose the link between detonation velocity and shock front curvature [18]. Another essential theory in modelling the phenomena is Detonation Shock Dynamics (DSD), developed by Bdzil and Stewart [19]. DSD is a name given to a set of theories and experiments that attempt to analyze the dynamics of detonations, especially those with minor curvature compared to

the reaction zone length. In most cases, the flow of reactants after the shock is governed by the two-dimensional reactive Euler equations in the shock-attached reference frame. The DSD also addresses the unsteady effects and the evolution of detonation dynamics for unsteady cases. An overview of other different yet relevant analytical models is given in [20].

Sommers [21] developed a one-dimensional model to predict the intensity of expansion of the reaction zone structure due to weak confiner by matching the flow conditions at the contact surface between the inert gas and the reacted products by shock-polar analysis. Watt et al. developed a mathematical model based on the fluid-streamline approach of reactive gas flow across the detonation front to study the dynamics of non-ideal detonations [22]. The model adopts the steady reactive Euler equations in streamline coordinates (ψ, y) and assumes straight streamlines. For a given detonation speed, the governing equations are integrated from the charge axis for increasing ψ until the critical streamline deflection angle is reached. While approximate, Watt and colleagues demonstrated that the Straight Streamline Approximation (SSA) model could accurately predict the detonation velocity for condensed-phase explosives, compared to the numerical solutions and the DSD projections, for fundamental pressure-dependent kinetics. Watt's SSA model can also incorporate more complex chemical models for integration along each stream tube, thus opening avenues for modelling unstable detonations.

1.5 Statement of Work

In the present study, we wish to test the performance of the Straight Streamline Approximation (SSA) model in predicting the dynamics of cellular gaseous detonations that are weakly confined by an inert gas. It is done by adopting the SSA model to gas-phase characteristics where the rate-law is approximated as Arrhenius 1-step. We also develop a simpler Quasi 1-D model that can be useful for engineering purposes. Recently, Reynaud et al. [23] and Mi et al. [24] have computed detailed numerical simulations of cellular detonations. The model predictions will be validated against these results. A total of seven cases are studied for both models – a) $E_a/RT_0 = 10, 20, 30$ and 38.23 for $Q/RT_0 = 23.81$ and $\gamma = 1.333$, and b) $E_a/RT_0 = 10, 20$ and 30 for $Q/RT_0 = 50$ and $\gamma = 1.2$.

While the agreement will be shown to be very good for stable detonations, the deviation of the models for more unstable detonations, characterized by high reduced activation energies, can be quantitatively reconciled by the influence of the cellular structure on detonation's global reaction zone structure. This deviation is addressed by two models developed in this study - a) the empirical model that incorporates the lengthening of the reaction zone in such detonations and b) the Ignition delay model that considers the local velocity fluctuations that arise due to the cellular structure of gaseous detonation.

In summary, the present study attempts to address the effect of losses from the confiner and its interaction with the reaction zone structure of gaseous detonations by analytical modelling. Particularly tackling the question - Can macro-level prop-

erties of gaseous detonation confined by non-reactive material be predicted by simple models, which inherently incorporate physics of the micro-level details like -cellular structure, delayed energy deposition and unsteady character of such detonations?

1.6 Outline of this Study

The first chapter introduces the physical problem in this thesis and the different techniques employed to address the issue. Next, an overview of fundamental detonation theories is provided, followed by a relevant literature review of experimental and numerical studies on the problem. The third chapter is dedicated to developing the Straight Streamline Approximation (SSA) model. Then, the development of a simpler, Quasi-one-dimensional (Q1D) model is presented. The models to account for the reaction-zone thickening that arises due to the cellular structure of gaseous detonations are discussed in the fifth chapter. Finally, relevant conclusions are drawn out from the study and possible future avenues are discussed.

Chapter 2

Literature Review

2.1 Introduction

This chapter presents a literature review of the fundamentals of detonation theory, meant primarily to the non-specialist, followed by a more focused account of previous experimental and numerical simulations of the problem studied in the present thesis.

2.2 CJ Theory

Chapman [25] and Jouget [26] independently presented the initial theory of the stationary detonation model and treated it as a discontinuity, as shown in Figure 2.1. The criterion described by Chapman [25], which addresses the stationary detonation model, is when the Rayleigh line is tangent to the detonation branch of

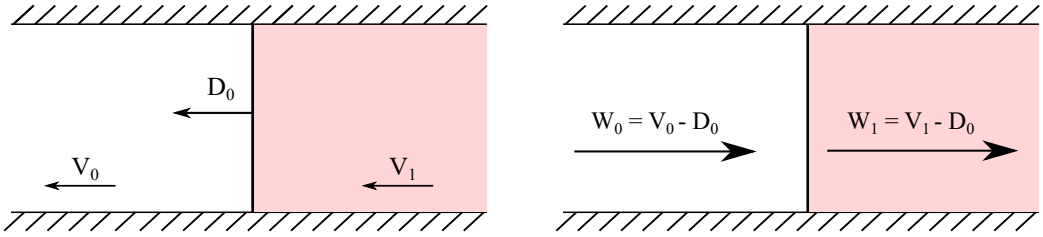

(a) Laboratory Reference Frame (b) Shock attached Reference Frame

Figure 2.1: Detonation as a discontinuity in (a) laboratory reference frame with D_0 velocity and stationary in (b) shock attached reference frame.

the Rankine-Hugoniot curve, as shown in Figure 2.2. Simultaneously, Jouget [26] confirmed the existence of a sonic plane that separates this shock-flame complex from any downstream flow disturbances in his solution to the problem. Coincidently, the independent methodologies derived by Chapman and Jouget gave the same answer to the problem, and this criterion is then termed as Chapman-Jouget (CJ) criterion.

2.3 ZND Model

Zel'dovich [27], von Neuman [28], and Döring [29] extended the CJ Theory by providing a model for the reaction zone structure. As depicted in Figure 2.3, the definition of detonation wave structure in ZND theory is as follows: Induction and recombination zones comprise the reaction zone between the shock wave and the CJ state. The purpose of the shock wave is to compress the reactants and elevate their temperature and pressure initially. Free radicals are created in the induction zone characterized by very little change in thermodynamic properties across the

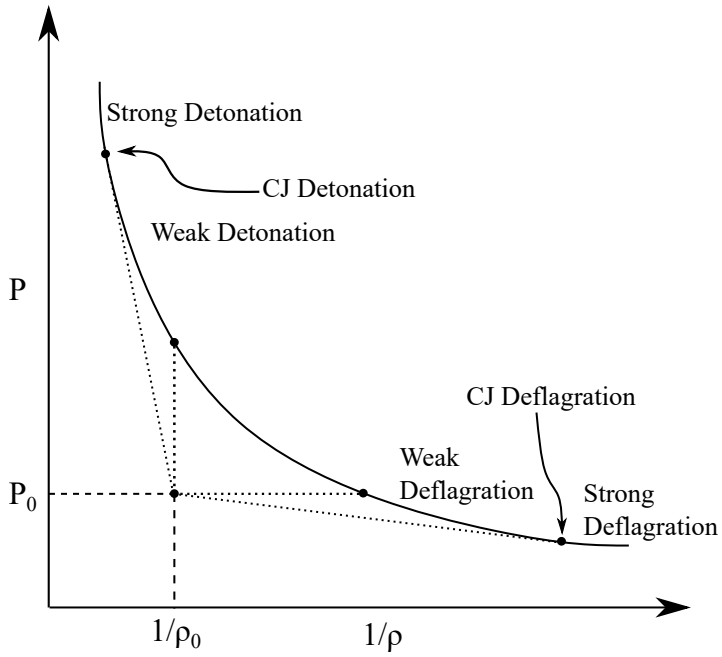

Figure 2.2: The Rankine - Hugoniot curve.

area. It is followed by a recombination zone where these free radicals recombine to create products and release the chemical energy of the reactive compound. The temperature rises further due to chemical energy being released rapidly within the reaction zone, along with a corresponding drop in pressure and density. Finally, the burning products, responsible for the self-sustainability character of detonation, expand and drive the supersonic combustion wave's whole structure.

The state just after the shock wave in the ZND model is called the von-Neumann (VN) state. The shock jump relations, obtained from solving the Rankine-Hugoniot curve and Rayleigh line, given by equations (2.1) and (2.2) and the ideal gas equation ($pv = RT$), can compute the pressure, density, and temperature at that state.

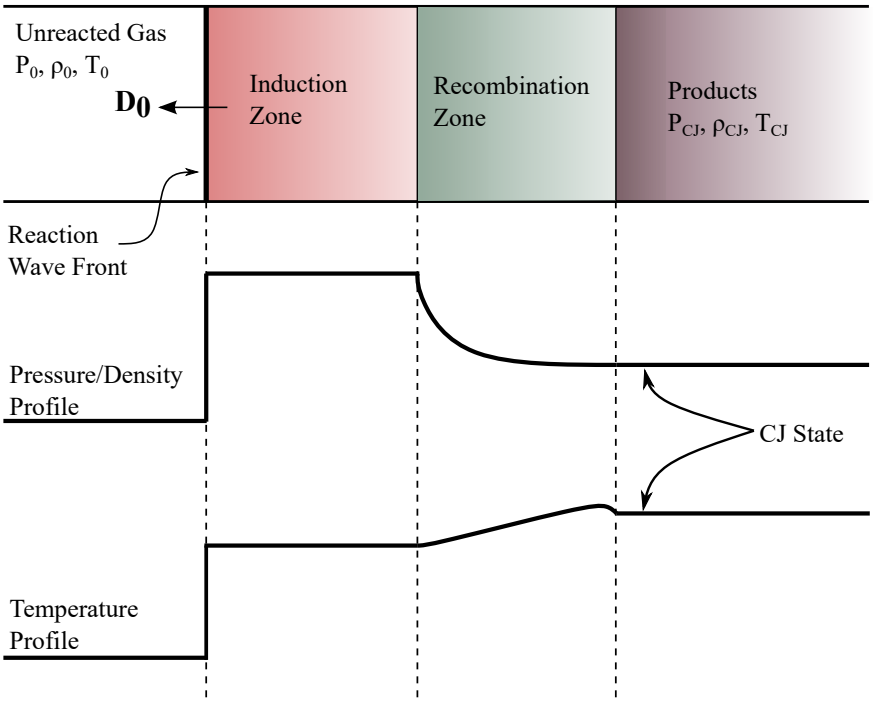

Figure 2.3: Schematic of pressure, density, and temperature profiles for a steady one-dimensional ZND detonation wave that goes from right to left in a laboratory frame of reference.

$$\frac{p_{VN} - p_0}{p_0} = \frac{2\gamma(M^2 - 1)}{(\gamma + 1)} \tag{2.1}$$

$$\frac{\rho_{VN}}{\rho_0} = \frac{(\gamma + 1)M^2}{(\gamma - 1)M^2 + 2} \tag{2.2}$$

The law of conservation of mass, momentum, and energy, along with the calorific equation of state, presented in equations (2.3), (2.4), (2.5) and (2.6), forms the governing equations. These equations are then coupled with the rate of reactant burning as presented in equation (2.7). The initial condition for this set of ODEs is the von-Neumann state. An assumption on the velocity or, say, Mach Number of the detonation wave has to be made such that the sonic flow velocity in the CJ state is obtained, thus making it an eigenvalue problem. Here $\gamma = C_p/C_v$ is the ratio of specific heats, M is the Mach number with which detonation travels in fresh unreacted gas, Q is total chemical energy released per unit mass, λ is the reaction progress variable, and W is the reaction rate law.

$$\frac{d}{dx}(\rho v) = 0 \tag{2.3}$$

$$\frac{d}{dx}(p + \rho v^2) = 0 \tag{2.4}$$

$$\frac{d}{dx}(h + \frac{v^2}{2}) = 0 \tag{2.5}$$

$$h = \frac{\gamma}{\gamma - 1}\frac{p}{\rho} - \lambda Q \tag{2.6}$$

$$\frac{d\lambda}{dt} = W/v \tag{2.7}$$

2.4 Structure of Detonation

The actual structure of gaseous detonation is different from what Zel'dovich, von Neuman, and Döring put forth in the literature. The actual gaseous detonation possesses the cellular configuration, including Mach shock, triple point, incident shock, shear layer, transverse shocks and dense unburned reactant pockets present downstream, distant from the initial shockwave [30, 31, 32, 33, 34, 35]. As shown in Figure 2.4, the series of unsteady and non-uniform Incident and Mach shocks make up the structure of the lead front.

The incident shock is the part of the lead front present inside the later part of the cell, whereas Mach shock, characterized by higher velocity and strength, is formed just after the triple point collision. Transverse shocks originating from the triple point can be reactive or non-reactive, depending on their intensity. The shear layer, which separates the reacted gases processed by the more robust Mach stem from the unburned gases processed by the weaker incident shock, also emerges from the triple point. The shear layer is easily noticeable due to the high-density difference prevalent across it and exemplified by little whirls, as shown in Figure 2.4. The pulsating locus of the triple point, which moves up and down the width of the channel of the reactive mixture, is responsible for propelling the lead shock front. The evolution of the wavefront characterized by triple point collisions and the introduction of new Mach stems is evidenced in Figure 2.5.

The strength of the shock consistently decays across the length of the cell. Thus, the change in ignition delays is dramatic as they are exponentially dependent upon

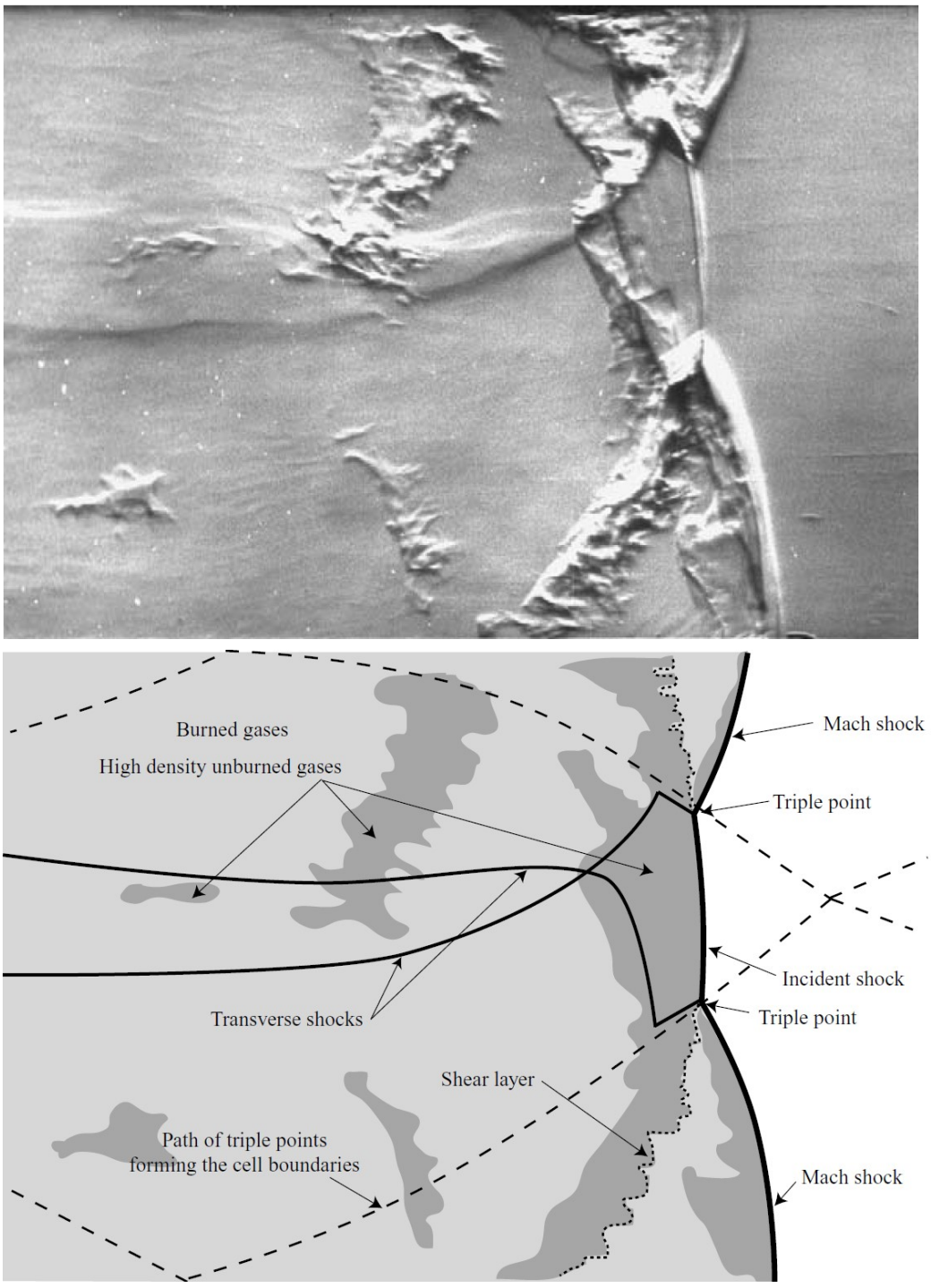

Figure 2.4: Schlieren photograph of detonation structure in a $CH_4 + 2O_2$ mixture at 3.4 kPa initial pressure in a 25-mm by 100-mm cross-section channel, and explanatory sketch. (From Reference [36])

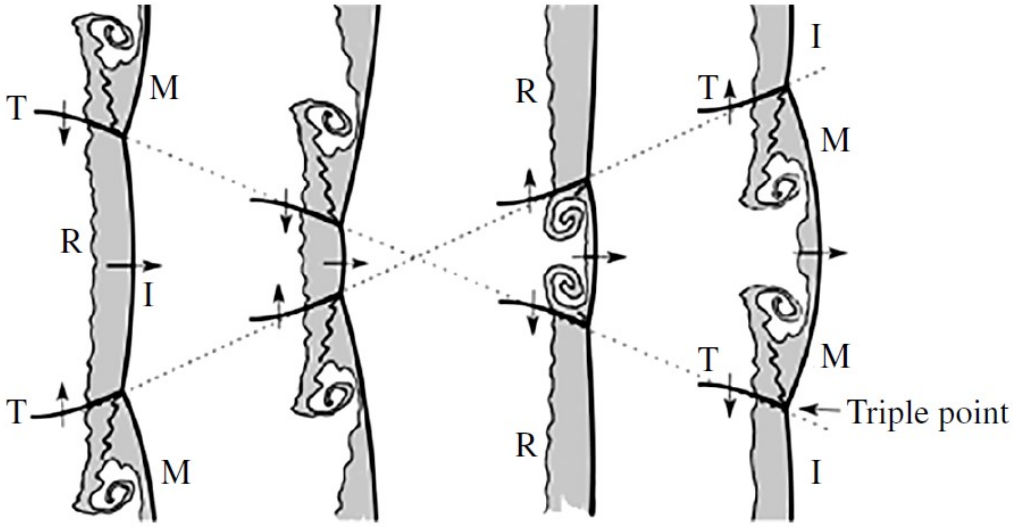

Figure 2.5: Sketch showing a triple-point collision process. Various waves indicated are the incident shocks (I), Mach shocks (M) and transverse shocks (T). The extents of the turbulent reaction zones (R) are also shown (From Reference [37]).

the temperature of the reactant mixture, which has just passed through the lead shock [1, 36, 37, 38, 39]. The unreacted pockets of gases are formed due to the exponential sensitivity of the reaction rates to the temperature of the shocked gases. The usual norm for most steady gaseous detonations is having non-reactive and weak transverse shock behind the incident shock. The two weak shocks are insufficient to shorten the ignition delay of unreacted gases, and thus they remain dormant in the flow field for much longer. The movement of the triple points causes this lump of unreacted gases to detach from the shock front as they collide. Numerous experiments and numerical simulations show that these island-shaped pockets of unreacted reactants burn via surface turbulent waves rather than auto-ignition [37].

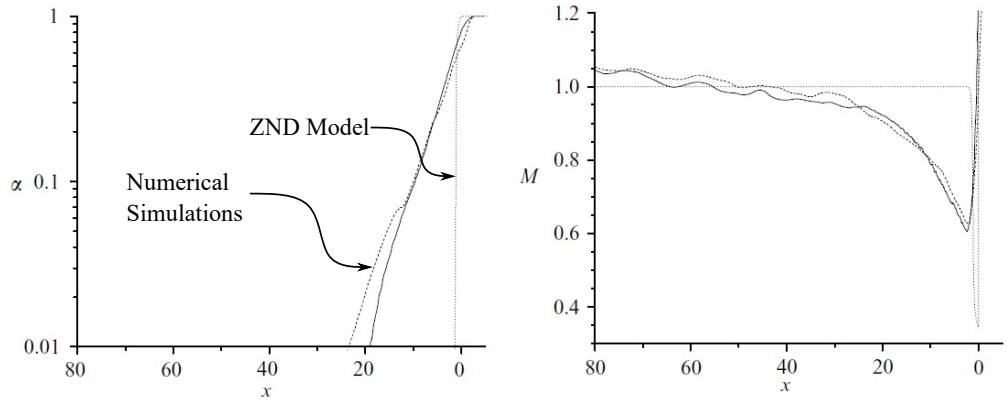

Figure 2.6: Favre-averaged Reactant concentration and Mach number profiles for θ_o = 63.7; broken lines, case A; (solid lines), case B; dotted lines, ZND model (From Reference [36])

The rate of burning of reactants of a cellular detonation obtained from numerical simulation for a particular case defined in [36] is shown in Figure 2.6. The relevant lengthening of the reaction zone and hydrodynamic thickness can be observed compared to the ZND solution, shown by dotted lines.

2.5 Experiments of Confined Gaseous Detonations

Sommers was the first to systematically study the detonation propagation in a charge bounded by an inert gas [21, 40]. He used a rectangular tube with a test section confined by glass on two sides and metal on one side, which acts as a centerline symmetry for the detonation, as shown in Figure 2.7. This inquiry revealed some essential characteristics of such a system, as shown in Figure 2.7. The one thing to note here is that Sommers' observations are limited to the field of view,

having 1.8 times the width of the rectangular tube in the longitudinal direction. He concluded that a one-dimensional nature of gaseous detonation waves in rigid tubes was not observed when the elastic boundary was present. The presence of curvature and quenching of such detonations were attributed to the hydrodynamic nature of the confining layer.

Dabora et al. extended Sommers's work by conducting several quantitative similar experiments [41, 42]. The experimental design developed by Dabora and his peers is presented in Figure 2.8. The reactive charge is separated by the non-combustible gases by a thin soap film of about 250 Å in thickness, and the explosive mixture chosen is H_2-O_2 with varying volumetric ratios. Moreover, the confiner material is selected as nitrogen. The steady velocity of detonation for a stoichiometric mixture of hydrogen and oxygen with varying channel widths is shown in Figure 2.9; the solid lines in Figure 2.9 correspond to an analytical model suggested by Dabora [41].

Dabora and his peers concluded that the velocity deficits of gaseous detonations bounded by compressible inert gases are proportional to the reaction-zone length and inversely related to the channel width. It is also a function of the acoustic impedance ratio, $Z = \rho_r c_r/\rho_i c_i$, of explosive and inert material; the higher the ratio, the lesser the deficit.

Adams's studies were focused on the effects of changing acoustic impedances of the inert layer [43]. He concentrated on cases where $Z = \rho_r c_r/\rho_i c_i$, also known as acoustic impedance ratio, varies. Figure 2.10 depicts the two different types of detonation structures observed in his studies when the acoustic impedance of

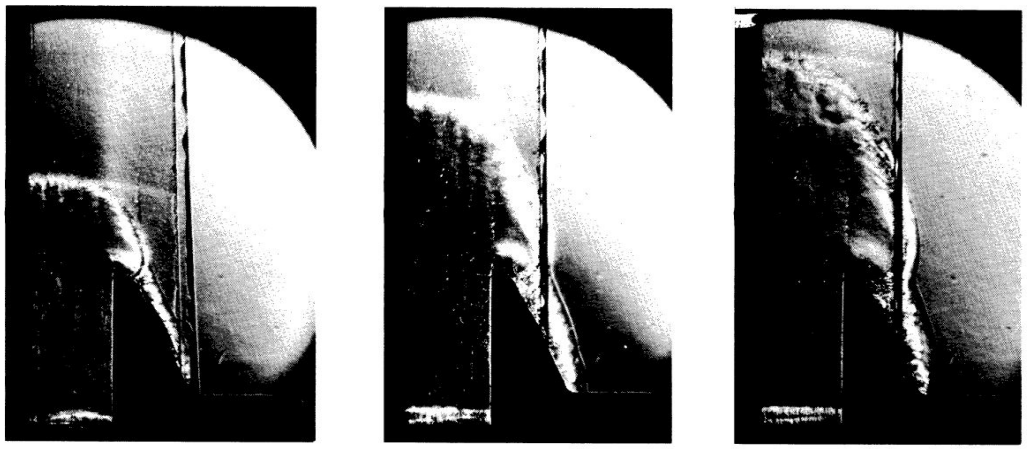

(a)

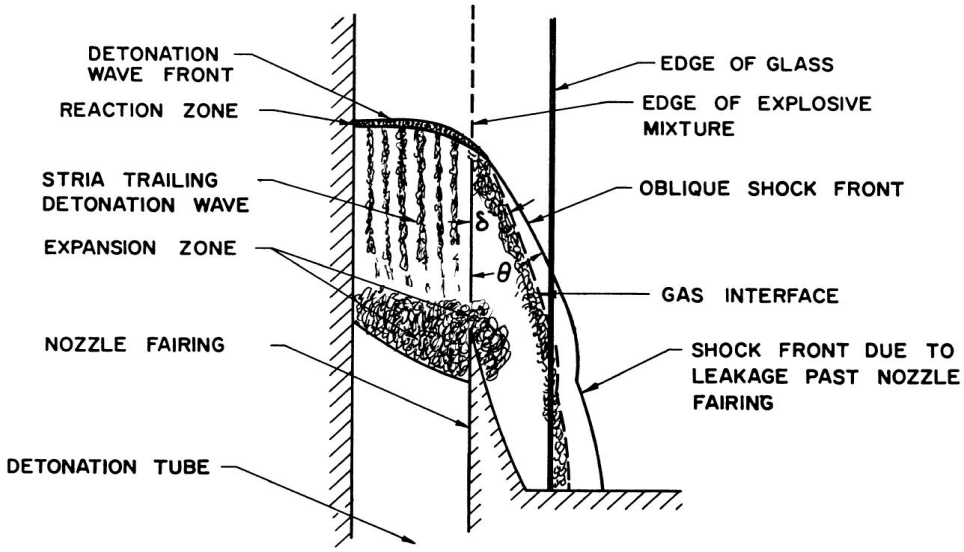

(b)

Figure 2.7: Experiments with Test Section III - (a) Schlieren photographs of the Detonation of 78% H_2 - 22% O_2 with air boundary, (b) Interpretive sketch of flow field associated with detonation next to gaseous boundary (From Reference [40]).

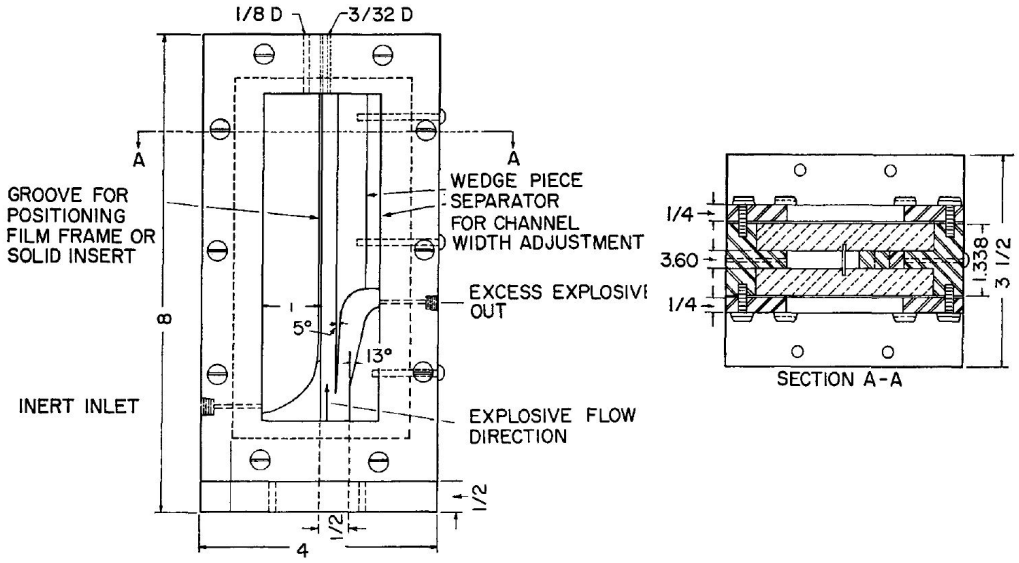

Figure 2.8: Test-Section assembly (From Reference [41])

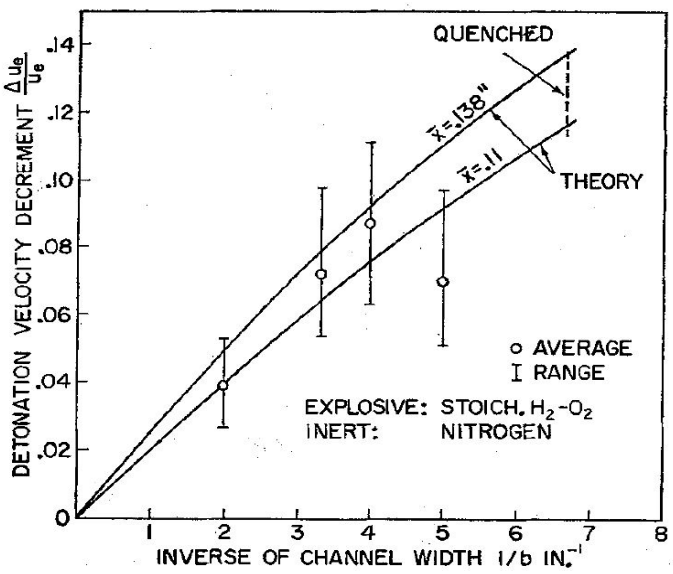

Figure 2.9: Variation of detonation velocity with channel width. $\bar{x}$ is the reaction zone length - input parameter for the theoretical model. (From Reference [41]).

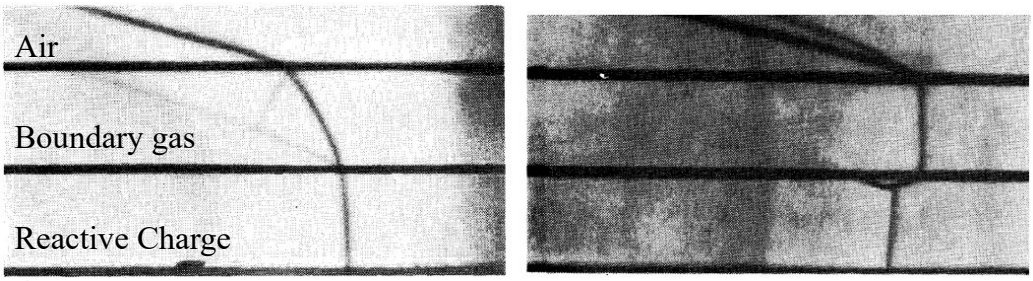

Figure 2.10: Schlieren photographs of detonations propagating in a 50% H_2 - 50% O_2 mixture confined by helium (left) and hydrogen (right). Adapted from Adams' work. (From Reference [43])

the confiner material varied from high to low. The lowermost part is the reactive mixture, followed by boundary gas separated to air by nitrocellulose film. Figure 2.10 (on the left) constitutes a detonation structure similar to existing studies when the confiner density is high. Figure 2.10 (on the right) suggests the possibility of oblique shock running forward, as evidenced in studies by Dabora. The maximum velocity deficit recorded is 17 %, twice what Dabora [41] and his peers found in their studies.

Vasil'ev challenged the findings of Dabora by arguing based on the inaccuracy of the experimental setup [44, 41]. The main argument put forth by Vasil'ev was the implementation of nitrocellulose film employed by Dabora, which would eventually sustain the pulsating detonations by reflecting triple points off the thin film. Vasil'ev proposed that there should be no physical boundary between a reactive mixture and inert gas to study the problem of weakly confined detonations.

Vasil'ev's study, therefore, pays particular attention to overcoming this problem to return to a 'free charge' propagation, as initially conceived by Sommers [21]. The

plastic tube, surrounded by air, contained the reactive media in the new configuration. This plastic tube is stretched several times its original length. The firing was triggered following the cutting of the elastic material at its base by blades placed perpendicularly. The walls then retracted due to the elastic force, and the reactive mixture was no longer confined except by the ambient air. However, the flexible wall retraction speed exceeded 70 m/s, and the interface between the reactive premix and the air became turbulent.

A novel experimental device has been developed by Vasil'ev and Zak [45] to prevent the occurrence of turbulence at the interface between the two gases. Indeed, in the first study by Vasil'ev [44], the turbulent part of gas columns can represent nearly 20% of their overall volume. The new process created two concentric flows, reactive and inert, with identical velocities. The results differ significantly from the findings of Dabora [41] and Dabora et al. [42], as the critical diameters obtained by Vasil'ev and Zak are much higher in magnitude. Again, the authors attributed these differences to nitrocellulose film, ultimately aiding the detonation propagation in Dabora's work.

2.6 Numerical Simulations of Confined Gaseous Detonations

Ivanov et al. conducted the first known numerical simulations [46, 47] of weakly confined detonations. The focus of the research was to calculate the evolution of a detonation in a finite-diameter gaseous explosive layer to identify the layer's

critical height and recreate the nonstationary conditions that occurred in the experiments. However, the results can be questioned due to the implementation of just 2000 cells in the computational domain, less than one cell per half-reaction zone length. They discovered a wide range of detonations as the transverse dimension of charge varies, ranging from a surprisingly smooth wave to powerfully pulsating waves and attenuating regimes.

In [48], Ryan et al. looked into a similar arrangement. They performed two-dimensional numerical simulations that investigate the physical mechanisms by which detonation propagates through a layer of gaseous reactants surrounded by an inert gas, focusing on the role of varying acoustic impedance ratio (Z). The results demonstrated the existence of attenuating regime for values of Z close to 1. The findings showed self-sustaining detonation for the case of $Z = 1.73$, imitating dense gas in inert media, as shown in Figure 2.11(a). Because the speed of sound is faster in the confiner material, the stable detached shock structure is observed for $Z = 0.29$, as shown in Figure 2.11(b). The disconnected shock travels a long way upstream from the detonation point. An oblique shockwave forms the intersection of these two elements, and a massive jet of fresh gas develops downstream from the front.

Chiquete and his colleagues looked into this setup to see how vital two different hydrodynamic flow factors are in achieving a steady solution to this problem [49]. The two hydrodynamic factors are (a) the energy loss associated with the transmission of transverse waves into an inert material confiner and (b) the induced detonation front curvature resulting from yielding confinement owing to flow di-

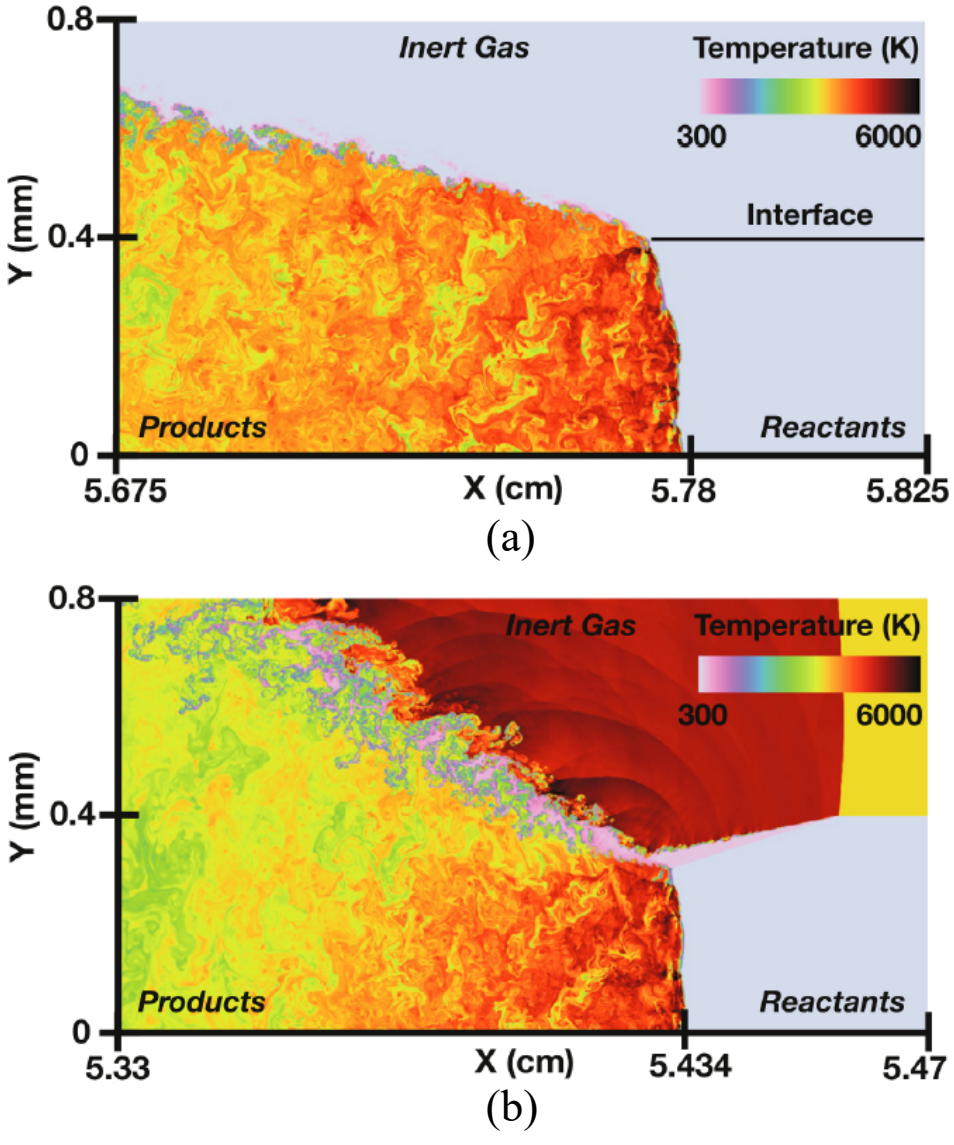

Figure 2.11: Temperature profiles for acoustic impedance ratios of (a) Z = 1:73 (T_i = 100K and T_r = 300K) (b) and Z = 0.29 (T_i = 3500K and T_r = 300K). (From Reference [48]).

vergence. They concluded that any loss of transverse waves into the confiner is not the most effective hydrodynamic mechanism for cellular structure in detonations. Instead, the global front curvature is the driving force for cell evolution and detonation stabilization in this setup.

The propagation of detonations in a layer of reactive gas surrounded by an inert gas is numerically studied using the two-dimensional Euler equations with a 1-step Arrhenius rate model controlling the energy release in homogeneous and heterogeneous systems by Mi et al. [24]. The purpose is to examine the effects of spatial inhomogeneity on near-limit wave propagation and quantify the impact of activation energy on the critical layer thickness. They concluded that the minimum required height decreased as the inhomogeneities increased. The increase in activation energy further aggravates this trend.

Reynaud and his coworkers performed numerical simulations of gaseous detonations confined by an inert layer on their side [23, 50]. The height of the reactive layer, the sensitivity of the reactive premix E_a/RT_0, and the acoustic impedance ratio (Z) are the three critical parameters of the study. They found that the reaction zone gets much thicker than a one-dimensional Wood-Kirkwood model as the activation energy increases. Moreover, the Wood-Kirkwood model fails to capture the curvature effects for high activation energy cases.

Figures 2.12 and 2.13 show the velocity deficit curves for different activation energies obtained from the numerical calculations of Mi et al. [24] and Reynaud et al. [23], respectively. It is visible from the figures that as the activation energy of the mixture is increased, the curves shift to the left on the 'D/D_{CJ} *vs* $l_{1/2}/h$' graph.

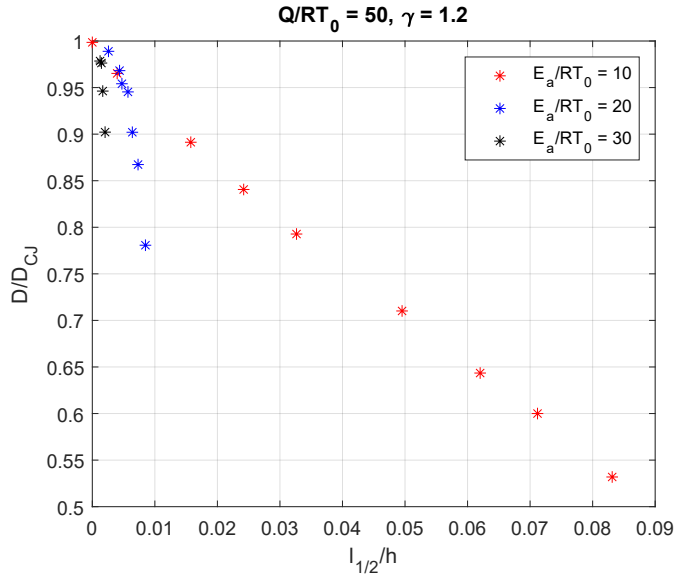

Figure 2.12: Velocity deficit curves for different activation energy as obtained from numerical simulations for $Q/RT_0 = 50$ and $\gamma = 1.2$ (From Reference [24])

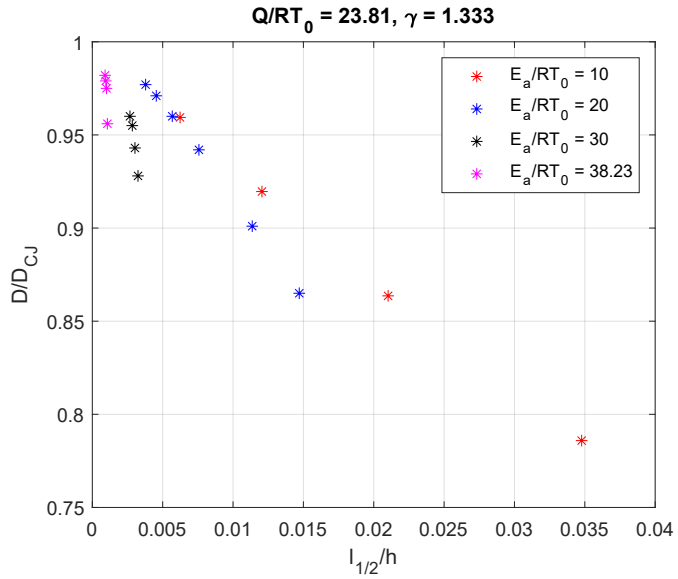

Figure 2.13: Velocity deficit curves for different activation energy as obtained from numerical simulations for $Q/RT_0 = 23.81$ and $\gamma = 1.333$ (From Reference [23])

The physical interpretation is that the detonation faces more losses in a highly unstable mixture due to multi-dimensional instabilities and the relative thickening of the reaction-zone structure. As shown in Figure 2.14(a), the cellular structure is not disturbing the flow, and reactants are burning much faster for $E_a/RT_0 = 20$ case. However, as shown in Figure 2.14(b), the increase in the activation energy allows the instabilities to grow and ultimately interact with the flow field, evidenced by the formation of reactant pockets at a much later stage for $E_a/RT_0 = 30$ case.

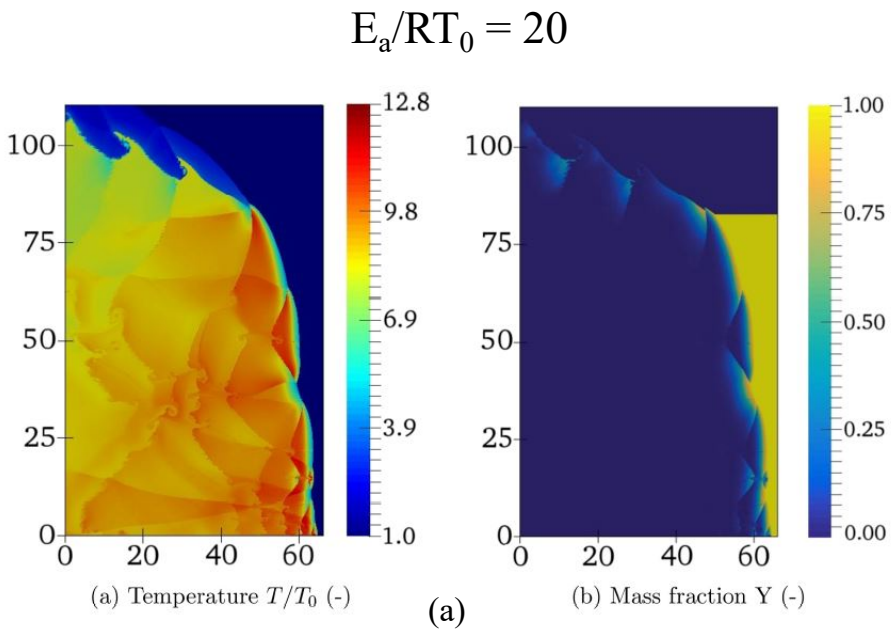

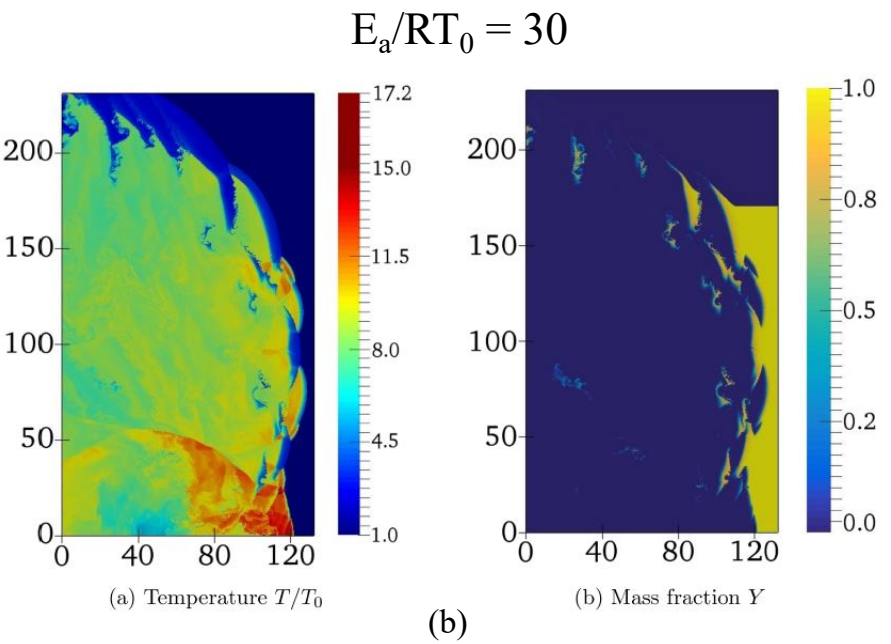

Figure 2.14: Temperature and mass reactant profiles for (a) $E_a = 20$ and $h = 82.6l_{1/2}$, (b) $E_a = 30$ and $h = 170.7l_{1/2}$ (From Reference [23])

2.7 Summary

The experiments performed by various researchers are sensitive to the reactive-confiner interaction. The presence of thin yet physical boundary aids in the triple-point reflection and thus is said to capture detonation limits incorrectly [44]. Furthermore, the diffusion between the reactive charge and the inert gas leads to a gradient of reactive mixture across the interface. However, the recent high-resolution numerical simulations by Reynaud et al. [23] and Mi et al. [24] accurately capture the dynamics of weakly confined detonations. The present study thus uses these numerical simulations as target results to validate the analytical models proposed in this work.

Chapter 3

Straight Streamline Approximation Model

3.1 Introduction

Watt et al. [22] developed a mathematical model based on the fluid-streamline approach of the flow of reactive material across the detonation front to study the dynamics of non-ideal detonations [22]. The model employs a streamline-based approach where the solution along each streamline is merged to generate the detonation structure for a given detonation speed. However, this requires a prior assumption on the shape of the streamlines as an input parameter to the model.

The model adopts the steady reactive Euler equations in streamline-based coordinates (ψ, y), with the assumption of 'straight' streamlines. Figure 3.1 shows the setup. The governing equations coupled with any arbitrarily chosen chemistry are

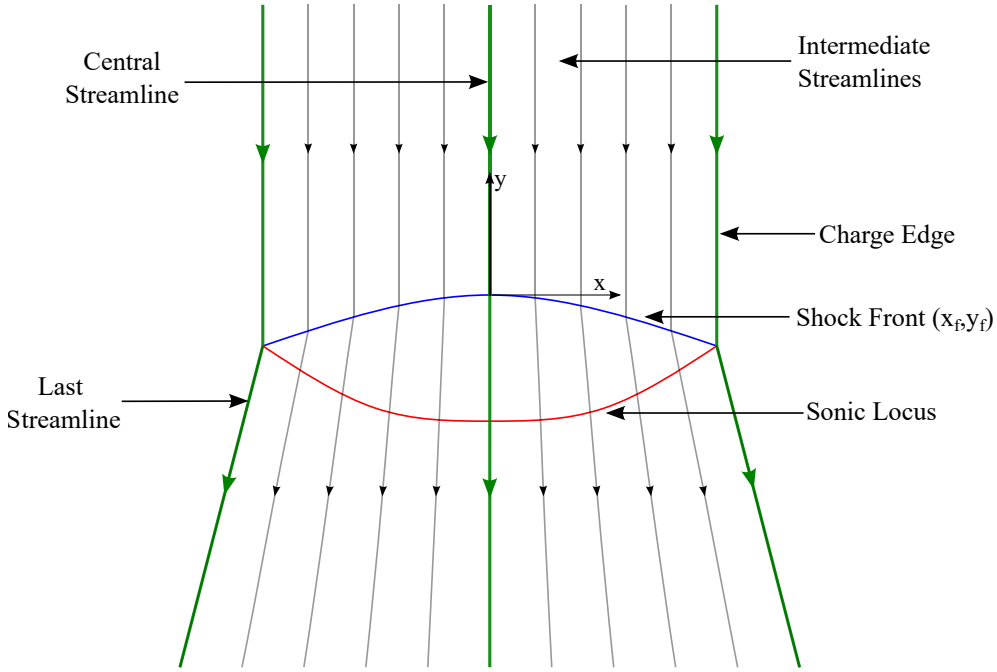

Figure 3.1: Schematic of a steady detonation experiencing lateral area divergence.

integrated on the central streamline, with generalized CJ conditions at the sonic locus providing the constraints at the shock. The process is repeated for all the intermediate streamlines as we move from the charge axis to the charge edge along the shock front. The model gives the shape of the lead shock, sonic locus, structure of reaction zone and corresponding charge thickness for a given velocity deficit. The model is deployed for a series of varying velocity of detonations to obtain the corresponding detonation structure for a particular reactive-inert couple. This information can be used to analyze the influence of varying charge-thickness on the velocity of non-ideal detonations - the ”Diameter-effect” curve.

The first account of the detailed derivation of the Straight Streamline Approxima-

tion (SSA) model is given in Cartwright's thesis [51], and a similar methodology is followed here. Section 3.1 of this chapter introduces the SSA model. The steady reactive Euler equations in the streamline-based coordinate system are derived in section 3.2. In section 3.3, loss terms in the governing equations are derived by making an assumption on the shape of the streamlines - straight yet diverging. The initial conditions and the slope of the straight streamlines, which are needed to integrate the governing ODEs, are obtained via oblique shock relations in section 3.4. Section 3.5 describes the detailed numerical procedure of implementation of the SSA model. Next, an appropriate boundary criterion for marching along the lead shock until the reactant-inert interface is derived in section 3.6. The SSA model developed in this work is verified by comparing with the existing results of Watt et al. [22] in section 3.7. Finally, the SSA model is deployed for weakly confined gaseous detonations with the 1-step Arrhenius rate law, and the relevant results are reported in section 3.8, which will be further discussed in detail in chapter 5.

3.2 Governing Equations in Streamline Coordinates

3.2.1 Streamline Function

In order to derive the governing equations in streamline-based coordinates, we have to define the compressible streamline function ψ. In Cartesian coordinates (x, y), the compressible streamline function ψ is given by,

$$\left(\frac{\partial \psi}{\partial y}\right)_x = \rho u \tag{3.1}$$

$$\left(\frac{\partial \psi}{\partial x}\right)_y = -\rho v \tag{3.2}$$

The symbols u and v represent the flow velocity of the medium in the x and y-direction, respectively. By the definition of stream function ψ, the change in the differential amount of stream function is given by,

$$d\psi = \frac{\partial \psi}{\partial x}dx + \frac{\partial \psi}{\partial y}dy$$

$$\therefore d\psi = \rho u dy - \rho v dx$$

For the analysis on a particular streamline, $d\psi \to 0$, thereby giving us the expression,

$$\left(\frac{\partial x}{\partial y}\right)_\psi = \frac{u}{v} \tag{3.3}$$

The local flow direction is tangent to the flow velocity, which is true everywhere, according to equation (3.3). The reactive Euler equations will be transformed from the Cartesian coordinate system (x,y) to the streamline-based coordinate system (ψ,y) by employing the definition of the streamline function. The transverse direction x is now a function of the stream function so that $x = x(\psi,y)$.

3.2.2 Material Derivative

The material derivative in Cartesian coordinates is,

$$\frac{D}{Dt} = \frac{\partial}{\partial t} + \mathbf{v} \cdot \nabla$$

The problem we are studying is steady, and the geometry is two-dimensional in Cartesian coordinates. This simplifies the material derivative to,

$$\frac{D}{Dt} = \left(u\hat{i} + v\hat{j}\right) \cdot \left(\frac{\partial}{\partial x}\hat{i} + \frac{\partial}{\partial y}\hat{j}\right)$$

Thus, for the given test function $f = f(x,y)$, the material derivative of it is,

$$\frac{Df}{Dt} = u\left(\frac{\partial f}{\partial x}\right)_y + v\left(\frac{\partial f}{\partial y}\right)_x$$

The terms in the material derivative are expanded with respect to ψ and y yielding,

$$\begin{aligned}\frac{Df}{Dt} =& u\left[\left(\frac{\partial f}{\partial \psi}\right)_y\left(\frac{\partial \psi}{\partial x}\right)_y + \left(\frac{\partial f}{\partial y}\right)_\psi\left(\frac{\partial y}{\partial x}\right)_y\right] \\ &+ \quad v\left[\left(\frac{\partial f}{\partial \psi}\right)_y\left(\frac{\partial \psi}{\partial y}\right)_x + \left(\frac{\partial f}{\partial y}\right)_\psi\left(\frac{\partial y}{\partial y}\right)_x\right]\end{aligned}$$

By using equations (3.1) and (3.2) and substituting them in the definition of the material derivative, and the term $\left(\frac{\partial y}{\partial x}\right)_y = 0$, we get

$$\frac{Df}{Dt} = -\rho uv\left(\frac{\partial f}{\partial \psi}\right)_y + \rho uv\left(\frac{\partial f}{\partial \psi}\right)_y + v\left(\frac{\partial f}{\partial y}\right)_\psi$$

Thus the definition of material derivative in streamlined-based coordinates for a steady problem is given by,

$$\frac{D}{Dt} = v\left(\frac{\partial}{\partial y}\right)_\psi \tag{3.4}$$

This definition of the material derivative will be used to derive the steady reactive Euler equations in the streamline-based coordinates (ψ, y).

3.2.3 Continuity Equation

The continuity equation in two-dimensional Cartesian coordinates is given by,

$$\frac{D\rho}{Dt} + \rho\left[\left(\frac{\partial u}{\partial x}\right)_y + \left(\frac{\partial v}{\partial y}\right)_x\right] = 0 \tag{3.5}$$

By replacing the material derivative defined for streamline-based coordinates, equation (3.4), and simplifying the partial derivative terms with respect to ψ and y, we obtain,

$$v\left(\frac{\partial \rho}{\partial y}\right)_\psi + \rho\left[\left(\frac{\partial u}{\partial y}\right)_\psi\left(\frac{\partial y}{\partial x}\right)_y + \left(\frac{\partial u}{\partial \psi}\right)_y\left(\frac{\partial \psi}{\partial x}\right)_y\right]$$
$$+\rho\left[\left(\frac{\partial v}{\partial \psi}\right)_y\left(\frac{\partial \psi}{\partial y}\right)_x + \left(\frac{\partial v}{\partial y}\right)_\psi\left(\frac{\partial y}{\partial y}\right)_x\right] = 0$$

We know that,

$$\left(\frac{\partial y}{\partial x}\right)_y = 0,\ \left(\frac{\partial \psi}{\partial y}\right)_x = \rho u,\ \left(\frac{\partial \psi}{\partial x}\right)_y = -\rho v$$

Thus equation (3.5) reduces to,

$$v\left(\frac{\partial \rho}{\partial y}\right)_\psi - \rho^2 v\left(\frac{\partial u}{\partial \psi}\right)_\psi + \rho^2 u\left(\frac{\partial v}{\partial \psi}\right)_y + \rho\left(\frac{\partial v}{\partial y}\right)_\psi = 0$$

Dividing the abovementioned equation by $-\rho^2 v^2$, we get,

$$\left[-\frac{1}{\rho^2 v}\left(\frac{\partial \rho}{\partial y}\right)_\psi - \frac{1}{\rho v^2}\left(\frac{\partial v}{\partial y}\right)_\psi\right] + \left[\frac{1}{v}\left(\frac{\partial u}{\partial \psi}\right)_y - \frac{u}{v^2}\left(\frac{\partial v}{\partial \psi}\right)_y\right] = 0$$

Thus, the continuity equation in streamline-based coordinates for the steady-state is given by equation (3.6).

$$\frac{\partial}{\partial y}\left(\frac{1}{\rho v}\right)_\psi + \frac{\partial}{\partial \psi}\left(\frac{u}{v}\right)_y = 0 \tag{3.6}$$

3.2.4 Momentum Equation in the x-direction

The momentum equation of steady reactive Euler equations in the x-direction of Cartesian coordinates is given by,

$$\rho \frac{Du}{Dt} + \left(\frac{\partial p}{\partial x}\right)_y = 0 \tag{3.7}$$

Using equation (3.4) and expanding the partial derivative term, we get,

$$\rho \left[v \left(\frac{\partial u}{\partial y}\right)_\psi \right] + \left[\left(\frac{\partial p}{\partial \psi}\right)_y \left(\frac{\partial \psi}{\partial x}\right)_y + \left(\frac{\partial p}{\partial y}\right)_\psi \left(\frac{\partial y}{\partial x}\right)_y \right] = 0$$

By using equation (3.2) and $\left(\frac{\partial y}{\partial x}\right)_y = 0$, equation (3.7) is transformed to,

$$\rho v \left(\frac{\partial u}{\partial y}\right)_\psi - \rho v \left(\frac{\partial p}{\partial \psi}\right)_y = 0$$

Thus, the momentum equation in x-direction transformed to streamline-based coordinates is given by equation (3.8).

$$\left(\frac{\partial u}{\partial y}\right)_\psi - \left(\frac{\partial p}{\partial \psi}\right)_y = 0 \tag{3.8}$$

3.2.5 Momentum Equation in the y-direction

The momentum equation of steady reactive Euler equations in the y-direction of Cartesian coordinates is given by equation (3.9).

$$\rho \frac{Dv}{Dt} + \left(\frac{\partial p}{\partial y}\right)_x = 0 \tag{3.9}$$

Using equation (3.4) and expanding the partial derivative term, we get,

$$\rho \left[v \left(\frac{\partial v}{\partial y}\right)_\psi \right] + \left[\left(\frac{\partial p}{\partial \psi}\right)_y \left(\frac{\partial \psi}{\partial y}\right)_x + \left(\frac{\partial p}{\partial y}\right)_\psi \left(\frac{\partial y}{\partial y}\right)_x \right] = 0$$

By substituting 3.1 in the abovementioned equation, we get the y-momentum equation transformed to the streamline-based coordinates presented here in equation (3.10).

$$\rho v \left(\frac{\partial v}{\partial y}\right)_\psi + \rho u \left(\frac{\partial p}{\partial \psi}\right)_y + \left(\frac{\partial p}{\partial y}\right)_\psi = 0 \tag{3.10}$$

3.2.6 Energy equation and Rate law

The energy equation for steady reactive Euler is given by equation (3.11).

$$\frac{De}{Dt} - \frac{p}{\rho^2}\frac{D\rho}{Dt} = 0 \tag{3.11}$$

Upon applying the material derivative definition in streamline-based coordinates, the energy equation in streamline coordinates is given by equation (3.12).

$$\left(\frac{\partial e}{\partial y}\right)_{\psi} = \frac{p}{\rho^2}\left(\frac{\partial \rho}{\partial y}\right)_{\psi} \tag{3.12}$$

$$\frac{d\lambda}{dt} = W \tag{3.13}$$

Similarly, the rate law defined in equation (3.13) is transformed to equation (3.14), shown in streamlined-based coordinates.

$$\left(\frac{\partial \lambda}{\partial y}\right)_{\psi} = \frac{W}{v} \tag{3.14}$$

The mass conservation, momentum conservation in the x and y direction, and energy and rate law equations, which are transformed in streamline-based coordinates, are bundled together to form the governing equations, presented here by equations (3.15)-(3.19).

$$\frac{\partial}{\partial y}\left(\frac{1}{\rho v}\right)_{\psi} + \frac{\partial}{\partial \psi}\left(\frac{u}{v}\right)_{y} = 0 \tag{3.15}$$

$$\left(\frac{\partial u}{\partial y}\right)_{\psi} - \left(\frac{\partial p}{\partial \psi}\right)_{y} = 0 \tag{3.16}$$

$$\rho v\left(\frac{\partial v}{\partial y}\right)_{\psi} + \rho u\left(\frac{\partial p}{\partial \psi}\right)_{y} + \left(\frac{\partial p}{\partial y}\right)_{\psi} = 0 \tag{3.17}$$

$$\left(\frac{\partial e}{\partial y}\right)_{\psi} = \frac{p}{\rho^2}\left(\frac{\partial \rho}{\partial y}\right)_{\psi} \tag{3.18}$$

$$\left(\frac{\partial \lambda}{\partial y}\right)_{\psi} = \frac{W}{v} \tag{3.19}$$

3.2.7 Governing Equations

The governing equations transformed to a streamline-based coordinate system, as derived in subsections 3.2.3-3.2.6, are currently not in Ordinary Differential Equation (ODE) form; thus, we need to simplify them to obtain a trivial form.

Here, we start with the continuity equation given by,

$$\frac{\partial}{\partial y}\left(\frac{1}{\rho v}\right)_{\psi} + \frac{\partial}{\partial \psi}\left(\frac{u}{v}\right)_{y} = 0 \tag{3.20}$$

Upon expanding, we get,

$$-\frac{1}{\rho^2 v}\left(\frac{\partial \rho}{\partial y}\right)_{\psi} - \frac{1}{\rho v^2}\left(\frac{\partial v}{\partial y}\right)_{\psi} + \frac{\partial}{\partial \psi}\left(\frac{u}{v}\right)_{y} = 0$$

By making the $\left(\frac{\partial \rho}{\partial y}\right)_{\psi}$ term subject and substituting from 3.3, we get the density evolution along the particular streamline ψ after the initial shock.

$$\left(\frac{\partial \rho}{\partial y}\right)_{\psi} = \rho^2 v\left(\frac{\partial^2 x}{\partial \psi \partial y}\right) - \frac{\rho}{v}\left(\frac{\partial v}{\partial y}\right)_{\psi} \tag{3.21}$$

We will simplify equations (3.16) and (3.17) to derive the pressure evolution along a streamline. By direct substitution of (3.16) into (3.17), it yields,

$$\rho v\left(\frac{\partial v}{\partial y}\right)_{\psi}+\rho u\left(\frac{\partial u}{\partial y}\right)_{\psi}+\left(\frac{\partial p}{\partial y}\right)_{\psi}=0$$

From equation (3.3),

$$u=v\left(\frac{\partial x}{\partial y}\right)_{\psi}\rightarrow\ \therefore\ \left(\frac{\partial u}{\partial y}\right)_{\psi}=v\left(\frac{\partial^2 x}{\partial y^2}\right)_{\psi}+\left(\frac{\partial x}{\partial y}\right)_{\psi}\left(\frac{\partial v}{\partial y}\right)_{\psi}$$

After substituting the above expressions, then the evolution of pressure along the streamline ψ is given by equation (3.22),

$$\left(\frac{\partial p}{\partial y}\right)_{\psi}=-\rho v\left(\frac{\partial v}{\partial y}\right)_{\psi}-\rho v^2\left(\frac{\partial x}{\partial y}\right)_{\psi}\left(\frac{\partial^2 x}{\partial y^2}\right)_{\psi}-\rho v\left(\frac{\partial x}{\partial y}\right)_{\psi}^2\left(\frac{\partial v}{\partial y}\right)_{\psi} \quad (3.22)$$

Here the equation of state is given by 4.3, partial derivative with respect to y with keeping ψ constant gives,

$$\left(\frac{\partial e}{\partial y}\right)_{\psi}=\frac{1}{(\gamma-1)\rho}\left(\frac{\partial p}{\partial y}\right)_{\psi}-\frac{p}{(\gamma-1)\rho^2}\left(\frac{\partial \rho}{\partial y}\right)_{\psi}-Q\left(\frac{\partial \lambda}{\partial y}\right)_{\psi} \quad (3.23)$$

By substituting equations (3.23) and (3.19) in equation (3.18), we get,

$$\frac{1}{(\gamma-1)\rho}\left(\frac{\partial p}{\partial y}\right)_{\psi}-\frac{p}{(\gamma-1)\rho^2}\left(\frac{\partial \rho}{\partial y}\right)_{\psi}-\frac{QW}{v}=\frac{p}{\rho^2}\left(\frac{\partial \rho}{\partial y}\right)_{\psi}$$

Upon simplification, we get,

$$\frac{1}{(\gamma-1)\rho}\left(\frac{\partial p}{\partial y}\right)_{\psi}-\frac{\gamma}{\gamma-1}\frac{p}{\rho^2}\left(\frac{\partial \rho}{\partial y}\right)_{\psi}-\frac{QW}{v}=0 \tag{3.24}$$

By substituting (3.21) and (3.22) in equation (3.24), it yields,

$$\left(\frac{\partial v}{\partial y}\right)_{\psi}\left[\left(\frac{\gamma p}{\rho}\right)-v^2\left(1+\left(\frac{\partial x}{\partial y}\right)_{\psi}^2\right)\right]=$$
$$\left(\frac{\gamma p}{\rho}\right)(\rho v)\,v\left(\frac{\partial^2 x}{\partial \psi \partial y}\right)+v^3\left(\frac{\partial x}{\partial y}\right)_{\psi}\left(\frac{\partial^2 x}{\partial y^2}\right)_{\psi}+Q(\gamma-1)W$$

Using 3.3 and making $\left(\frac{\partial v}{\partial y}\right)_{\psi}$ as the target variable, we get,

$$\left(\frac{\partial v}{\partial y}\right)_{\psi}=\frac{\left(\frac{\partial x}{\partial \psi}\right)_{y}^{-1}c^2 v\left(\frac{\partial^2 x}{\partial \psi \partial y}\right)-v^3\left(\frac{\partial x}{\partial y}\right)_{\psi}\left(\frac{\partial^2 x}{\partial y^2}\right)_{\psi}-Q(\gamma-1)W}{\left[v^2\left(1+\left(\frac{\partial x}{\partial y}\right)_{\psi}^2\right)-c^2\right]} \tag{3.25}$$

Here, we rewrite the equations (3.25), (3.21), (3.22) and (3.14) as equations (3.26)-(3.29) which ultimately are the governing equations in trivial ODE form which can be integrated easily. The equations (3.26)-(3.29) depict the evolution of velocity of the flow in the y-direction (v), density (ρ), pressure (p) and reaction progress variable (λ) from the shocked state until the generalized CJ condition is met at sonic locus along a fixed streamline.

$$\left(\frac{\partial v}{\partial y}\right)_{\psi} = \frac{\left(\frac{\partial x}{\partial \psi}\right)_{y}^{-1} c^2 v \left(\frac{\partial^2 x}{\partial \psi \partial y}\right) - v^3 \left(\frac{\partial x}{\partial y}\right)_{\psi} \left(\frac{\partial^2 x}{\partial y^2}\right)_{\psi} - Q(\gamma - 1)W}{\left[v^2 \left(1 + \left(\frac{\partial x}{\partial y}\right)_{\psi}^2\right) - c^2\right]} \tag{3.26}$$

$$\left(\frac{\partial \rho}{\partial y}\right)_{\psi} = \rho^2 v \left(\frac{\partial^2 x}{\partial \psi \partial y}\right) - \frac{\rho}{v}\left(\frac{\partial v}{\partial y}\right)_{\psi} \tag{3.27}$$

$$\left(\frac{\partial p}{\partial y}\right)_{\psi} = -\rho v \left(\frac{\partial v}{\partial y}\right)_{\psi} - \rho v^2 \left(\frac{\partial x}{\partial y}\right)_{\psi} \left(\frac{\partial^2 x}{\partial y^2}\right)_{\psi} - \rho v \left(\frac{\partial x}{\partial y}\right)_{\psi}^2 \left(\frac{\partial v}{\partial y}\right)_{\psi} \tag{3.28}$$

$$\left(\frac{\partial \lambda}{\partial y}\right)_{\psi} = \frac{W}{v} \tag{3.29}$$

In order to quantify the different terms in equations (3.26)-(3.29), one has to make an assumption on the shape of the streamlines. The detailed account of the quantification is described in section 3.3. The initial conditions for these governing equations are given by thermodynamic properties at the von-Neumann state and are discussed in much depth in section 3.4.

However, in order to solve the overall structure of detonation, one has to solve the governing equations on all streamlines between the charge axis and charge edge. The process of solving ODEs on all stream tubes and merging them to obtain the complete detonation structure is described in section 3.5.

3.3 Straight Streamline Approximation

This section describes the simplification of different derivative terms showing up in the governing equations. In order to solve the governing equations, one needs to know the expression of the following terms,

$$\left(\frac{\partial x}{\partial \psi}\right)^{-1}, \left(\frac{\partial^2 x}{\partial \psi \partial y}\right), \left(\frac{\partial x}{\partial y}\right)_{\psi}, \left(\frac{\partial^2 x}{\partial y^2}\right)_{\psi}$$

The terms $\left(\frac{\partial x}{\partial y}\right)_{\psi}$ and $\left(\frac{\partial^2 x}{\partial y^2}\right)_{\psi}$ correspond to the slope and curvature of streamlines, respectively. The terms $\left(\frac{\partial x}{\partial \psi}\right)^{-1}$ and $\left(\frac{\partial^2 x}{\partial \psi \partial y}\right)$ correspond to divergence of streamline in reaction zone structure. Here, we replicate the assumption initially put forth by Watt et al. [22] to simplify these terms. The assumption states that the streamlines after passing through the lead shock must remain straight and diverging from each other.

The Straight Streamline Approximation (SSA) implies that the flow behind the shock is linear but diverging. At point (x_f, y_f), the streamlines intersect the shock and deflect at a particular angle dependent on the shock's obliqueness and are derived in section 3.4. The flow of gases continues on the straight yet diverging streamlines from the shock front to the very end, passing through the sonic locus and the reaction zone's end.

As the streamlines incoming towards the shock front are parallel to the central streamline, that intersects the shock at $x_f = 0, y_f = 0$, the stream function ψ is given by equation (3.30). Alternatively, integrating equation (3.2) yields the same result. Here, D_0 is the speed with which the detonation is steadily propagating,

and x_f is the x-coordinate of the shock front.

$$\psi = \rho_0 D_0 x_f \tag{3.30}$$

From the above equation (3.30), we can get,

$$\left(\frac{\partial x_f}{\partial \psi}\right)_{y_f} = \frac{1}{\rho_0 D_0} \tag{3.31}$$

The streamlines deflect at the shock front, and oblique shock conditions govern their deflection angle. The shape of straight streamlines is thus given by a straight-line equation given here by 3.32.

$$x = x_f + F(\psi)(y - y_f) \tag{3.32}$$

Here the slope of the streamline is $F(\psi)$ is given by,

$$F(\psi) = \left(\frac{\partial x}{\partial y}\right)_{\psi} = \frac{u_f}{v_f} \tag{3.33}$$

Here, u_f is the transverse velocity just after the shock, and v_f is the velocity component in the y-direction immediately after the shock. We can take the derivative of equation (3.32) to get,

$$\left(\frac{\partial^2 x}{\partial y^2}\right)_{\psi} = 0 \tag{3.34}$$

In equation (3.34), $\left(\frac{\partial^2 x}{\partial y^2}\right)_{\psi}$ represents the curvature of the streamline. As we

have assumed streamlines to be straight, this term will not contribute to governing equations. Now we have to find expressions for $\left(\frac{\partial x}{\partial \psi}\right)_y$ and $\left(\frac{\partial^2 x}{\partial \psi \partial y}\right)$ in order to integrate the governing ODEs .Upon taking the derivative of equation (3.32) with respect to ψ at constant y, it yields,

$$\left(\frac{\partial x}{\partial \psi}\right)_y = \left(\frac{\partial x_f}{\partial \psi}\right)_y + \left(\frac{\partial F}{\partial \psi}\right)_y (y - y_f) - F(\psi)\left(\frac{\partial y_f}{\partial \psi}\right)_y \tag{3.35}$$

Upon parameterizing y_f in terms of x_f, we can simplify the term $\left(\frac{\partial y_f}{\partial \psi}\right)_y$ as shown here in equation (3.36), with $y_f^{'}$ being the shock front's slope where it meets the streamline. Moreover, only the derivatives of ψ are present; we can convert the partial differential terms to ordinary differential terms,

$$\left(\frac{\partial x}{\partial \psi}\right)_y = \frac{dx_f}{d\psi} + \frac{dF}{d\psi}(y - y_f) - F(\psi) y_f^{'} \frac{dx_f}{d\psi} \tag{3.36}$$

Upon retaking the derivative of the equation (3.37), we get,

$$\left(\frac{\partial^2 x}{\partial \psi \partial y}\right)_y = \frac{dF}{d\psi} \tag{3.37}$$

As we know from our assumption of straight yet diverging streamlines, the slope of the streamline deflected after the shock is dependent on the shock front slope (obliqueness of the lead shock); thus, the streamline slope F is a function of $y_f^{'}$, and we can write,

$$\frac{dF}{d\psi} = \left(\frac{\partial F}{\partial y_f^{'}}\right) y_f^{''} \frac{dx_f}{d\psi} \tag{3.38}$$

By substituting 3.31, we get,

$$\left(\frac{\partial^2 x}{\partial \psi \partial y}\right) = \frac{dF}{d\psi} = \frac{\frac{dF}{dy_f^{'}} y_f^{''}}{\rho_0 D_0} \tag{3.39}$$

And by substituting equations (3.39) and (3.31) in (3.35), the term $\left(\frac{\partial x}{\partial \psi}\right)_y$ is given by,

$$\left(\frac{\partial x}{\partial \psi}\right)_y = \frac{1}{\rho_0 D_0}\left[1 + \frac{dF}{dy_f^{'}} y_f^{''}(y - y_f) - F y_f^{'}\right] \tag{3.40}$$

Thus, we have derived the expression for all the terms present in the governing equations. We can substitute the equations (3.33), (3.34), (3.39) and (3.40) in the governing equations so that one can easily integrate them.

It is evident from 3.39 and 3.40 that the governing equations depend on shock front location (x_f, y_f), the slope of the shock front given by $y_f^{'}$ and the curvature of shock front $y_f^{''}$. When the shock front location (x_f, y_f) and shock slope $y_f^{'}$ are known, the governing equations, described along a particular streamline, transform into an eigenvalue problem which is solved by correctly choosing the proper value of shock curvature $y_f^{''}$, thereby matching generalized CJ condition at sonic locus. The governing equations are integrated on all incoming streamlines to obtain the complete detonation structure.

However, we still need to evaluate - u_f, v_f, and $\frac{dF}{dy_f^{'}}$ to close the derivative expressions derived in this section. u_f, v_f, and $\frac{dF}{dy_f^{'}}$ correspond to transverse and longitudinal flow velocities at the shocked state and the change in slope of the streamlines with respect to the change in the lead shock slope. These three pa-

rameters are evaluated in section 3.4.

3.4 Oblique Shock Relations

This section is devoted to deriving the expression for u_f, v_f, and $\frac{dF}{dy_f^{'}}$, as these parameters show up in the governing equations. The governing equations need initial conditions as an input so that one can solve them on a fixed streamline until the generalized CJ condition is met at the sonic locus. These initial conditions are the v_f, ρ_f, p_f and λ_f - longitudinal velocity, density, pressure of the flow and the reaction progress variable at the shocked state, respectively.

Moreover, as the streamlines deflect at an angle governed by the shock slope, one needs to obtain a generalized expression for the initial conditions as a function of shock slope ($y_f^{'}$) so that the governing equations can be solved on any arbitrarily chosen streamline. The computation of the shock front location (x_f, y_f) and the shock slope $y_f^{'}$ from which any arbitrarily chosen streamline passes is described in section 3.5, as their prior knowledge is necessary (section 3.3) to solve the governing equations.

The oblique shock relations can calculate the pressure, density, and flow velocities in the axial and transverse direction just after the shock front, at the post-shock state, along each streamline. These thermodynamic properties are obtained using the normal shock-jump conditions for a one-dimensional flow. Figure 3.2 summarizes the various velocity components and their relative values following the shock. The vital point to note is that the transverse velocity v_t, the component of

velocity in the tangential direction to the incidental shock front at a given streamline, does not vary in magnitude or direction after passing through the shock.

Here, v_{n_0} is the normal component of initial velocity D_0 and is perpendicular to v_t. v_{n_1} is the normal component of the post-shock flow velocity. Subscript 0 denotes the unreacted state, while subscript 1 denotes the von-Neumann state. The flow velocity in the direction of detonation propagation at the von-Neumann state is given by v_f. u_f is the flow velocity normal to the v_f at the post-shock state, contributing to lateral area divergence in the reaction zone. θ is the angle made by the incoming streamline carrying the unreacted flow, in shock attached frame of reference, with the oblique lead shock. Here, w_1 is the total flow velocity at the shocked state and is given by equation (3.41),

$$\vec{w_1} = \vec{v_{n_1}} + \vec{v_t} = \vec{v_f} + \vec{u_f} \tag{3.41}$$

Thus the magnitude of w_1 is given by,

$$w_1 = \sqrt{v_{n_1}^2 + v_t^2} = \sqrt{v_f^2 + u_f^2} \tag{3.42}$$

It is clear from Figure 3.2 that,

$$v_{n_0} = D_0 \, cos\left(\frac{\pi}{2} - \theta\right) = D_0 \, sin\,\theta \tag{3.43}$$

$$v_t = D_0 \, sin\left(\frac{\pi}{2} - \theta\right) = D_0 \, cos\,\theta \tag{3.44}$$

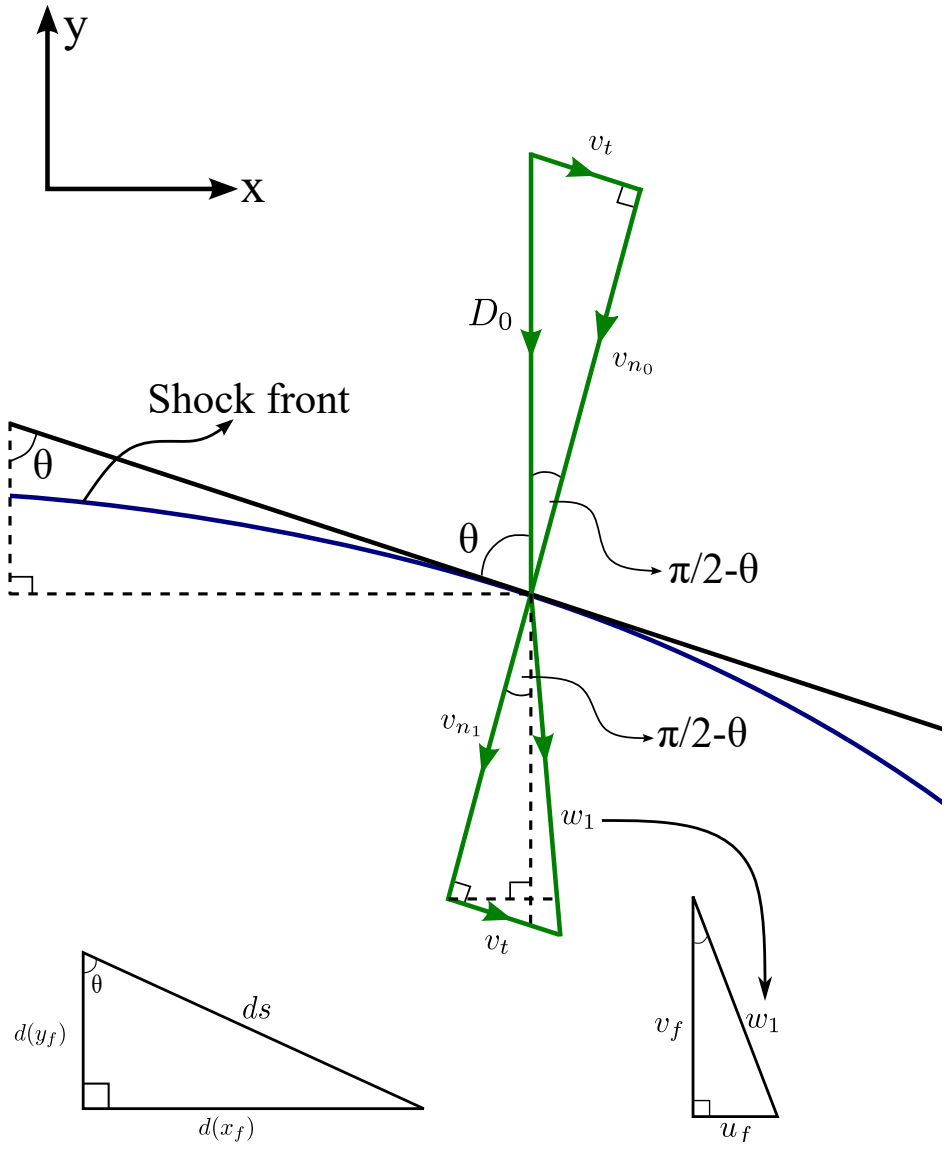

Figure 3.2: Representation of an oblique shock parameters relevant to the curved shock front in steady detonation.

The post-shock velocities is given by v_f and u_f, in y and x directions and can be obtained from Figure 3.2 as follows,

$$v_f = v_{n_1} \sin\theta + v_t \cos\theta \tag{3.45}$$

$$u_f = -v_{n_1} \cos\theta + v_t \sin\theta \tag{3.46}$$

The terms $\sin\theta$ and $\cos\theta$ are now required to convert to some known quantities. From Figure 3.2, it is evident that the shock slope can be defined by equation (3.47),

$$\cot\theta = \frac{dy_f}{dx_f} = y_f^{'} \tag{3.47}$$

Thus, the terms $\sin\theta$ and $\cos\theta$ are given by equations (3.48) and 3.49 from trigonometric relations.

$$\sin\theta = \frac{1}{\sqrt{1+\cot^2\theta}} = \frac{1}{\sqrt{1+(y_f^{'})^2}} \tag{3.48}$$

$$\cos\theta = \frac{\cot\theta}{\sqrt{1+\cot^2\theta}} = \frac{y_f^{'}}{\sqrt{1+(y_f^{'})^2}} \tag{3.49}$$

By substituting equations (3.48) and (3.49) in equation (3.45), the final expression for the v_f is given by equation (3.50).

$$v_f = \frac{v_{n_1}}{\sqrt{1+(y_f^{'})^2}} + \frac{v_t y_f^{'}}{\sqrt{1+(y_f^{'})^2}} \tag{3.50}$$

After Substituting v_t from equation (3.44) and simplifying the expression, we get,

$$v_f = \frac{v_{n_1}(1+(y_f^{'})^2)^{\frac{1}{2}} + D_0 (y_f^{'})^2}{1+(y_f^{'})^2} \tag{3.51}$$

Similarly, the transverse velocity component u_f is given by,

$$u_f = \frac{-v_{n_1} y_f^{'}(1+(y_f^{'})^2)^{\frac{1}{2}} + D_0 y_f^{'}}{1+(y_f^{'})^2} \tag{3.52}$$

It is essential to note that v_{n_1} is the normal velocity component after the shock, given by shock jump conditions. We need to evaluate the density jump before we compute the v_{n_1}.

The density jump across the shock is given by equation (3.53),

$$\frac{\rho_f}{\rho_0} = \frac{(\gamma+1)M_N^2}{(\gamma-1)M_N^2+2} \tag{3.53}$$

Here is M_N is the normal Mach-Number approaching the flow and mathematically denoted by,

$$M_N = \frac{v_{n_0}}{c_0} = \frac{D_0 sin\,\theta}{c_0} = M_0 \, sin\,\theta = \frac{M_0}{\sqrt{1+(y_f^{'})^2}} \tag{3.54}$$

Here, M_0 is the Mach number of the detonation propagating steadily under the influence of losses from inert confiner. It is described as follows,

$$M_0 = f \cdot M_{CJ} \tag{3.55}$$

Where f is the velocity deficit of the detonation and M_{CJ} is the CJ-Mach number of the detonation for given Q and γ, which are the properties of the reactive mixture. The system is non-dimensionalized by initial pressure, density and half-reaction zone length of the no-loss ZND solution. Therefore, $c_0 = \sqrt{\gamma}$.

Thus, after substituting 3.54 in 3.53 and simplifying, we get,

$$\frac{\rho_f}{\rho_0} = \frac{(\gamma+1)M_0^2}{(\gamma-1)M_0^2 + 2(1+(y_f^{'})^2)} \tag{3.56}$$

We know that from the continuity equation,

$$\rho_f v_{n_1} = \rho_0 v_{n_0} \;\; \rightarrow \;\; \therefore v_{n_1} = v_{n_0} \cdot \frac{\rho_0}{\rho_f}$$

Note that v_{n_0} is given by,

$$v_{n_0} = D_0 sin\theta = M_0 c_0 sin\theta = \frac{\sqrt{\gamma} M_0}{\sqrt{1+(y_f^{'})^2}}$$

Therefore, the v_{n_1} is given by,

$$v_{n_1} = \frac{\sqrt{\gamma} M_0}{\sqrt{1+(y_f^{'})^2}} \left(\frac{(\gamma-1)M_0^2 + 2(1+(y_f^{'})^2)}{(\gamma+1)M_0^2} \right) \tag{3.57}$$

By using v_{n_1} from equation (3.57) in (3.51) and simplifying, v_f is given by,

$$v_f = \frac{\sqrt{\gamma}\left[2(1+(y_f^{'})^2)+M_0^2(\gamma-1+(\gamma+1)(y_f^{'})^2)\right]}{(\gamma+1)M_0(1+(y_f^{'})^2)} \tag{3.58}$$

Similarly, u_f can be solved and is given by,

$$u_f = \frac{2\sqrt{\gamma}y_f^{'}(M_0^2-(1+(y_f^{'})^2))}{(1+(y_f^{'})^2)(\gamma+1)M_0} \tag{3.59}$$

The pressure p_f behind the shock front can be easily computed by normal shock jump conditions and is presented in equation (3.60).

$$\frac{p_f}{p_0} = \frac{2\gamma(M_N^2-1)}{\gamma+1}+1 = \frac{2\gamma(M_0^2-(1+(y_f^{'})^2))}{(\gamma+1)(1+(y_f^{'})^2)}+1 \tag{3.60}$$

The streamline slope F as a function of the shock slope $y_f^{'}$ is given by,

$$F = \frac{u_f}{v_f} = \frac{2\sqrt{\gamma}y_f^{'}(M_0^2-(1+(y_f^{'})^2))}{\sqrt{\gamma}\left[2(1+(y_f^{'})^2)+M_0^2(\gamma-1+(\gamma+1)(y_f^{'})^2)\right]} \tag{3.61}$$

The expression for $\frac{dF}{dy_f^{'}}$ can be easily evaluated by taking the derivative of equation (3.61). The parameters computed in this section correspond to the normal shock jump conditions. These parameters simplify to the expressions shown in Cartwright's thesis [51], where the lead shock is treated as a 'strong shock'.

3.5 Numerical Procedure

The process of obtaining the detonation structure starts by writing down the governing equations in the streamline-based coordinate system. These equations are derived in earlier sections and are given by (3.62), (3.63), (3.64) and (3.65), assuming straight yet diverging streamlines. These equations refer to the evolution of the flow's velocity in the direction of detonation propagation, reaction progress variable, density, and pressure on the arbitrarily chosen streamline (ψ = constant).

$$\left(\frac{\partial v}{\partial y}\right)_{\psi} = \frac{Q(\gamma-1)W - \left(\frac{\partial x}{\partial \psi}\right)_{y}^{-1} c^2 v \left(\frac{\partial^2 x}{\partial \psi \partial y}\right)}{\left[c^2 - v^2\left(1+\left(\frac{\partial x}{\partial y}\right)_{\psi}^{2}\right)\right]} \tag{3.62}$$

$$\left(\frac{\partial \lambda}{\partial y}\right)_{\psi} = \frac{W}{v} \tag{3.63}$$

$$\left(\frac{\partial \rho}{\partial y}\right)_{\psi} = \rho^2 v\left(\frac{\partial^2 x}{\partial \psi \partial y}\right) - \frac{\rho}{v}\left(\frac{\partial v}{\partial y}\right)_{\psi} \tag{3.64}$$

$$\left(\frac{\partial p}{\partial y}\right)_{\psi} = -\rho v\left(\frac{\partial v}{\partial y}\right)_{\psi}\left[1+\left(\frac{\partial x}{\partial y}\right)^{2}\right] \tag{3.65}$$

The different terms displayed in the governing equations are derived and presented in earlier sections. The initial conditions for these governing equations are presented here as follows,

$$v_f = \frac{\sqrt{\gamma}(2(1+(y_f^{'})^2)+M_s^2(\gamma-1+(\gamma+1)(y_f^{'})^2))}{(\gamma+1)M_s(1+(y_f^{'})^2)} \tag{3.66}$$

$$\lambda_f = 0 \tag{3.67}$$

$$\rho_f = \frac{(\gamma+1)M_s^2}{(\gamma-1)M_s^2 + 2(1+(y_f^{'})^2)} \tag{3.68}$$

$$p_f = \frac{2\gamma(M_s^2 - (1+(y_f^{'})^2))}{(\gamma+1)(1+(y_f^{'})^2)} + 1 \tag{3.69}$$

The first step is to assume a value for the detonation speed such that $D_0 < D_{CJ}$. This D_0 will correspond to the Mach number M_0 of the steady propagating detonation wave. We then start integrating the equations from the central streamline where x_f = 0, y_f = 0, $x = 0$ and initial slope $y_f^{'} = 0$. The governing equation now becomes the eigenvalue problem. The solution is provided by matching the generalized CJ-condition by varying the only parameter left in the governing equations - $y_f^{''}$, i.e., shock curvature at the central streamline. Once we have the shock curvature for that streamline, we can integrate out along the shock using a Taylor expansion around the point (x_f,y_f) to find the shock slope and position of the next streamline by following equations,

$$y_f^{n+1} = y_f^n + \frac{dy_f}{dx_f}^n \Delta x_f + \frac{1}{2}\frac{d^2y_f}{dx_f^2}^n \Delta x_f^2 \tag{3.70}$$

$$\frac{dy_f}{dx_f}^{n+1} = \frac{dy_f}{dx_f}^n + \frac{d^2y_f}{dx_f^2}^n \Delta x_f \tag{3.71}$$

$$x_f^{n+1} = x_f^n + \Delta x_f \tag{3.72}$$

After reaching the next streamline and evaluating initial conditions for that streamline, the governing equations are solved again to obtain shock curvature $y_f^{''}$. The integration along the shock-front is done until we have reached the boundary value of the shock slope. The process of evaluating boundary shock slope $y_{f_{cr}}^{'}$ is described in the next section.

The process gives shock-front structure, sonic locus, charge-width (h) and spatial evolution of thermodynamic parameters in the reaction zone structure, for a given velocity deficit. Solving this problem for different D_0 will thus give us the diameter-effect curve for the chosen reactive charge - confiner couple.

3.6 Boundary Conditions

The boundary conditions at the reactive charge edge are described in this section. The origin lies at the intersection of the central streamline with the shock front, as shown in Figure 3.3. The slope of the shock front at the central streamline $y_f^{'}(x_f = 0) = 0$. The streamline slope after the shock is $F(x = 0) = 0$, as the central streamline does not undergo any deflection, evident in Figure 3.3.

The boundary condition at the charge edge for the case where the acoustic impedance ratio $Z = \frac{\rho_r c_r}{\rho_i c_i} = 1$ is given by the fact that the velocity of the incoming reactive flow of gases is sonic immediately after the shock [52]. As the slope of the shock front governs the thermodynamic parameters immediately behind the shock, the

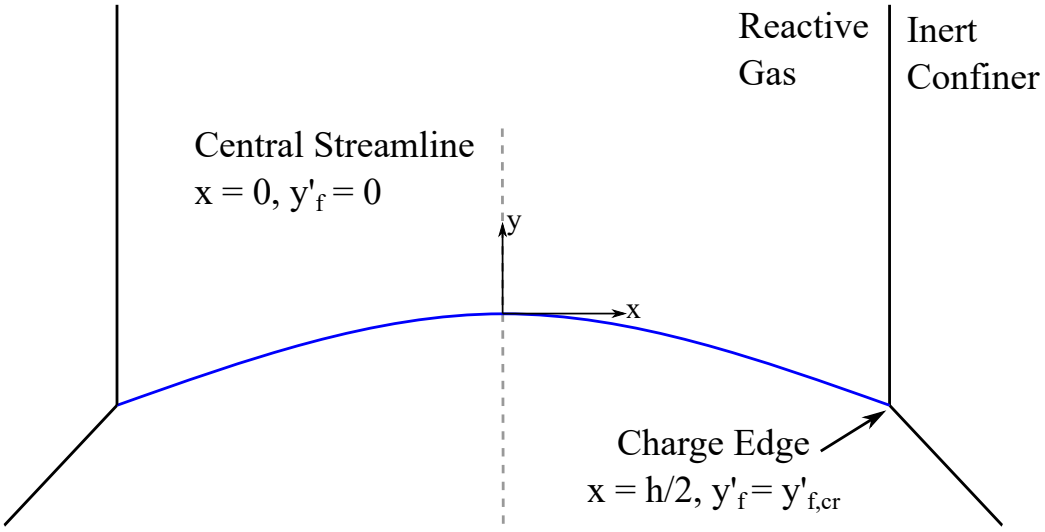

Figure 3.3: Schematic of the boundary conditions at the central streamline and at charge edge

boundary condition at the charge edge is given by a peculiar value of shock slope $y'_{f_{cr}}$.

For confined detonations where acoustic impedance ratio $Z \neq 1$, the post-shock pressure is matched via shock-polar analysis to obtain the critical shock slope value [53].

We have considered the cases only where $Z = 1$; thus, the boundary condition becomes the sonic conditions just behind the shock front. The idea is to integrate along the shock front until we reach the value of the shock slope $y'_{f_{cr}}$ that corresponds to the sonic point behind the shock front. We know that the slope of the shock front increases as we move away from the charge axis to the charge edge. However, we cannot integrate along the shock front until the sonic-point rule as the shock slope value corresponding to maximum streamline deflection is smaller

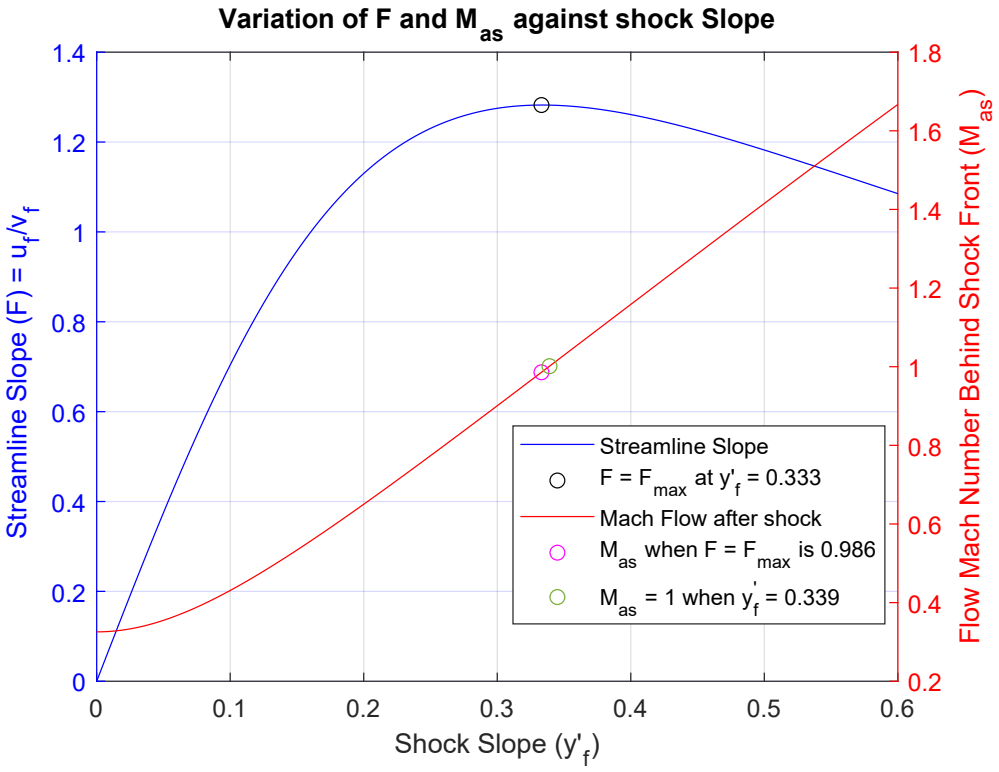

Figure 3.4: Variation of Streamline slope (F) and Mach number (M_{as}) of the flow behind the shock front as we progress from $y_f^{'} = 0$, i.e. central streamline to charge edge for $Q/RT_0 = 50$, $\gamma = 1.2$ and $D_s/D_{CJ} = 0.98$.

in magnitude than the ideal sonic-point rule. Integrating further after this point, along the shock, will relatively cause streamlines to converge and intersect downstream, which is physically not possible. This phenomenon is briefly displayed in Figure 3.4.

Figure 3.4 shows the slope of the streamline, given by 3.73, against the slope of the shock-front for the case where $Q/RT_0 = 50$, $\gamma = 1.2$ and $D/D_{CJ} = 0.98$. We can see that streamlines start to converge after a specific value of shock slope,

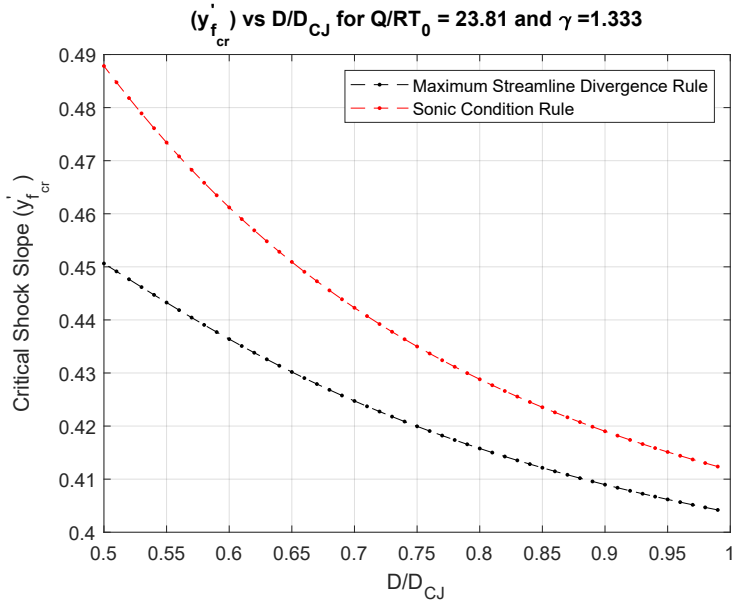

Figure 3.5: Boundary shock slope obtained from sonic-condition and maximum streamline divergence criteria for $Q/RT_0 = 23.81$ and $\gamma = 1.333$.

as shown in Figure 3.4. The Mach number of the flow just behind the shock-front, denoted by M_{as}, against the shock-slope value is also presented in Figure 3.4 for the same parameters. For this case, we can see that the peak divergence of the streamline is achieved before than sonic point $M_{as} = 1$. Thus, one can not march along the increasing value of shock slope after the maximum divergence of streamlines as it will lead the streamlines to cross each other downstream, which is non-physical.

$$F = \frac{u_f}{v_f} = \frac{2(M_s^2 - (1 + (y_f^{'})^2))}{(2(1 + (y_f^{'})^2) + (M_s^2(\gamma - 1 + (\gamma + 1)(y_f^{'})^2)))} \tag{3.73}$$

In the cases considered, we have integrated up to the shock slope corresponding

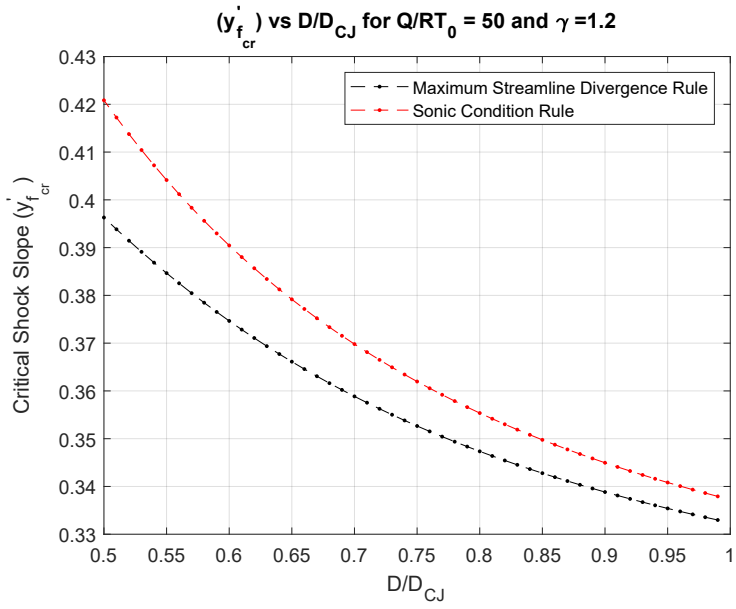

Figure 3.6: Boundary shock slope obtained from sonic-condition and maximum streamline divergence criteria for $Q/RT_0 = 50$ and $\gamma = 1.2$.

to maximum streamline divergence. Figure 3.5 and Figure 3.6 corresponds to the sonic-locus boundary condition and maximum streamline divergence boundary condition for various D/D_{CJ} values for a) $Q/RT_0 = 23.81$ and $\gamma = 1.333$, and b) $Q/RT_0 = 50$ and $\gamma = 1.2$. These two cases are picked so that a comparison of models with existing numerical calculations can be made [23, 24].

It is evident from the Figures that by using the 'Maximum Streamline Divergence Rule', one can relatively obtain the 'all but a negligible amount' of the overall detonation structure. Thus, selecting this criterion as the boundary condition in our study is appropriate.

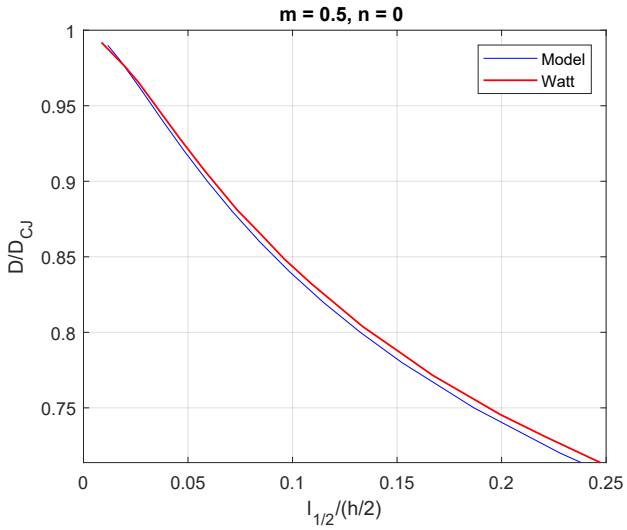

Figure 3.7: Comparison of the SSA model of Diameter effect curve for m = 0.5 and n = 0 with Watt's results [22].

3.7 Model Verification

This subsection refers to the validation of the SSA model with the existing results in the literature. The first attempt to model the solid explosives by this Straight Streamline Approximation (SSA) was performed by Watt et al. [22]. The energy release is governed by the pressure-dependent rate law, given by equation (3.74).

$$\frac{d\lambda}{dy} = \frac{W}{v} = k\,p^n\,(1-\lambda)^m \tag{3.74}$$

The initial conditions for the governing equations were derived by assuming strong shock conditions, i.e., $M_0 >> 1$. The exponent parameters m and n are changed to obtain the diameter-effect curve for various energy-release equations. As shown in Figures 3.7, 3.8, 3.9, 3.10 and 3.11, the results obtained by the model developed

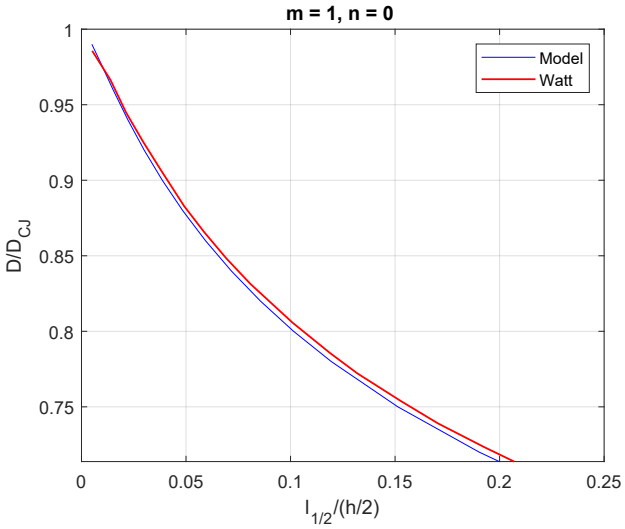

Figure 3.8: Comparison of the SSA model of Diameter effect curve for m = 1 and n = 0 with Watt's results [22].

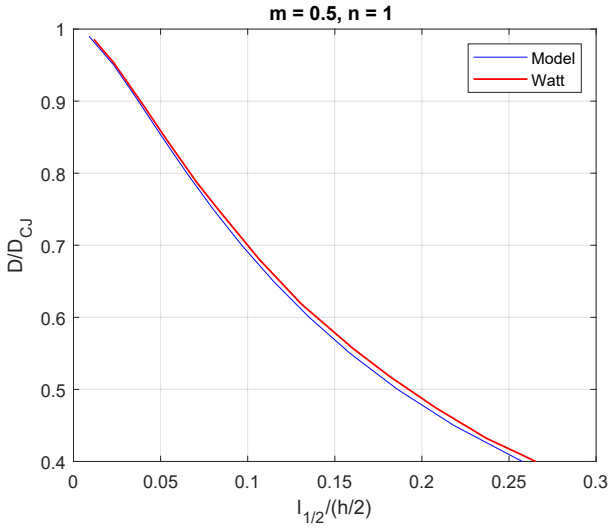

Figure 3.9: Comparison of the SSA model of Diameter effect curve for m = 0.5 and n = 1 with Watt's results [22].

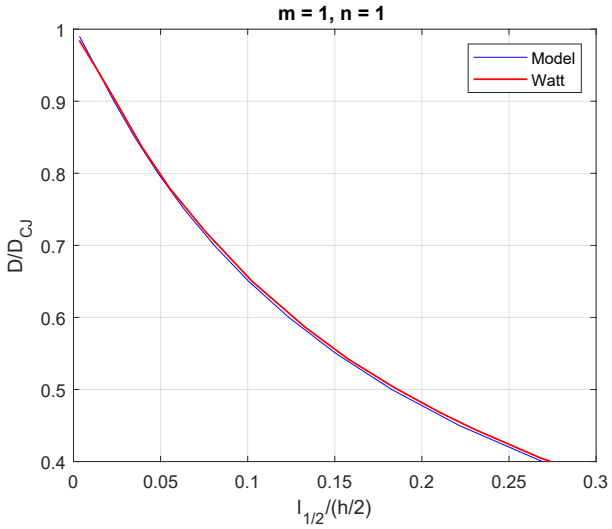

Figure 3.10: Comparison of the SSA model of Diameter effect curve for m = 1 and n = 1 with Watt's results [22].

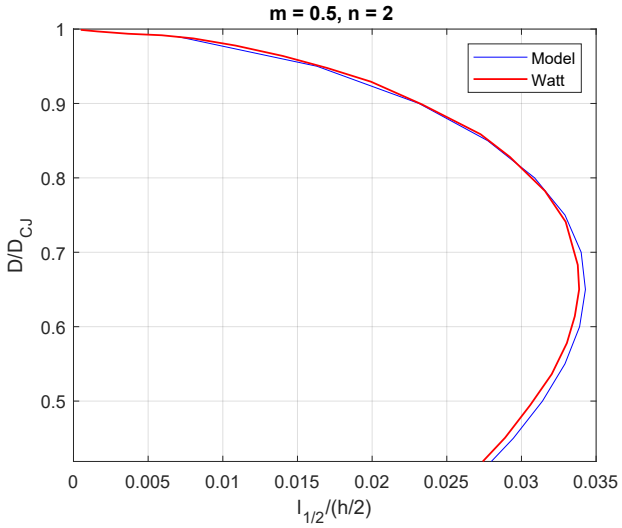

Figure 3.11: Comparison of the SSA model of Diameter effect curve for m = 0.5 and n = 2 with Watt's results [22].

here are compared against Watt's result to verify our implementation. The minor variation between the results can be attributed to the difference in the numerical method employed.

The integration along the shock-front is chosen so that $\Delta y_f^{'} = 0.005$. The reason for choosing this value for marching along the front is the relatively small change in curves for $\Delta y_f^{'} < 0.005$ shown in Figure 3.12 for the case of $m = 1$ and $n = 1$. The results move towards the right upon decreasing the step size in $\Delta y_f^{'}$.

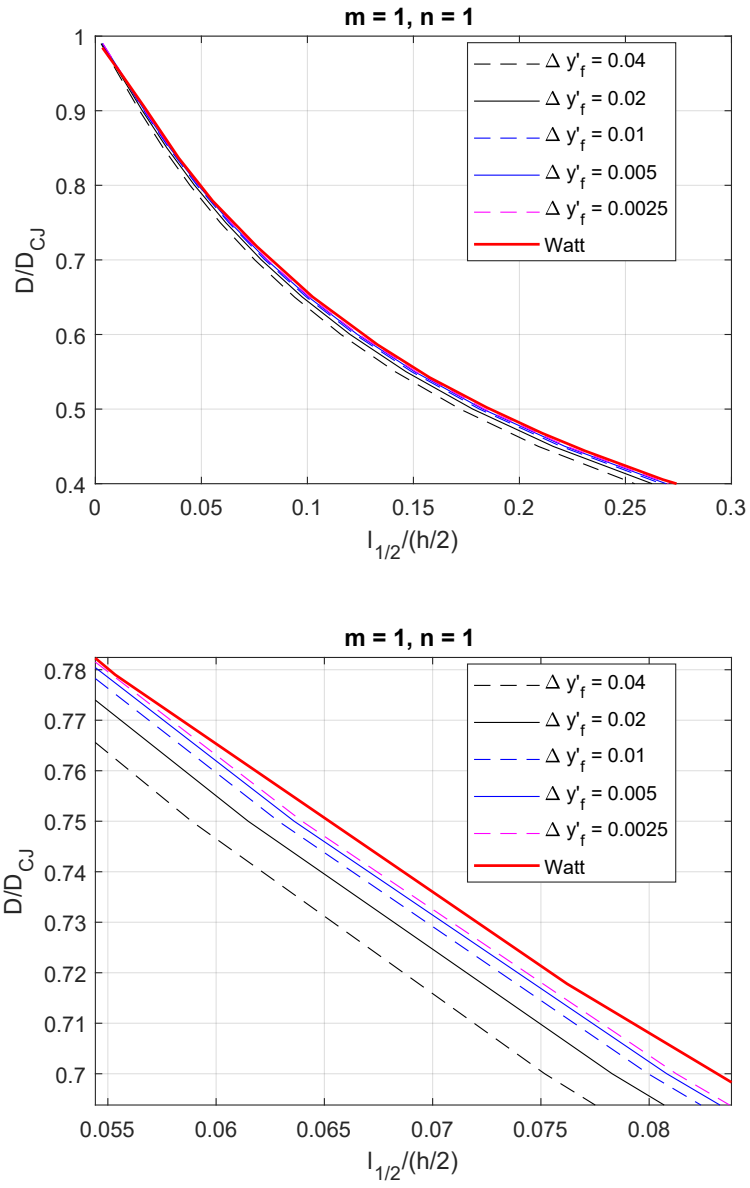

Figure 3.12: Effect of Varying $\Delta y_f^{'}$ on the D/D_{CJ} *vs* $l_{1/2}/(h/2)$ curves for $m = 1$ and $n = 1$.

3.8 Results

This section provides the results obtained using the SSA model for gaseous detonations that are weakly confined by an inert gas. Table 3.1 summarizes the cases and relevant parameters for which results are obtained. The chemistry of the reactants burning is given by the Arrhenius 1-step model, mathematically represented in equation (3.75). The numerical calculations against which the results of this model are compared have also employed the same rate law.

$$\frac{d\lambda}{dy} = \frac{k(1-\lambda)e^{-E_a\frac{\rho}{p}}}{v} \tag{3.75}$$

Sr No	E_a/RT_0	Q/RT_0	γ	Reference
1	10	23.81	1.333	[23]
2	20	23.81	1.333	[23]
3	30	23.81	1.333	[23]
4	38.23	23.81	1.333	[23]
5	10	50	1.2	[24]
6	20	50	1.2	[24]
7	30	50	1.2	[24]

Table 3.1: Different values of E_a/RT_0, Q/RT_0 and γ taken from literature [23, 24].

The structure of detonation, depicting shock front and sonic locus for $Q/RT_0 = 23.81$, $E_a/RT_0 = 10$ and $D/D_{CJ} = 0.98$ is displayed in Figure 3.13. It is noticed that the sonic locus does not meet the shock front at the charge edge. This disparity has arisen as we cannot integrate along the shock until the sonic point as streamline starts converge earlier than the sonic point boundary condition, as de-

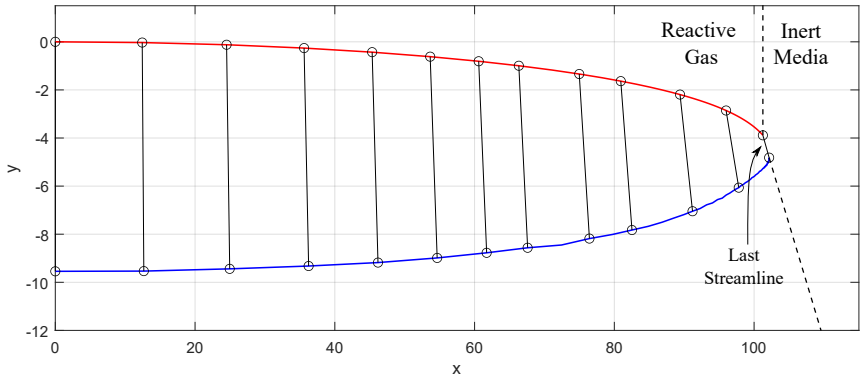

Figure 3.13: Structure of detonation obtained from the SSA Model for $Q/RT_0 = 23.81$, $E_a/RT_0 = 10$ and $D/D_{CJ} = 0.98$.

scribed in section 3.6. Figure 3.5 argues this in detail. The relevant detonation structure of detonation for other cases is shown in Appendix A.

The diameter-effect curves for the cases considered are shown in Figures 3.14, 3.15, 3.16, 3.17, 3.18, 3.19 and 3.20.

For $E_a/RT_0 = 10$, the SSA model is in excellent agreement with the numerical simulations of Mi and Reynaud [23, 24]. At this low activation energy, both the SSA model and the numerical calculations of Mi et al. [24] do not predict extinction, which would be marked by a turning point in the thickness effect curve. As the activation energy increases, this agreement starts to deteriorate, as evidenced in the results presented in Figures 3.15-3.17. Thus, the model can predict the velocity of detonations for lower activation energies but fails for higher activation energies. This discrepancy is due to the delayed burning of reactants for high-activation energy cases and irregular cellular structure, which are not accounted for in the macroscopic kinetic model.

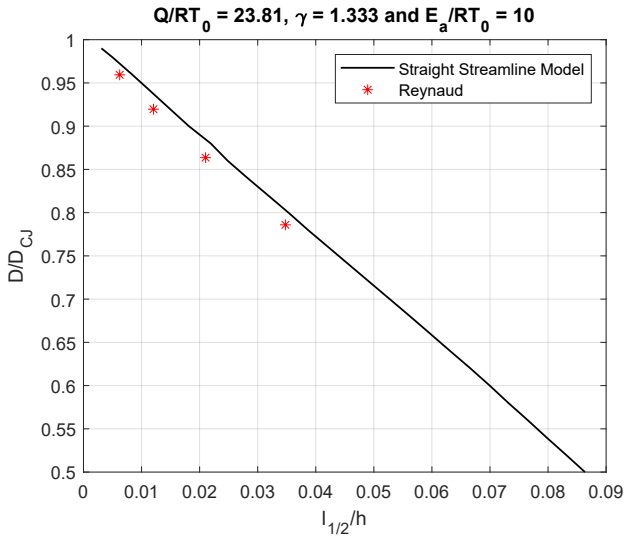

Figure 3.14: Comparison of diameter effect curve obtained from the SSA model for $Q/RT_0 = 23.81$, $\gamma = 1.333$, and $E_a/RT_0 = 10$ with Reynaud's results [23].

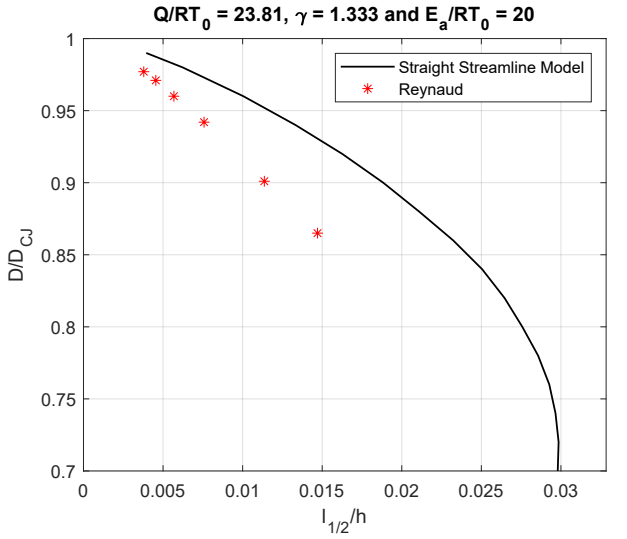

Figure 3.15: Comparison of diameter effect curve obtained from the SSA model for $Q/RT_0 = 23.81$, $\gamma = 1.333$, and $E_a/RT_0 = 20$ with Reynaud's results [23].

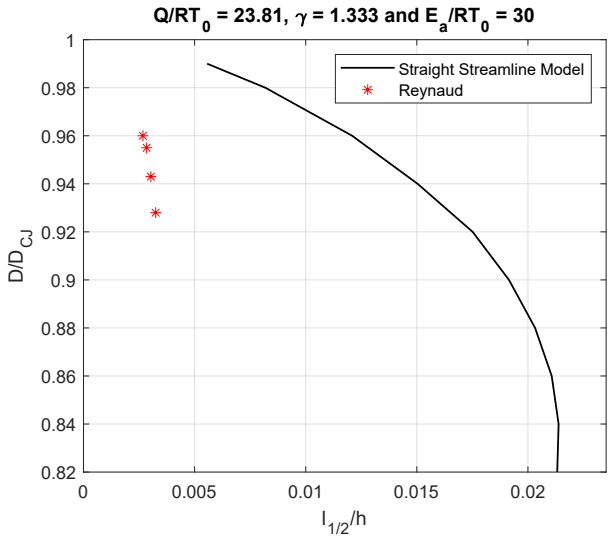

Figure 3.16: Comparison of diameter effect curve obtained from the SSA model for $Q/RT_0 = 23.81$, $\gamma = 1.333$, and $E_a/RT_0 = 30$ with Reynaud's results [23].

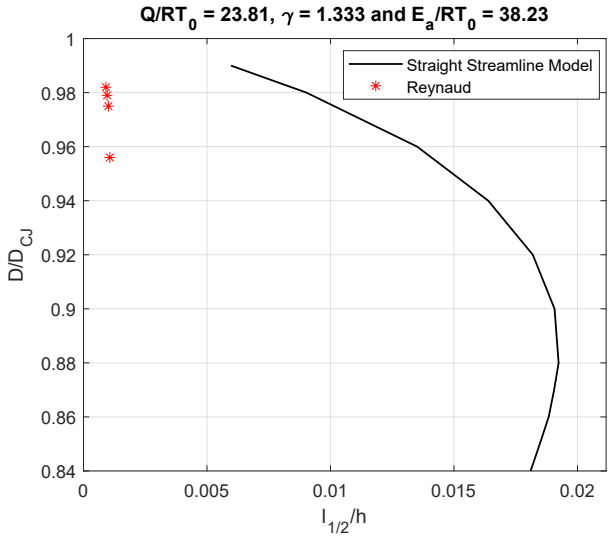

Figure 3.17: Comparison of diameter effect curve obtained from the SSA model for $Q/RT_0 = 23.81$, $\gamma = 1.333$, and $E_a/RT_0 = 38.23$ with Reynaud's results [23].

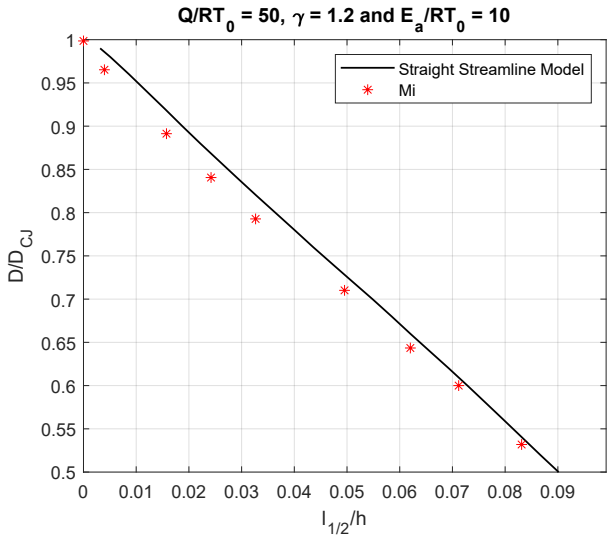

Figure 3.18: Comparison of diameter effect curve obtained from the SSA model for $Q/RT_0 = 50$, $\gamma = 1.2$, and $E_a/RT_0 = 10$ with Mi's results [24].

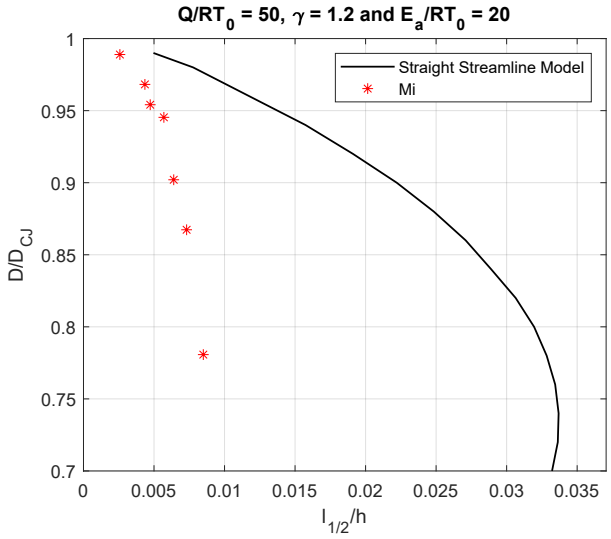

Figure 3.19: Comparison of diameter effect curve obtained from the SSA model for $Q/RT_0 = 50$, $\gamma = 1.2$, and $E_a/RT_0 = 20$ with Mi's results [24].

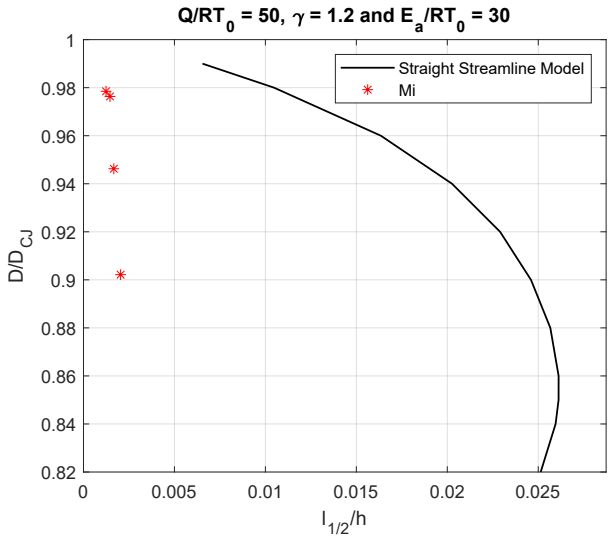

Figure 3.20: Comparison of diameter effect curve obtained from the SSA model for $Q/RT_0 = 50$, $\gamma = 1.2$, and $E_a/RT_0 = 30$ with Mi's results [24].

Chapter 4

Quasi 1-D Model

4.1 Introduction

In this chapter, we treat a further simplification of the SSA model. We assume a single equivalent streamtube, for which the rate of global divergence is taken as the average of the distribution. It is a simple extension of the Wood-Kirkwood model, first proposed by Radulescu et al. [8] in the context of detonations in porous wall tubes. The simple conceptual model for the detonation propagation in the presence of weak confinement is shown in Figure 4.1. The planar shock front is moving steadily in a fixed width of reactants. The reactants are confined by inert material on its side. The flow in the reaction zone is approximated by classic quasi-1D flow with area changes. The increase in the pressure in the reaction zone of such detonation causes the contact surface to move laterally, away from the charge axis. This lateral area divergence causes the detonation to propagate at

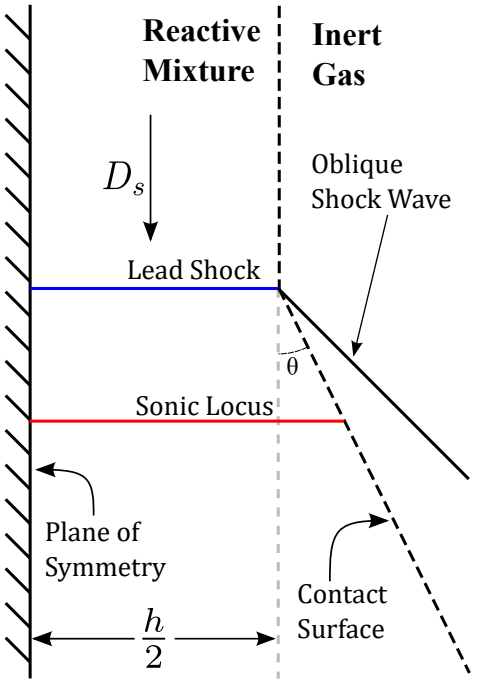

Figure 4.1: Schematic of a one-dimensional detonation interacting with an inert layer.

a velocity less than the CJ one.

This chapter provides the simpler Quasi 1-D model to predict the effect of expanding reaction zone on steady propagation velocity. Section 4.2 describes the steady one-dimensional reactive Euler equations which govern the flow fields from the von-Neumann state to the sonic locus. The Quasi 1-D model is developed to account for the loss term in the governing equations and is presented in section 4.3. The relevant results are reported in section 4.4.

4.2 Governing Equations

The steady form of the conservation of mass, momentum, and energy written in conservative form is given by,

$$\frac{d}{dy}(\rho v A) = 0 \tag{4.1}$$

$$\frac{d}{dy}\left[A\left(p+\rho v^2\right)\right] = p\frac{1}{A}\frac{dA}{dy} \tag{4.2}$$

$$\frac{d}{dy}\left(h+\frac{1}{2}v^2\right) = 0 \tag{4.3}$$

For simplicity, we assume an Arrhenius 1-step rate law. It is important to note that these equations are ODEs because there is only one independent variable - flow propagation direction in the shock-connected reference frame. These equations, given by 4.1-4.3, are combined with the rate law, equation of state, the sound speed relation for ideal gas and ideal gas law, given by 4.4-4.6, to solve the problem.

$$\frac{d\lambda}{dy} = \frac{W}{v} = \frac{k(1-\lambda)e^{-E_a\frac{\rho}{p}}}{v} \tag{4.4}$$

$$h = \frac{\gamma P}{(\gamma-1)\rho} - Q\lambda \tag{4.5}$$

$$c^2 = \frac{\gamma p}{\rho} \tag{4.6}$$

After simplifying equations (4.1)-(4.6), we can obtain the ODEs that provide the evolution of velocity, pressure, density, and reaction progress variable. The governing equations are given by (4.7)-(4.10).

$$\frac{dv}{dy} = \frac{(\gamma-1)Qv\frac{d\lambda}{dy} - c^2 v\frac{1}{A}\frac{dA}{dy}}{c^2 - v^2} \tag{4.7}$$

$$\frac{d\rho}{dy} = -\frac{\rho}{v}\left(\frac{dv}{dy} + \frac{v}{A}\frac{dA}{dy}\right) \tag{4.8}$$

$$\frac{dp}{dy} = -\rho v\frac{dv}{dy} \tag{4.9}$$

$$\frac{d\lambda}{dy} = \frac{k(1-\lambda)e^{-E_a\frac{\rho}{p}}}{v} \tag{4.10}$$

Here, v is the flow velocity, ρ is the density of reactive gas, p is the pressure of charge, λ is the reaction progress variable, γ is the ratio of specific heats, Q is the total heat release when reactants convert to products, c is the local speed of sound, k pre-exponential factor, E_a is the activation energy corresponding to reactive gas, R is the gas constant, T is the temperature and y is the direction of propagation of incoming reactants in the shock-attached frame of reference.

The initial conditions correspond to the von-Neumann state and are given by equations (4.11)-(4.14).

$$\frac{p_f}{p_0} = \frac{2\gamma(M_0^2-1)}{(\gamma+1)} + 1 \tag{4.11}$$

$$\frac{\rho_f}{\rho_0} = \frac{(\gamma+1)M_0^2}{2+(\gamma-1)M_0^2} \tag{4.12}$$

$$\frac{v_f}{v_0} = \frac{\rho_0}{\rho_{VN}} \ , \ v_0 = M_0 c_0 = M_0\sqrt{\frac{\gamma p_0}{\rho_0}} \tag{4.13}$$

$$\lambda_f = 0 \tag{4.14}$$

The governing equations can be solved to obtain a one-dimensional solution to the problem. The issue lies in the quantification of loss term $\frac{1}{A}\frac{dA}{dy}$, which physically means the lateral area divergence experienced in the reaction zone structure of the confined detonation. The loss term is modelled by the Quasi 1-D model which is described in detail in section 4.3.

4.3 Quasi 1-D Model

In order to solve these problems, the term $\frac{1}{A}\frac{dA}{dy}$ must be taken into account. As seen in Figure 4.2, the loss term contributing to area divergence is given by equation (4.15), where h is the height of the reactive charge, t is one-dimensional slab thickness, which does not vary with y.

$$\frac{1}{A}\frac{dA}{dy} = \frac{1}{(h/2)\cdot t}\frac{d[(h/2)\cdot t]}{dy} = \frac{2}{h}\,tan\theta \tag{4.15}$$

The equation (4.15) interprets that the fraction of energy generated in the reac-

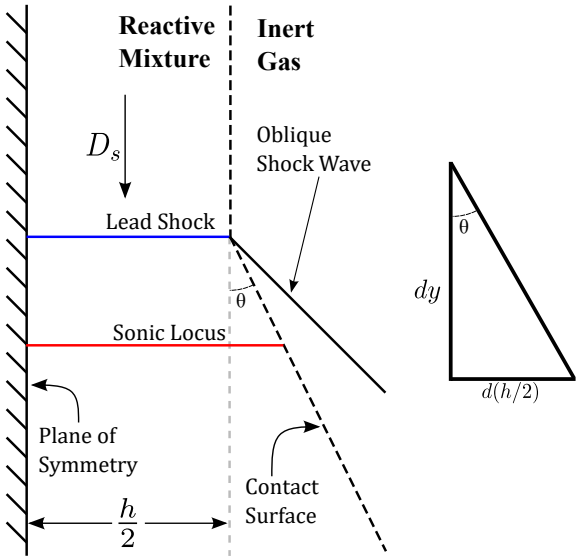

Figure 4.2: Lateral area divergence in the Quasi-one-dimensional model.

tion zone is lost to the confiner increases as the charge thickness decreases and increases with an effective increase in deflection angle θ. Here we model the loss term pertinent for a 1-D description of confined detonation by taking the mean flow divergence in the SSA model. The simple way of quantifying the mean flow divergence in the SSA model is by obtaining the mean of flow divergence experienced by the central streamline and the last streamline, which corresponds to maximum flow divergence in our SSA model formalism, as shown mathematically in equation (4.16).

$$\left(\frac{1}{A}\frac{dA}{dy}\right)_{Q1D} = \frac{\left[\left(\frac{1}{A}\frac{dA}{dy}\right)_{SSA,central} + \left(\frac{1}{A}\frac{dA}{dy}\right)_{SSA,last}\right]}{2} \tag{4.16}$$

We know that the central streamline does not deflect in the SSA model; thus, from

equation (4.15), we get,

$$\left(\frac{1}{A}\frac{dA}{dy}\right)_{SSA_{cental}} = \frac{2}{h}\,tan\theta = \frac{2}{h}\tan(0) = 0 \tag{4.17}$$

Thus, Upon further evaluating equation (4.16), we get

$$\left(\frac{1}{A}\frac{dA}{dy}\right)_{Q1D} = \frac{(2/h)\cdot tan(\theta_{SSA})}{2} \tag{4.18}$$

Here, θ_{SSA} is the flow deflection angle of the last streamline, as shown in figure 4.3. The equation can be further simplified as we know that $tan(\theta_{SSA})$ is the slope of the last streamline in the SSA model. Thus the loss term for 1-D description can be simplified to,

$$\left(\frac{1}{A}\frac{dA}{dy}\right)_{Q1D} = \frac{1}{2}\cdot\left(\frac{2}{h}\cdot\left(\frac{u_f}{v_f}\right)_{last}\right) = \frac{1}{2}\cdot\left(\frac{2}{h}\cdot(F)_{last}\right) = \frac{F_{max}}{h} \tag{4.19}$$

Thus, the equation (4.19) represents the effective lateral area divergence experienced by a weakly confined gaseous detonation. The $F_{last} = F_{max}$ as in our SSA model formalism; the last streamline has the maximum streamline slope (F). The F_{max} can be evaluated from the equation (3.61) for a critical value of shock slope at a fixed detonation speed.

Following the loss term's quantification and the initial conditions' definition, the velocity of detonation is assumed (M_0). The setup is now an eigenvalue problem, the solution of which gives the correct charge height h for the assumed detonation velocity. The initial pressure, density and half-reaction zone length of the ZND solution are chosen to non-dimensionalize the system. The procedure is

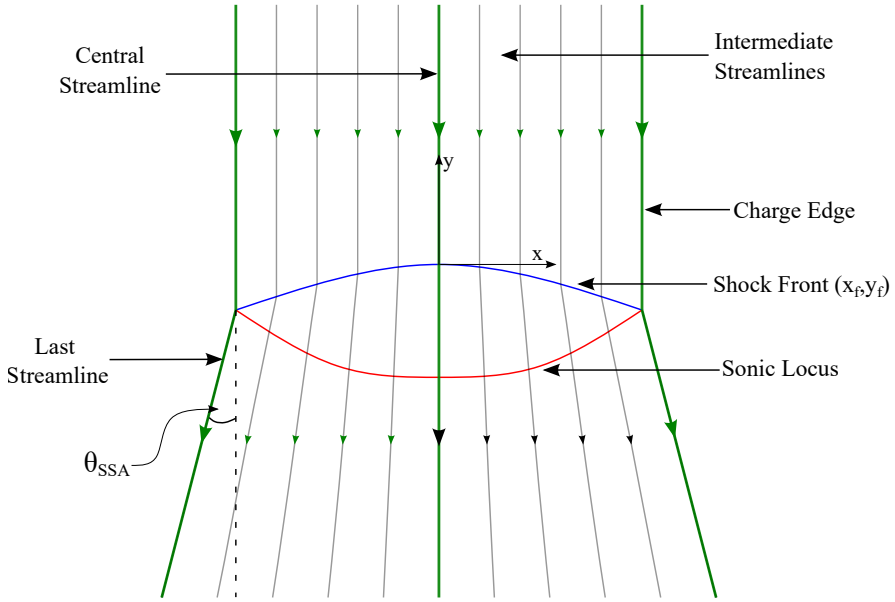

Figure 4.3: Schematic of lateral flow divergence of steady detonation as defined in the SSA model.

repeated for the multiple detonation velocities that are lesser in magnitude than the CJ detonation velocity. The final answer provides the Diameter-Effect curve (D/D_{CJ} *vs* $l_{1/2}/h$) for the given reactive gas and inert layer.

4.4 Results and Discussion

The results of the Quasi 1-D model are compared with the SSA model and the numerical simulations of Reynaud et al. [23] and Mi et al. [24].

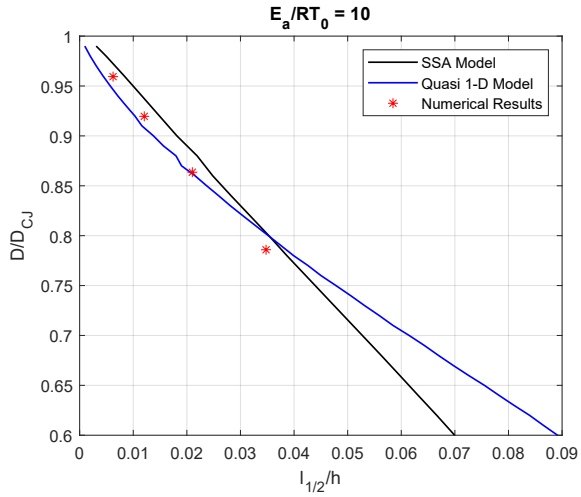

Figure 4.4: Velocity deficit curves for the Quasi 1-D model (blue line), the SSA model (black line) and numerical results of Reynaud [23] for $E_a/RT_0 = 10$.

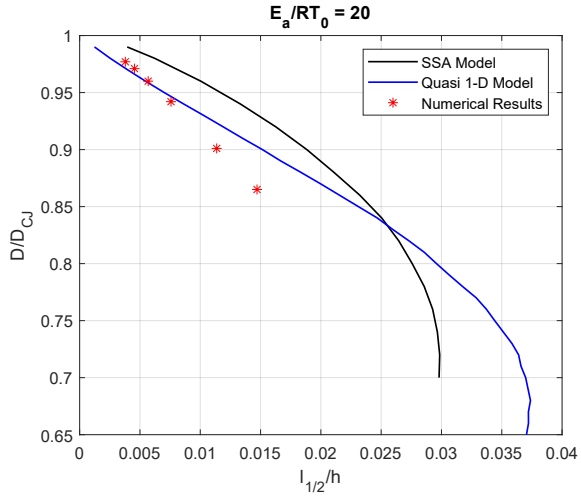

Figure 4.5: Velocity deficit curves for the Quasi 1-D model (blue line), the SSA model (black line) and numerical results of Reynaud [23] for $E_a/RT_0 = 20$.

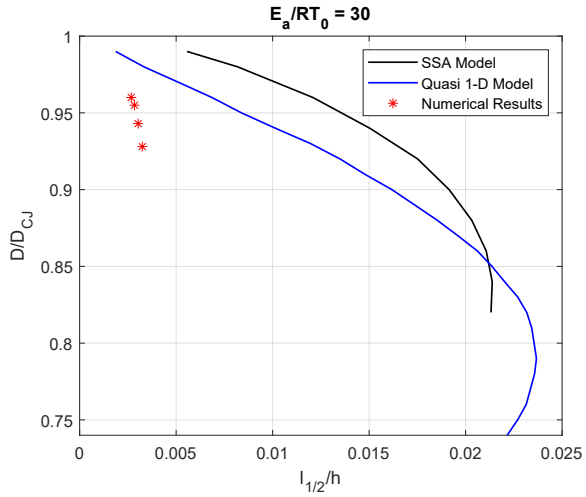

Figure 4.6: Velocity deficit curves for the Quasi 1-D model (blue line), the SSA model (black line) and numerical results of Reynaud [23] for $E_a/RT_0 = 30$.

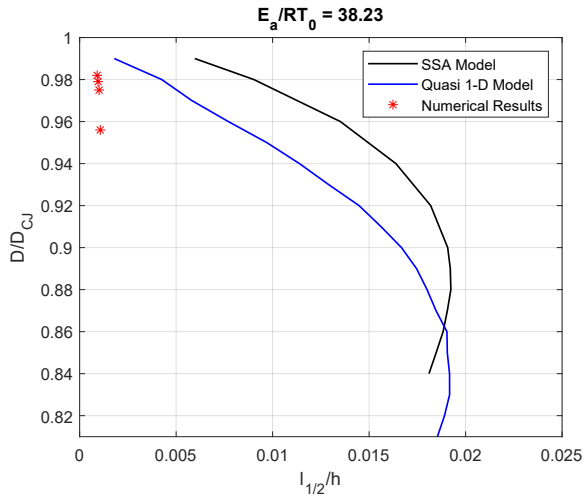

Figure 4.7: Velocity deficit curves for the Quasi 1-D model (blue line), the SSA model (black line) and numerical results of Reynaud [23] for $E_a/RT_0 = 38.23$.

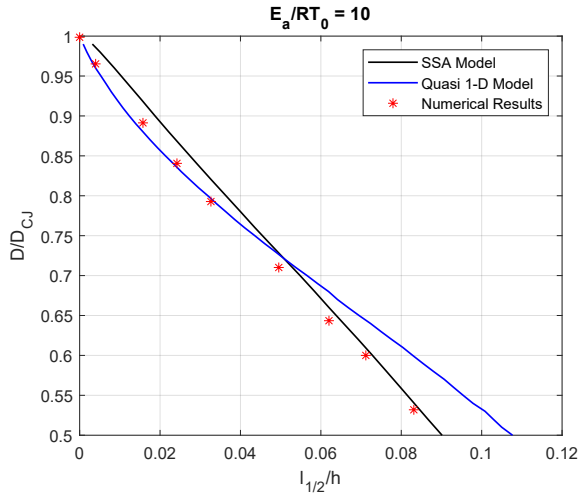

Figure 4.8: Velocity deficit curves for the Quasi 1-D model (blue line), the SSA model (black line) and numerical results of Mi [24] for $E_a/RT_0 = 10$.

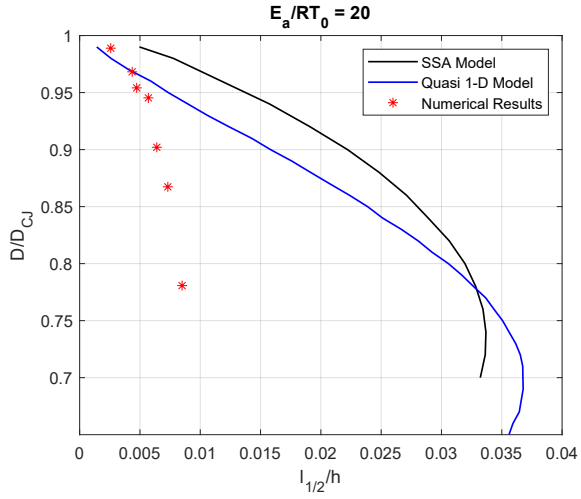

Figure 4.9: Velocity deficit curves for the Quasi 1-D model (blue line), the SSA model (black line) and numerical results of Mi [24] for $E_a/RT_0 = 20$.

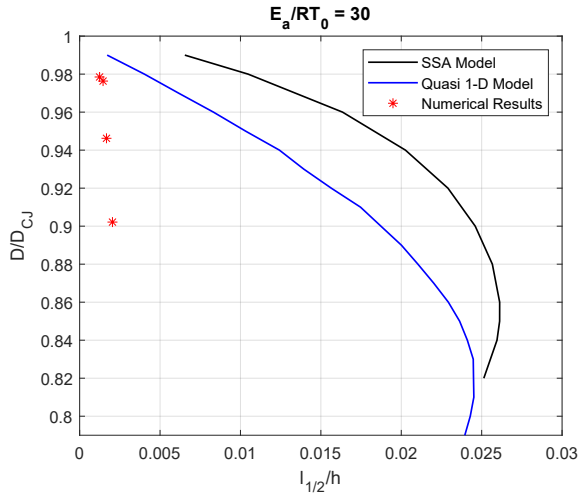

Figure 4.10: Velocity deficit curves for the Quasi 1-D model (blue line), the SSA model (black line) and numerical results of Mi [24] for $E_a/RT_0 = 30$.

Figures 4.4-4.10 show that the Quasi 1-D model agrees with the SSA model. However, both analytical models fail to capture the velocity trends for the case when activation energy is high. It is due to the growing instabilities and significant effect of cellular structure on the dynamics of weakly confined detonations, especially for high activation energies. The effect of cellular structure on the delayed burning of reactions is modelled in chapter 5.

Chapter 5

Modelling of Cellular Structure

5.1 Introduction

The results presented in the previous chapters showed that the prediction of the laminar reaction zone model over-estimates the results obtained for cellular detonations. This observation is due to the significant lengthening of the global reaction zone due to the cellular structure, as reviewed in the Chapter 2. In the present chapter, we present two models for the reaction zone. Their incorporation in the SSA model results in excellent agreement with the results of cellular detonations. First, an empirical approach is described to quantify the delayed-energy release present in unstable detonations in section 5.2. Then, an analysis of the effective kinetic slow-down of such detonations from numerical results of Reynaud [23] is presented in section 5.3. Next, a physical model incorporating the ignition-delay properties in detonations characterized by higher activation energies is developed

to account for slow energy generation in the reaction zone in section 5.4. Finally, these three approaches that account for the slow-burning of reactants in irregular detonations restricted by non-reactive gases are analyzed.

5.2 Empirical Modelling of Rate Law

The delayed energy release in unstable detonations, characterized by high reduced activation energies, can be modelled by modelling the rate-law term. Here, in our approach, the rate law is scaled down for all the cases on hand to match the diameter-effect curves of the SSA model and the Quasi 1-D model with the existing numerical simulations [23, 24]. The scaling factor S is given by,

$$\frac{d\lambda}{dy} = \frac{k}{\mathbf{S}} \cdot \frac{(1-\lambda)e^{-E_a\rho/p}}{v} \tag{5.1}$$

The diameter effect curves show the relationship between the steady velocity of non-ideal detonations and charge thickness. The scaling of rate law has linear dependency on the velocity deficit curves. The rate law that governs the chemical energy release is slowed down by factor S until the analytical model matches the numerical simulations, mathematically shown in equation (5.2). The n is the total number of points on the velocity deficit curve of numerical simulations. The relative departure of the analytical model at each of the observation points is noted, and the mean of them gives us the global thickening parameter - S.

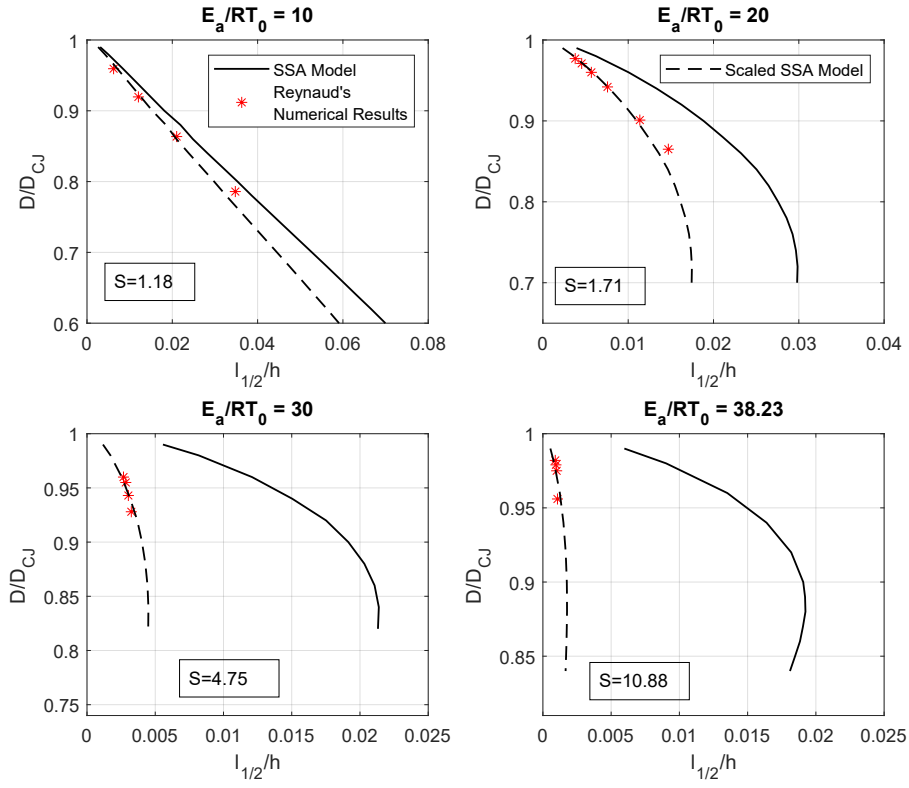

Figure 5.1: Scaling of the SSA model for $Q/RT_0 = 23.81$, $\gamma = 1.333$, with Reynaud's results [23].

$$S = \frac{\sum_1^n \frac{(1/h)_{Model}}{(1/h)_{NS}}}{n} \tag{5.2}$$

5.2.1 Results

The scaling of the rate law to match the SSA model's result with the existing numerical simulations is shown in Figures 5.1 and 5.2. The relevant results for the Quasi 1-D models are shown in Figures 5.3 and 5.4.

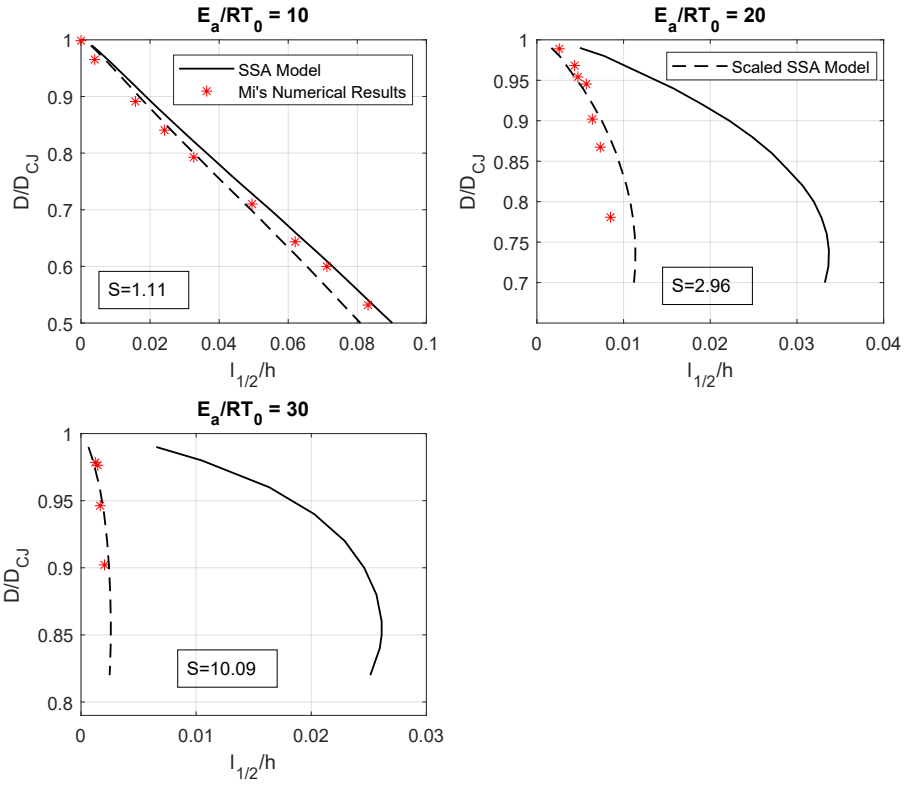

Figure 5.2: Scaling of the SSA model for $Q/RT_0 = 50$, $\gamma = 1.2$, with Mi's results [24].

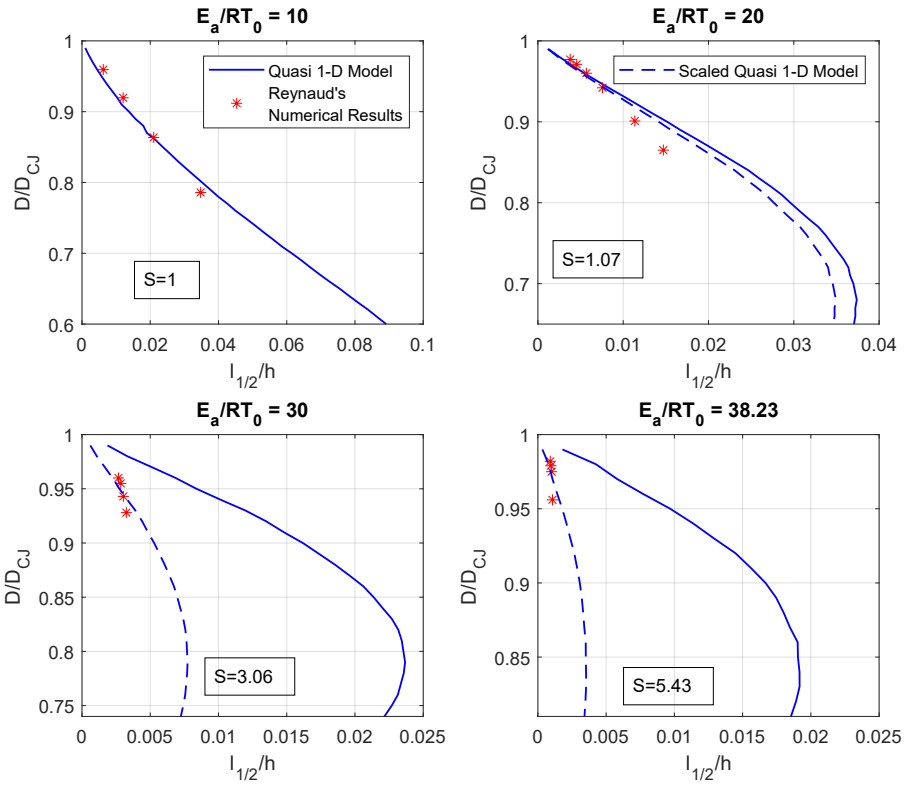

Figure 5.3: Scaling of the Quasi 1-D model for $Q/RT_0 = 23.81$, $\gamma = 1.333$, with Reynaud's results [23].

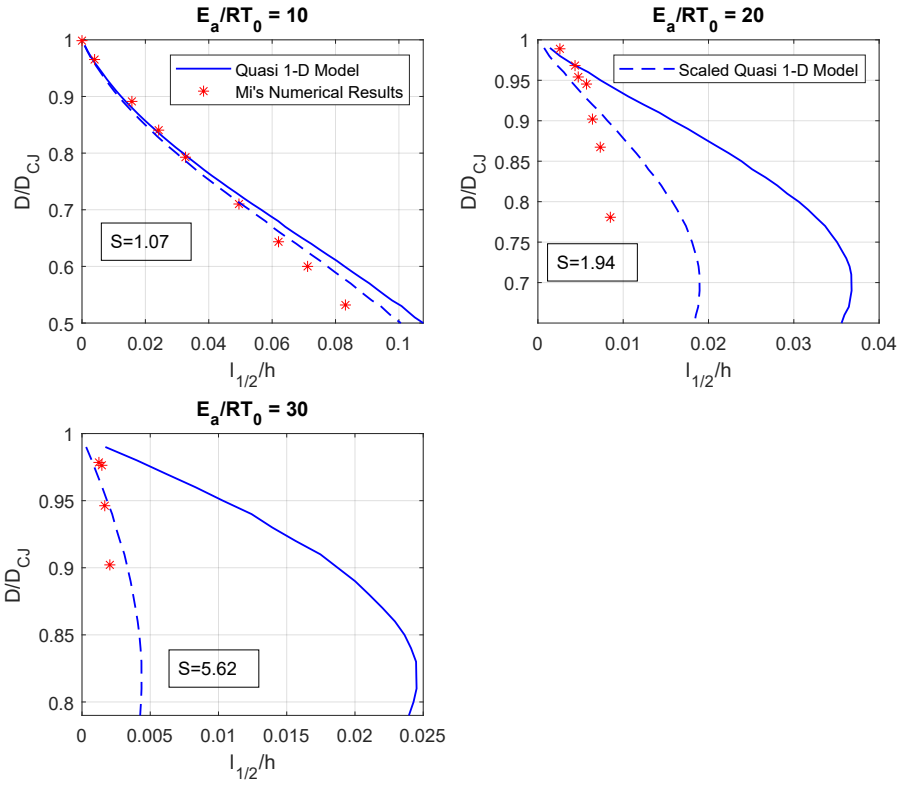

Figure 5.4: Scaling of the Quasi 1-D model for $Q/RT_0 = 50$, $\gamma = 1.2$, with Mi's results [24].

It is evident from Figures 5.1 - 5.4 that the reaction rate law needs to be drastically slowed down as the activation energy is increased due to the growing effect of cellular structure on detonation dynamics for higher activation energies. The quantitative analysis of the increase in scaling factor with an increase in activation energy is explained in subsection 5.3.1.

5.3 Kinetic Slow Down in Real Detonations

This section analyzes the global reaction zone lengthening as observed from the numerical simulations of Reynaud et al. [23]. The following graphs in Figure 5.5 correspond to results obtained by Reynaud [23]. As the reduced activation energy increases, the reaction zone gets thicker and thicker for different D/D_{CJ} values compared to the ZND-type Wood-Kirkwood (WK) model.

The typical decay of reactants on this graph (not to scale) is presented in Figure 5.6. Here $\widetilde{Y}$ is the Favre-averaged mass fraction on the central streamline for numerical computations. $x/l_{1/2}$ is the non-dimensionalized distance in the direction of propagation of detonation. Generally, it is observed that the evolution of reactants on this log-linear graph is linear, especially up till the majority of reactants are depleted. This reactant concentration profile can be represented by a straight line and is displayed in equation (5.3).

$$log(\widetilde{Y}) = m \cdot (x/l_{1/2}) + c \tag{5.3}$$

But as $x \to 0$, $log(\widetilde{Y}) \to 0$ and thus $c \approx 0$. The absolute equation of the line, which

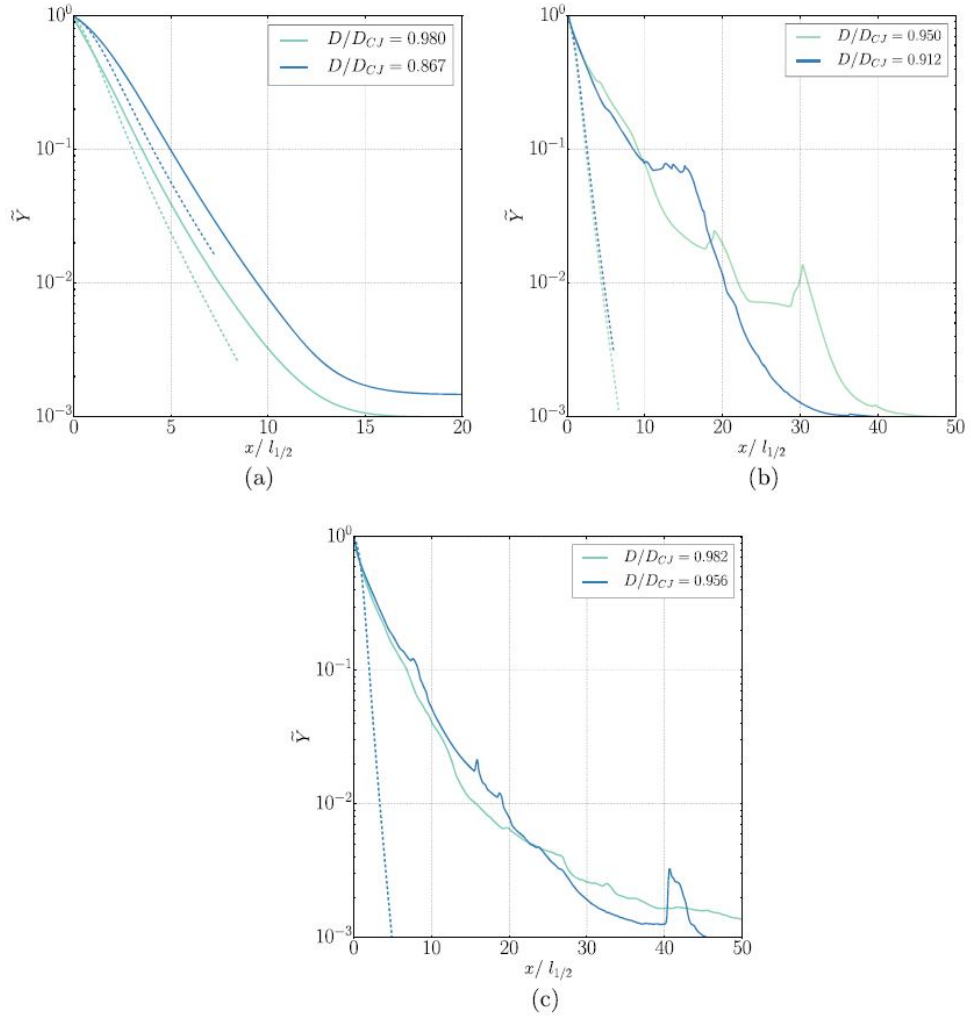

Figure 5.5: Average mass fraction profiles (solid lines) obtained for $E_a/RT_0 = 20$ (a), $E_a/RT_0 = 30$ (b), $E_a/RT_0 = 38.23$ (c). Comparison with WK model (broken lines). (From Reference [23]).

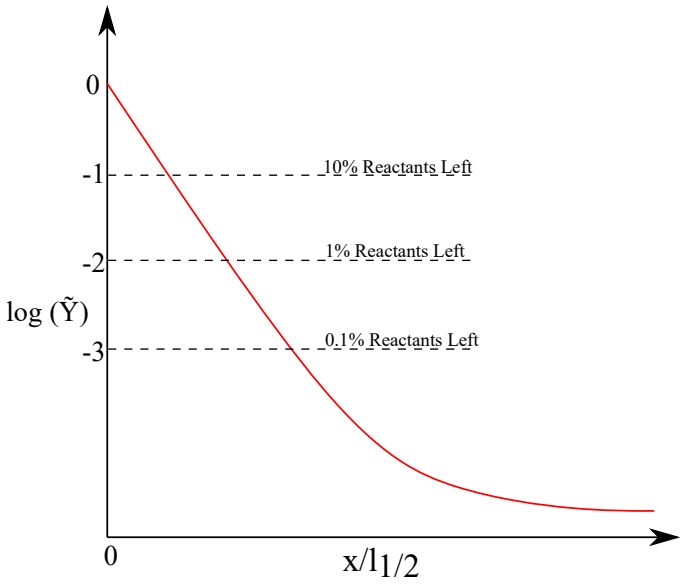

Figure 5.6: Schematic of depletion of reactants with respect to distance in direction of propagation of detonation (not to scale).

depicts the evolution of reactants, is now,

$$log(\widetilde{Y}) = m \cdot (x/l_{1/2}) \tag{5.4}$$

In order to calculate the reaction zone lengthening parameter, we have to evaluate x_{NS}/x_{WK}, where subscript NS correspond to numerical simulations and WK correspond to the Wood-Kirkwood model employed by Reynaud in his studies [23].

Thus, we can get the x_{NS}/x_{WK} expression upon simplification, as shown in equation (5.5).

$$\frac{x_{NS}}{x_{WK}} = \frac{m_{WK}}{m_{NS}} \tag{5.5}$$

The physical meaning of the term x_{NS}/x_{WK} is by how much factor the length of the reaction is scaled for numerical simulations as compared against the ZND-type Wood-Kirkwood model for the specified reactant concentration depletion value. This thickening is due to delayed energy deposition and cellular structure present in actual detonations. Here we take the ratio of the slope of lines on $log_{10}\widetilde{Y}\ \ vs\ \ x/l_{1/2}$. The effective kinetic slow-down experienced by the system, called G_1, can be calculated by equation (5.6).

$$G_1 = \frac{\sum_1^n \frac{m_{WK}}{m_{NS}}}{n} \tag{5.6}$$

Here, n total number of observation cases (different D/D_{CJ} values available) for given E_a/RT_0, m_{WK} is the slope of the straight line fitted to results of Wood-Kirkwood on '$log_{10}\widetilde{Y}\ \ vs\ \ x/l_{1/2}$' graph, and, similarly, m_{NS} is the slope of numerical computations. A snapshot from the [23] showing the reaction evolution is displayed here in Figure 5.5.

5.3.1 Results

The current analysis shows two different approaches to account for the reaction zone thickening due to the cellular structure of detonations. Here, we compare both approaches to check if they have any correlation. The correct way of quantifying scaling is to connect it with reduced activation energy non-dimensionalized by properties calculated at the von-Neumann state. This non-dimensionalization considers different heat-release energies, as T_{VN} is a function of Q and γ.

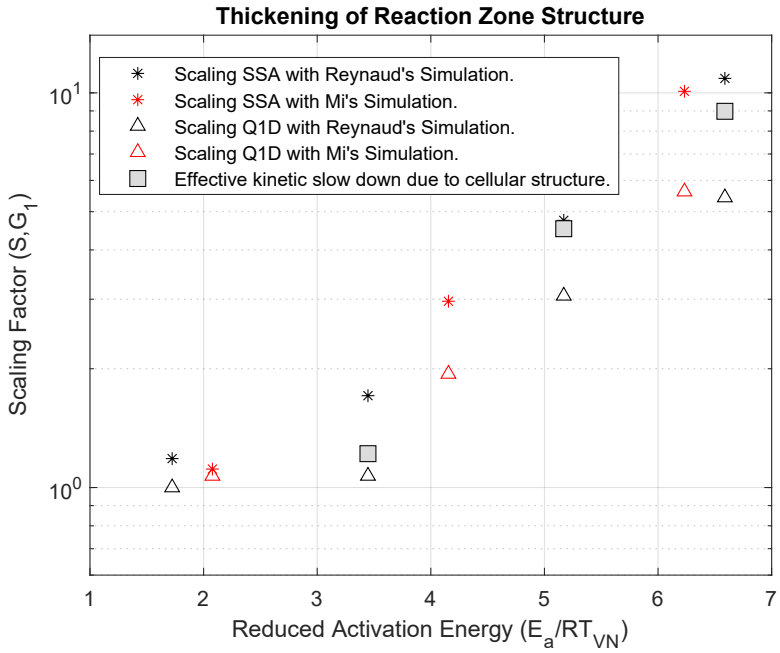

Figure 5.7: Scaling of the Quasi 1-D model, SSA model with numerical simulations.

Thus, the scaling parameters obtained from empirical fitting and effective lengthening of the reaction zone structure are plotted on '$Scaling\ vs\ E_a/RT_{VN}$'. The results are portrayed in Figure 5.7. Note that it is a 'semilog-y' graph, where values on Y-axis vary exponentially, not linearly.

The Figure shows that the Arrhenius 1-step chemistry employed in ZND-type analytical models has to be scaled exponentially as the instability of detonation increases. The decent correspondence between S_{SSM} & S_{Q1D} and G_1 (obtained from numerical simulations) strongly suggests that these ZND-type analytical models will continue to work well for unstable detonations, given that the correct rate law is employed. This exponential departure can be attributed to the unburnt pockets

of reactant present in irregular detonations which tend to burn at much slower rate.

5.4 Ignition Delay Model

5.4.1 Introduction

The results and analysis from section 5.3.1 suggest a significance of cellular structure on global energy deposition. A physical model to predict the delayed energy deposition arising due to slower burning of unburnt reactant pockets present in irregular cellular detonations is presented in this section.

The model starts by modelling the velocity fluctuations of the leading shock inside a detonation cell. It results in temperature variation behind the shock, as the shock's strength decays inside the cell. It is proposed that the reactants present in the later part of the cell burn at a much higher time than expected, as the ignition delay time of the reactants is exponentially proportional to the temperature. Thus, the cellular structure can be responsible for delayed energy deposition, which is not incorporated in 1-step Arrhenius kinetics.

5.4.2 Velocity Profile

The recent work by Cheevers and Radulescu [54], on the ignition mechanism behind decaying shock waves, has shown a linear decay of lead shock in a detonation cell with respect to spatial direction. Figure 5.8 shows the evolution of lead shock for different mixtures over the cell length as presented in [54]. It is clear from

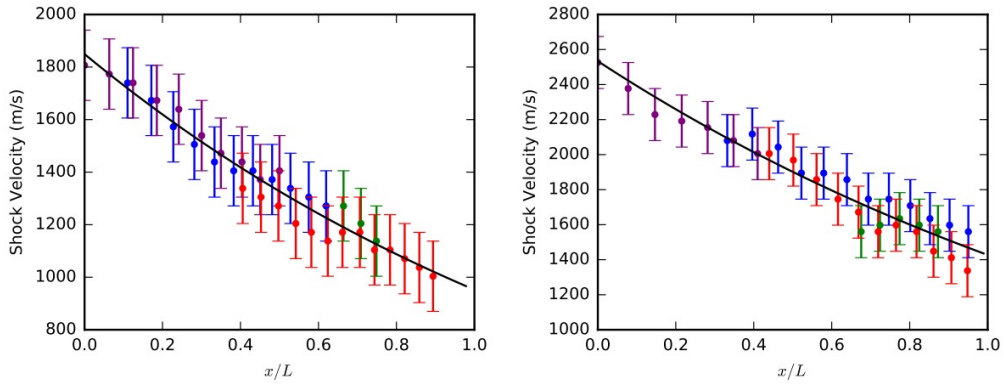

Figure 5.8: The shock speed evolution over a detonation cell, with the exponential curve-fit traced in black. For experiments a) 13_H2 and b) 0_CH4. The colour of each point represents their measurement series - blue : top wall, red : bottom wall, green : centreline pre-collision, purple : centreline post-collision (from Reference [54]).

figure 5.8 that lead shock has an overall trend of decaying linearly with distance inside a cell. Fickett and Davis [55] reviewed the literature available in 1979. The data collected indicate a sharp decrease in the lead shock speed at the early stages of the cell, which was followed by a generally linear decay with distance. The evolution of the velocity inside a cell, shown in Figure 5.9, is thus assumed to decay linearly in space and equivalently exponentially in time. The velocity gradient is constant, and the average velocity is the CJ-velocity.

Mathematically, the velocity profile looks like this,

$$\frac{dv}{dx} = C_1 \tag{5.7}$$

Here, equation (5.7) can be integrated to obtain the velocity profile as shown in

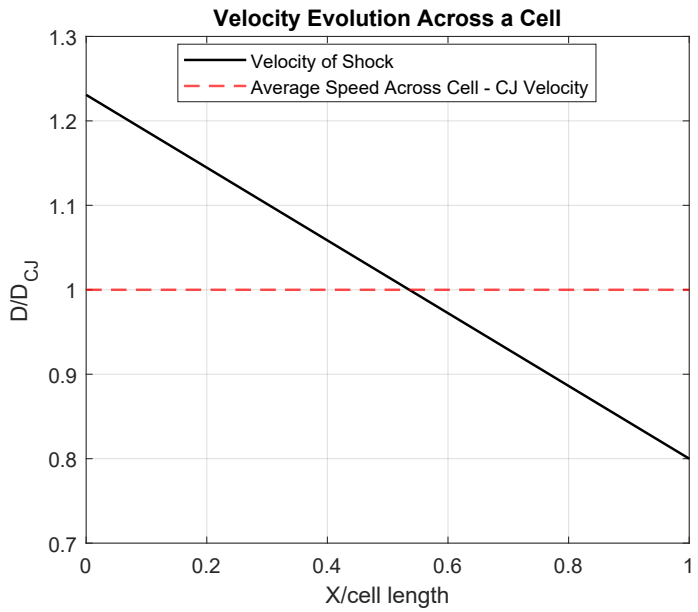

Figure 5.9: Schematic of a Velocity Profile inside a detonation cell.

equation (5.8). Here, v_i is the initial shock velocity at the cell's starting point and v_f is the velocity of decaying lead shock at the end of the cell, and x is the arbitrary distance in direction of cell length from the cell's starting point.

$$v = (v_f - v_i)x + v_i \tag{5.8}$$

The global average velocity of the lead shock, for the velocity profile as described in equation (5.8), is given by,

$$v_{avg} = \frac{v_f - v_i}{ln\left(\frac{v_f}{v_i}\right)} \tag{5.9}$$

Equation (5.9) shows the relationship between average detonation velocity v_{avg},

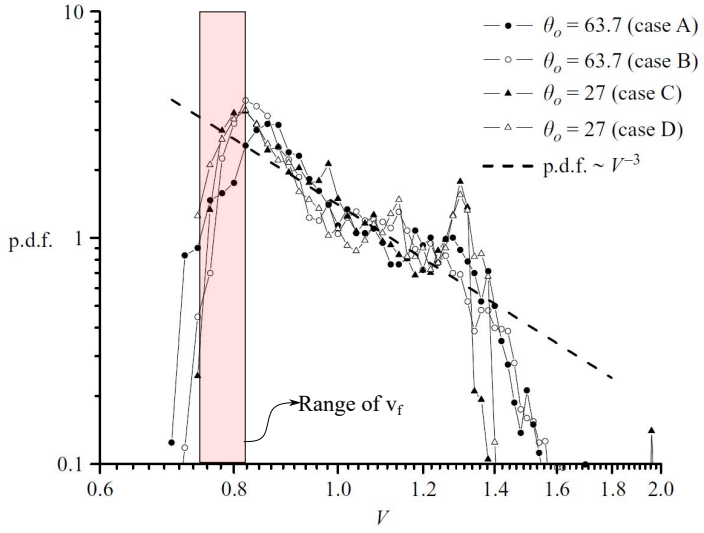

Figure 5.10: Probability density function of the leading shock velocity obtained from the shock velocity time series along the bottom wall for cases A, B, C, and D in [36]; broken line shows a power-law dependence with exponent - 3. (From Reference [36]).

the initial detonation velocity in the cell v_i, and final velocity v_f. If we can close any two variables with appropriate assumptions, the third variable takes value according to the equation. The first assumption is $v_{avg} = v_{CJ}$, the average detonation velocity in the cell, i.e., the global average steady velocity of detonation is CJ velocity. The second assumption is for the v_f, where the final velocity of the lead shock is $v_f = 0.80 \cdot v_{CJ}$. This value is arrived at after reviewing much literature [23, 36]. The sensitivity of the selection of v_f on the results is presented in Appendix B.1.

A snapshot of Figure from [36] shows that for different cases, $v_f \approx 0.75 - 0.85 \cdot D_{CJ}$, presented here as Figure 5.10.

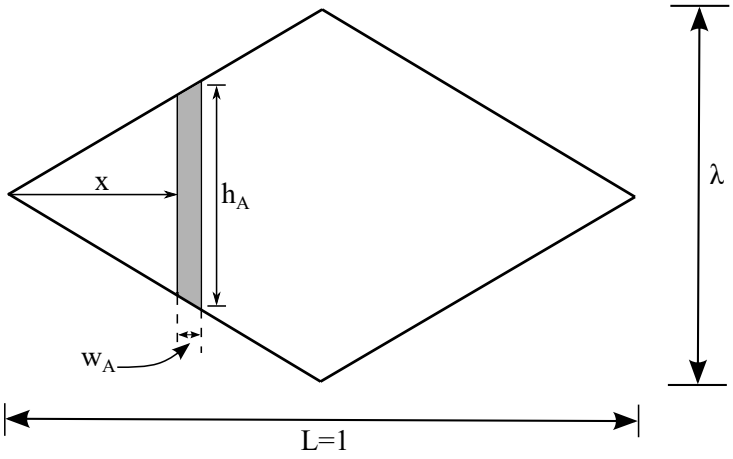

Figure 5.11: Schematic of a detonation cell.

5.4.3 Velocity Distribution

The next step is to evaluate the Probability Density Function (PDF) for velocity. It shows the fraction of reactive gases that have been shocked by the detonation front with velocity near to v, where v is the arbitrarily chosen velocity, mathematically represented by,

$$P(v \leq X < v + dv) = pdf(v) \cdot dv \tag{5.10}$$

We start by assuming a strip of reactive gas, as shown in Figure 5.11, at location x from the start of the cell, that has height h_a and width w_a. λ and L are cell-width and cell-length, respectively. Thus the h_a is given by equation (5.11). Note that the cell length is normalized, so $L = 1$.

$$h_a = 2\lambda x \tag{5.11}$$

The x is given by equation (5.8) and is represented here by,

$$x = \frac{v_i - v}{v_i - v_f} \tag{5.12}$$

After substituting equation (5.12) in (5.11), we get,

$$h_a = 2\lambda \left(\frac{v_i - v}{v_i - v_f} \right) \tag{5.13}$$

The width of the strip w_a is given by,

$$w_a = \mid x(v + dv) - x(v) \mid = \frac{dv}{v_i - v_f} \tag{5.14}$$

Thus, the total amount of reactants inside the strip, as displayed in Figure 5.11, is given by,

$$R = \rho_0 h_a w_a = 2\rho_0 \lambda \frac{(v_i - v)}{(v_i - v_f)^2} dv \tag{5.15}$$

The total amount of reactive gases present inside the detonation cell is given by the area of the cell, as shown mathematically,

$$R_t = \frac{\rho_0 \lambda}{2} \tag{5.16}$$

The fraction or probability of gases being shocked by the detonation front travelling at all velocities between v and $v + dv$ is given by,

$$P(v \leq X < v+dv) = \left(\frac{R}{R_t}\right) = \frac{4(v_i - v)}{(v_i - v_f)^2} \cdot dv \tag{5.17}$$

Thus, the PDF for all the velocities corresponding to the first half of the cell is given by equation (5.18). As the cell starts to shrink in size after $L = 0.5$, the probability density function will differ for the last half of the cell.

$$pdf_A(v) = \frac{4(v_i - v)}{(v_i - v_f)^2} \tag{5.18}$$

Similarly, the PDF for the last half of the cell can be derived and is presented here in equation (5.19). The subscript A and B on the pdf symbol indicate the cell's first and last half, respectively.

$$pdf_B(v) = \frac{4(v_f - v)}{(v_i - v_f)^2} \tag{5.19}$$

The entire probability distribution of velocities is displayed in Figure 5.12, where $v_f = 0.8 \cdot v_{CJ}$. A proper value for v_f is chosen from Figure 5.10. The v_i is obtained such that $v_{avg} = 1$, from equation (5.9). Note that velocity is normalized by v_{CJ}.

5.4.4 Ignition Delay Distribution

The next step is to evaluate the time taken by reactants to burn when the shock front of velocity v is passed through them. Thus ultimately deriving the probability density function of ignition delay time, the fraction of reactants burning after time t. The transformed distribution approach is employed to obtain the $pdf(t_{ig})$, as

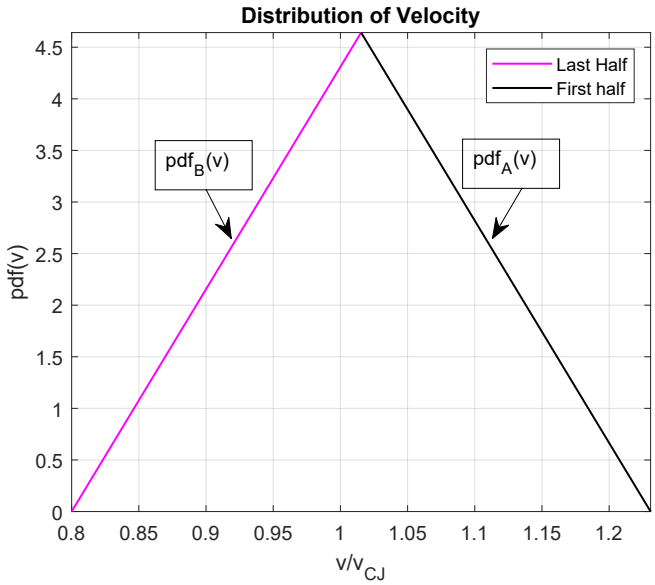

Figure 5.12: Probability density function of velocity for a detonation cell, where $v_f = 0.8\,v_{CJ}$.

shown in Figure 5.14. In this approach, if an expression between v and t_{ig} is known, the $pdf(v)$ can be transformed to $pdf(t_{ig})$. Note that the time taken by reactants to burn is the ignition delay time, t_{ig}, of the reactants.

It is known from various studies as present in the literature [56] that the t_{ig} of reactant materials is dependent on activation energy, E_a/RT_0, and temperature. This relation is shown here in equation (5.20). Here, T_{VN} is a function of v, the varying von-Neumann temperature faced by the reactants inside the cell, located just behind the shock.

$$t_{ig} = B \cdot exp\left[\frac{E_a}{RT_{VN}}\right] \tag{5.20}$$

Thus, ignition delay corresponding to CJ-detonation is,

$$t_{ig_{CJ}} = B \cdot exp\left[\frac{E_a}{RT_{VN_{CJ}}}\right] \tag{5.21}$$

Upon dividing equation (5.20) by (5.21), we get,

$$t_{ig} = t_{ig_{CJ}} \cdot exp\left[\frac{E_a}{RT_{VN_{CJ}}}\left(\frac{T_{VN_{CJ}}}{T_{VN}} - 1\right)\right] \tag{5.22}$$

In order to determine the shocked state, a strong shock approximation is employed for simplicity. The pressure p_{VN} and density ρ_{VN} are given by equations (5.23) and (5.24), respectively.

$$p_{VN} = \frac{2}{\gamma+1}\rho_0 v^2 \tag{5.23}$$

$$\rho_{VN} = \frac{\gamma+1}{\gamma-1}\rho_0 \tag{5.24}$$

The temperature at the shocked state is obtained from the Ideal gas law. It is given by,

$$T_{VN} = \frac{p_{VN}}{R\rho_{VN}} = \frac{2(\gamma-1)}{(\gamma+1)^2} v^2 \tag{5.25}$$

$$T_{VN_{CJ}} = \frac{p_{VN_{CJ}}}{R\rho_{VN_{CJ}}} = \frac{2(\gamma-1)}{(\gamma+1)^2} v_{CJ}^2 \tag{5.26}$$

Upon substituting equation (5.26) into equation (5.22), we get the relationship

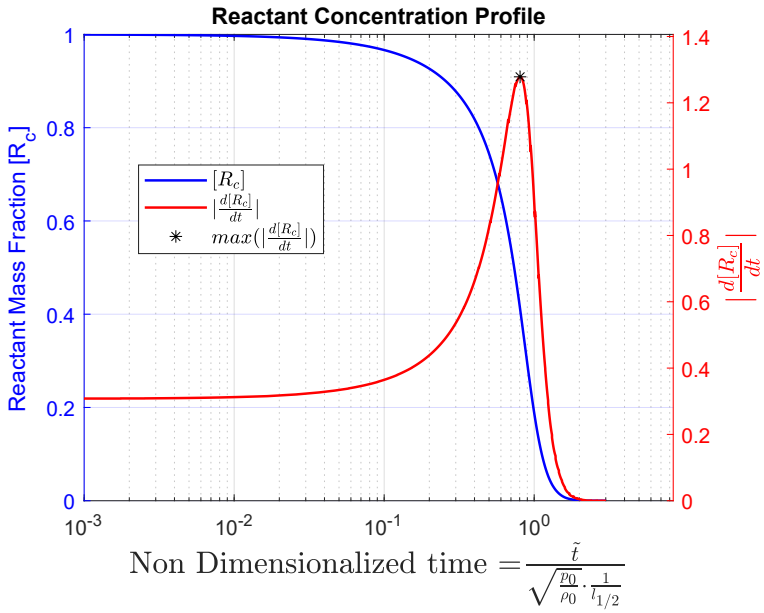

Figure 5.13: Reactant concentration profile of ZND detonation for $Q/RT_0 = 23.81$, $\gamma = 1.333$ and $E_a/RT_0 = 10$.

between t_{ig} and v. It is denoted in equation (5.27). The inverse of activation energy, non-dimensionalized by the shocked-state, is denoted here as ε. As the system is non-dimensionalized by CJ velocity, therefore $v_{CJ} = 1$.

$$t_{ig} = t_{ig_{CJ}} \cdot exp\left[\frac{1}{\varepsilon}\left(\frac{1}{v^2} - 1\right)\right] \tag{5.27}$$

Here, $t_{ig_{CJ}}$ is chosen as the time at which the maximum reactants are burning for the ZND solution with no loss case, for defined reduced activation energy E_a/RT_{VN}, for Arrhenius 1-step chemistry. Figure 5.13 shows the evolution of reactants for $Q = 23.81$, $\gamma = 1.333$ and $E_a/RT_0 = 10$ for the ZND detonation. These values correspond to $E_a/RT_{VN} = 1.7233$.

The summary of $t_{ig_{CJ}}$ for all the cases [23, 24] is given in table 5.1. Note that ignition delay time is non-dimensionalized by the initial pressure, density and half-reaction zone length.

Q/RT_0	γ	E_a/RT_0	$E_a/RT_{VN_{CJ}}$	$t_{ig_{CJ}}$
23.81	1.333	10	1.7233	0.22125
23.81	1.333	20	3.4468	0.56895
23.81	1.333	30	5.1706	0.72515
23.81	1.333	38.23	6.5891	0.81178
50	1.2	10	2.0775	0.53829
50	1.2	20	4.155	0.85989
50	1.2	30	6.2325	1.03599

Table 5.1: Ignition delay time of the CJ detonation for all the cases as obtained at peak reactant concentration change for ZND solution.

The probability density function of ignition time is given by equation (5.28). As t_{ig} increases upon decreasing v, the modulus operator in the equation is removed by adding a $-ve$ sign in the expression. The definition of the probability density function of t_{ig} is obtained from the transformed distribution approach. Here $pdf_t(x)$ is the PDF corresponding to ignition delay time t_{ig}, and $pdf_v(x)$ is PDF linked to velocity v.

$$pdf_t(t_{ig}) = pdf_v(v(t_{ig})) \mid \frac{dv}{dt_{ig}} \mid \tag{5.28}$$

In order to solve for $pdf_t(t_{ig})$, we have to evaluate two expressions, $v(t_{ig})$ and $\mid \frac{dv}{dt_{ig}} \mid$. Here, pdf_t and pdf_v, correspond to the distribution of ignition delay times and velocity of shock experienced by reactants inside the cell, respectively.

Upon rearranging equation (5.27), velocity as a function of ignition delay, $v(t_{ig})$, is given by,

$$v(t_{ig}) = \left(\varepsilon \, ln \left(\frac{t_{ig}}{t_{ig_{CJ}}} \right) + 1 \right)^{-\frac{1}{2}} \tag{5.29}$$

The term $\mid \frac{dv}{dt_{ig}} \mid$ can be obtained by taking the derivative of equation (5.27) and rearranging it. The final expression is shown in equation (5.30). Note that the $-ve$ is taken care of while opening the modulus operator.

$$\mid \frac{dv}{dt_{ig}} \mid = \frac{\varepsilon}{2t_{ig}} \left(\varepsilon \, ln \left(\frac{t_{ig}}{t_{ig_{CJ}}} \right) + 1 \right)^{-\frac{3}{2}} \tag{5.30}$$

Upon substituting equations (5.29) and (5.30) into equation (5.28), we get the expression for $pdf_t(t_{ig})$, where $pdf_v(x)$ is the probability density function for velocity. It is shown in equation (5.31).

$$pdf_t(t_{ig}) = pdf_v \left[\left(\varepsilon \, ln \left(\frac{t_{ig}}{t_{ig_{CJ}}} \right) + 1 \right)^{-\frac{1}{2}} \right] \cdot \frac{\varepsilon}{2t_{ig}} \left(\varepsilon \, ln \left(\frac{t_{ig}}{t_{ig_{CJ}}} \right) + 1 \right)^{-\frac{3}{2}} \tag{5.31}$$

Figure 5.14 shows the transformation of the probability density function of velocity to the probability density function of ignition delay time. The latter part of the curve in $pdf(t_{ig})$ corresponds to the first part of the curve in $pdf(v)$ and vice versa.

Upon substituting the definition of $pdf(v)$ in equation (5.31) and rearranging it, The $pdf_A(t_{ig})$, corresponding to the first half of the cell, is given by equation

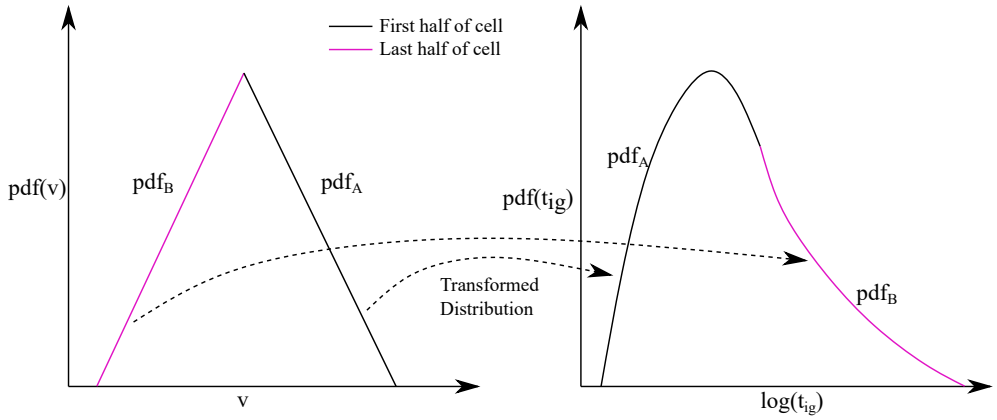

Figure 5.14: Schematic of transformed distribution approach.

(5.32).

$$pdf_A(t_{ig}) = \frac{4}{(v_i - v_f)^2}\left[\frac{\varepsilon}{2t_{ig}}\left(\varepsilon ln\left(\frac{t_{ig}}{t_{ig_{CJ}}}+1\right)\right)^{-2}\right] - \frac{4}{(v_i - v_f)^2}\left[\frac{v_i\varepsilon}{2t_{ig}}\left(\varepsilon ln\left(\frac{t_{ig}}{t_{ig_{CJ}}}+1\right)\right)^{-\frac{3}{2}}\right] \tag{5.32}$$

Similarly, the probability density function for ignition delay time corresponding to the last half of the cell is given by equation (5.33). The PDF of ignition delay time for the case where $Q/RT_0 = 23.81$, $E_a/RT_0 = 30$, $\gamma = 1.333$ and $v_f = 0.8\,v_{CJ}$ is shown in Figure 5.15.

$$pdf_B(t_{ig}) = \frac{4}{(v_i - v_f)^2}\left[\frac{\varepsilon}{2t_{ig}}\left(\varepsilon ln\left(\frac{t_{ig}}{t_{ig_{CJ}}}+1\right)\right)^{-2}\right] - \frac{4}{(v_i - v_f)^2}\left[\frac{v_f\varepsilon}{2t_{ig}}\left(\varepsilon ln\left(\frac{t_{ig}}{t_{ig_{CJ}}}+1\right)\right)^{-\frac{3}{2}}\right] \tag{5.33}$$

If we obtain the Cumulative Density Function (CDF) of the $pdf(t_{ig})$ and map it

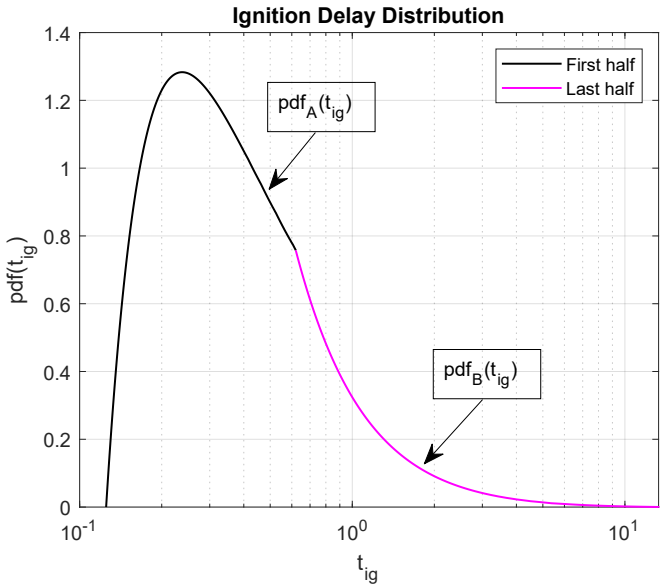

Figure 5.15: Probability density function of ignition delay time for a detonation cell, where $Q/RT_0 = 23.81$, $E_a/RT_0 = 30$, $\gamma = 1.333$ and $v_f = 0.8\,v_{CJ}$.

with ignition delay time, we can know what fraction of reactants are burned to products after how much time. Extrapolating this fact to all the cells for a steady solution will give the evolution of the global average reaction progress variable. The CDF for ignition delay time for the first and last half of the cell is given by equations (5.34) and (5.35), respectively. Here $t_{ig,i}$, $t_{ig,m}$ and $t_{ig,f}$ are the ignition delay times evaluated at v_i,$(v_i + v_f)/2$ and v_f, respectively.

$$cdf_A(t_{ig}) = \int_{t_{ig,i}}^{t} pdf_A(t_{ig})d(t_{ig}) \tag{5.34}$$

$$\begin{aligned} cdf_B(t_{ig}) &= \int_{t_{ig,i}}^{t_{ig,m}} pdf_A(t_{ig})d(t_{ig}) + \int_{t_{ig,m}}^{t} pdf_B(t_{ig})d(t_{ig}) \\ &= 0.5 + \int_{t_{ig,m}}^{t} pdf_A(t_{ig}) \end{aligned} \tag{5.35}$$

After solving equations (5.34) and (5.35), the expression for the CDF for ignition delay time is presented in equations (5.36) and (5.37), respectively. Here $v_m = (v_i + v_f)/2$, the velocity of the shock at the center of the cell.

$$\begin{aligned} cdf_A(t_{ig}) = \frac{2v_i^2}{(v_i - v_f)^2} &- \frac{4v_i}{(v_i - v_f)^2}\left(\varepsilon\, ln\left(\frac{t_{ig}}{t_{ig_{CJ}}}\right) + 1\right)^{-1/2} \\ &+ \frac{2}{(v_i - v_f)^2}\left(\varepsilon\, ln\left(\frac{t_{ig}}{t_{ig_{CJ}}}\right) + 1\right)^{-1} \end{aligned} \tag{5.36}$$

$$\begin{aligned} cdf_B(t_{ig}) = 0.5 &- \frac{2v_f v_m}{(v_i - v_f)^2} + \frac{4v_f}{(v_i - v_f)^2}\left(\varepsilon\, ln\left(\frac{t_{ig}}{t_{ig_{CJ}}}\right) + 1\right)^{-1/2} \\ &- \frac{2}{(v_i - v_f)^2}\left(\varepsilon\, ln\left(\frac{t_{ig}}{t_{ig_{CJ}}}\right) + 1\right)^{-1} + \frac{2v_m^2}{(v_i - v_f)^2} \end{aligned} \tag{5.37}$$

The CDF for ignition delay shows the total fraction of reactants burned as a function of time, also called the reaction progress variable. Thus, the '$1 - cdf(t_{ig})$' expression represents how much fraction of reactant concentration is left to be consumed as a function of time. Figure 5.16 shows this evolution of reactants with time for $Q/RT_0 = 23.81$, $E_a/RT_0 = 30$, $\gamma = 1.333$ and $v_f = 0.8\, v_{CJ}$.

This energy release profile is compared against ZND solution with 1-step Arrhenius kinetics. The relevant lengthening of time scales for a given reaction progress variable is evaluated to evaluate the effect of delayed burning of reactants evident

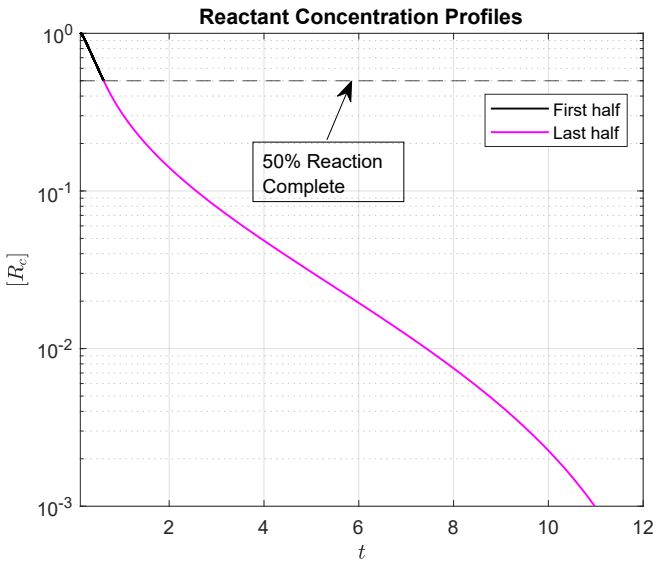

Figure 5.16: Evolution of reactant concentration as obtained from IGD model for $Q/RT_0 = 23.81$, $E_a/RT_0 = 30$, $\gamma = 1.333$ and $v_f = 0.8\,v_{CJ}$.

in unstable detonations.

5.4.5 Results

The Ignition Delay Model predicts the global average rate at which reactants are burning in a steady cellular detonation. This reactant profile is compared against the ZND structure of detonation, having no losses. The Figure 5.17 correspond to reactant concentration profiles for Ignition Delay Model and ZND solution for the case where $Q/RT_0 = 23.81$, $\gamma = 1.333$, $Ea/RT_0 = 30$ and $v_f = 0.8 \cdot D_{CJ}$.
To quantify the reaction zone lengthening, an assumption on the reaction completion must be made. For instance, an assumption that reaction is complete when 1% of reactants are left is considered for the abovementioned case. The scaling

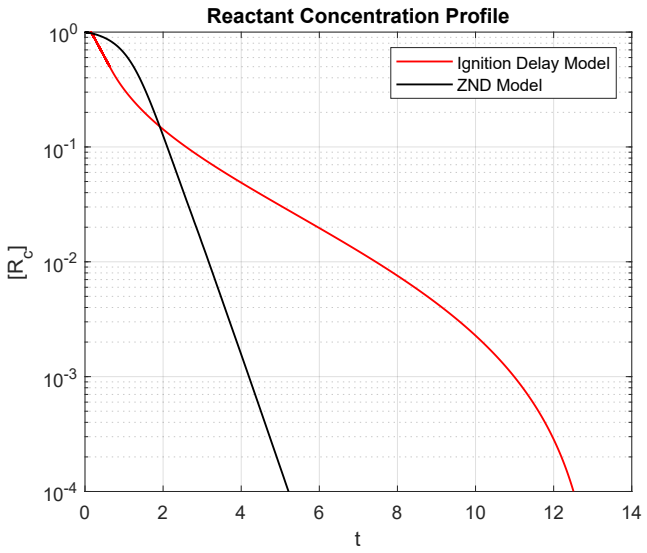

Figure 5.17: Reactant concentration profile for Ignition delay model (in red), for $v_f = 0.8\,v_{cj}$, and ZND solution (in black), for $E_a/RT_0 = 30$, $Q/RT_0 = 23.81$ and $\gamma = 1.333$.

parameter thus obtained is given by equation (5.38). The numerator and denominator correspond to the time t when 1% of reactants are left for the IGD and ZND model, respectively. $[R_c]$ is the mass fraction of reactants left to burn.

$$S_{IGD} = \frac{t\ @\ ([R_c] = 0.01)_{IGD}}{t\ @\ ([R_c] = 0.01)_{ZND}} \tag{5.38}$$

Figure 5.18 displays the variation in S_{IGD} for different activation energies E_a/RT_{VN}, when $v_f = 0.8 \cdot D_{CJ}$. The sensitivity of this graph on v_f and $[R_c]$ is presented in appendix B.1. Interestingly, the IGD model underpredicts the scaling, characterized by $S_{IGD} < 1$, for cases where $E_a/RT_{VN} < 4$. This underperformance arises because reactants deplete faster than expected compared to the ZND solution. This

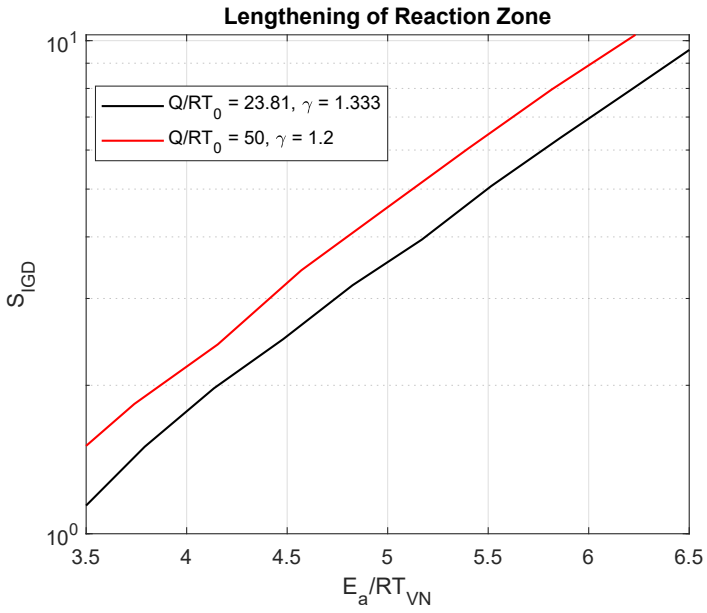

Figure 5.18: Scaling of reaction-zone structure as obtained from Ignition delay model for $v_f = 0.8\,v_{CJ}$.

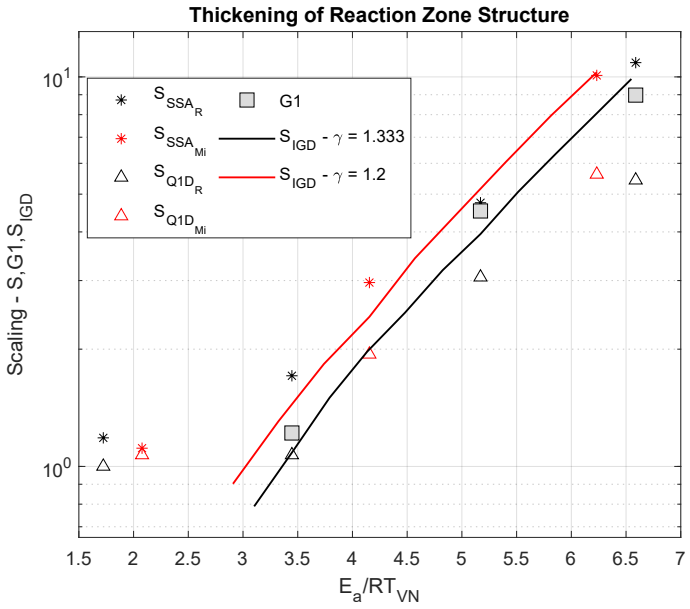

Figure 5.19: Scaling of reaction-zone structure as obtained from different models.

faster burning of reactants is due to the high von-Neuman temperature faced by reactants under strong-shock conditions.

The relevant comparison of effective kinetic slow-down due to lengthening of reaction zone as obtained via numerical simulations is compared against the results of the IGD model in Figure 5.19. The very good agreement of the two independently derived scaling factors shows that the cellular structure can be modelled accurately by first principles to account for the lengthening of the reaction zone in gaseous detonations.

The important aspect to note here is that the ignition delay model does not incorporate the effect of transverse waves on the burning rates of reactants. For stable detonations, characterized by low activation energies, the regular cellular structure can be treated as a collection of ”laminar detonation wavelets”, thereby allowing the ZND-type models to aptly capture the reaction zone structure. For, irregular mixtures the transverse waves are not strong enough to have a significant effect on the burning rates of reactants [57]. Thus, the ignition delay model is able to predict the global burning rate for irregular cellular detonation. The quantitative effect of transverse waves on unburnt reactants for varying regularity of mixtures is left for future study.

Chapter 6

Summary and Conclusions

6.1 Summary

The present study addresses the problem of predicting the nature of weakly confined gaseous detonations by analytical models. It is illustrated that two analytical models, Straight Streamline Approximation model and Quasi 1-D model, possess excellent predictability characteristics for the case where detonations are stable. However, these models underpredict the length of the reaction zone for unstable detonations. Compared to numerical calculations, the degree of departure of these models increases exponentially as the reduced activation energy is increased. The cellular structure of such detonations explains this disagreement. It slows down the global rate of reactant depletion, primarily due to long ignition delay times faced by reactants present in the latter half of the cell. As shown in Figure 6.1, the agreement between different scaling parameters suggests that

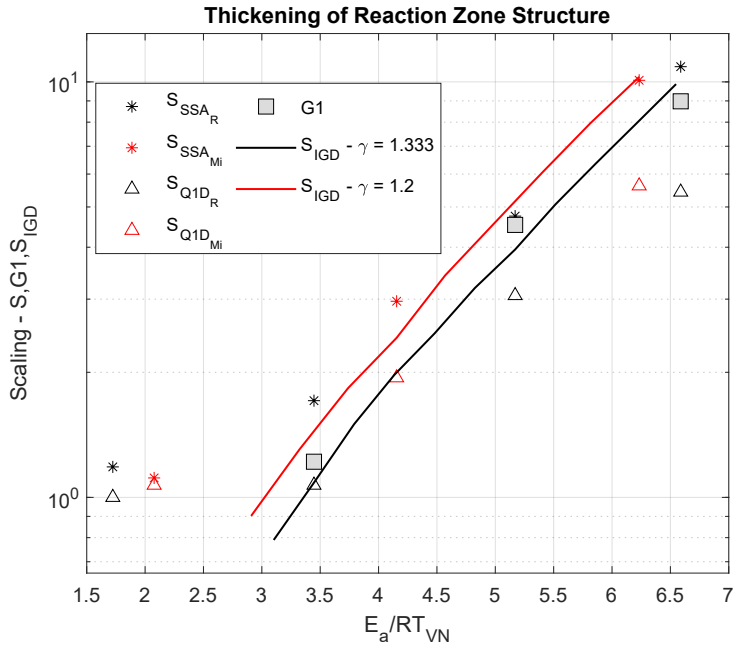

Figure 6.1: Scaling of reaction-zone structure as obtained from different models.

these analytical models would continue to work well in predicting the detonation response if the effective kinetic slow-down due to the cellular structure was modelled correctly. The two regimes of stability are discovered that are demarcated by $E_a/RT_{VN} \approx 3.5$. It is shown that these models can predict the dynamics of detonations corresponding to $E_a/RT_{VN} < 3.5$. The non-ideal detonations characterized by $E_a/RT_{VN} > 3.5$ can be modelled via these models if the influence of cellular structure on detonation's global reaction zone structure is quantified.

6.2 Conclusions

Finally, our investigation indicated that the SSA and Q1D models could predict the trends of Diameter-effect curves for detonations with $E_a/RT_{VN} < 3.5$, compared to numerical simulations. These models starts to disagree with the numerical simulations as the activation energy is increased. The disagreement increases exponentially as the E_a/RT_{VN} is increased, with a maximum error of about 1000% for $E_a/RT_{VN} \approx 6.5$. However, the error comes from the fact that these simple models do not consider the cellular structure that significantly influences the reaction zone of such detonations. If the influence of cellular structure is modelled appropriately, these analytical models will continue to predict the velocities of weakly confined detonations correctly.

6.3 Future Prospects

The present study adopted a single-step Arrhenius for simplicity and compared analytical models with the high fidelity simulations with the same rate law. Nevertheless, the SSA model can be extended to more complex kinetics and thermochemical properties in a straightforward way. The loss term in the Quasi 1-D model can be closed in multiple ways to justify the lateral flow divergence experienced in such detonations. The assumption of a straight streamline can also be relaxed, albeit at the expense of further complexity. Recently a "Variational Streamline Approach" model has been proposed [58]. More importantly, however, the model for the reaction zone lengthening in detonation waves, where

diffusion effects in real mixtures may play an important role in burning out the pockets [36, 5].

There are very few experiments available in the literature that captures the overall dynamics of gaseous detonations bounded by an inert layer. The scarcity in data is mainly for cases where acoustic impedance ratio, $Z \neq 1$, observed in Rotating Detonation Engine (RDE) where inert confiner is at elevated temperatures as they are combustion products. Thus, a proper qualitative and quantitative analysis from experiments of such detonation will add much-needed results to the detonation theory. Detailed numerical simulations of this configuration with complete chemistry will help understand the problem more deeply and analyze discontinuities observed due to detonation instabilities, irregular cells, and delayed burning of reactant pockets via diffusion.

Appendix A

Detonation Structure - SSA Model

A.1 $Q = 23.81$ and $\gamma = 1.333$

This section is dedicated to show the detonation structure comprising of shock front and sonic locus for all the cases as discussed in Reynaud's numerical simulation [23].

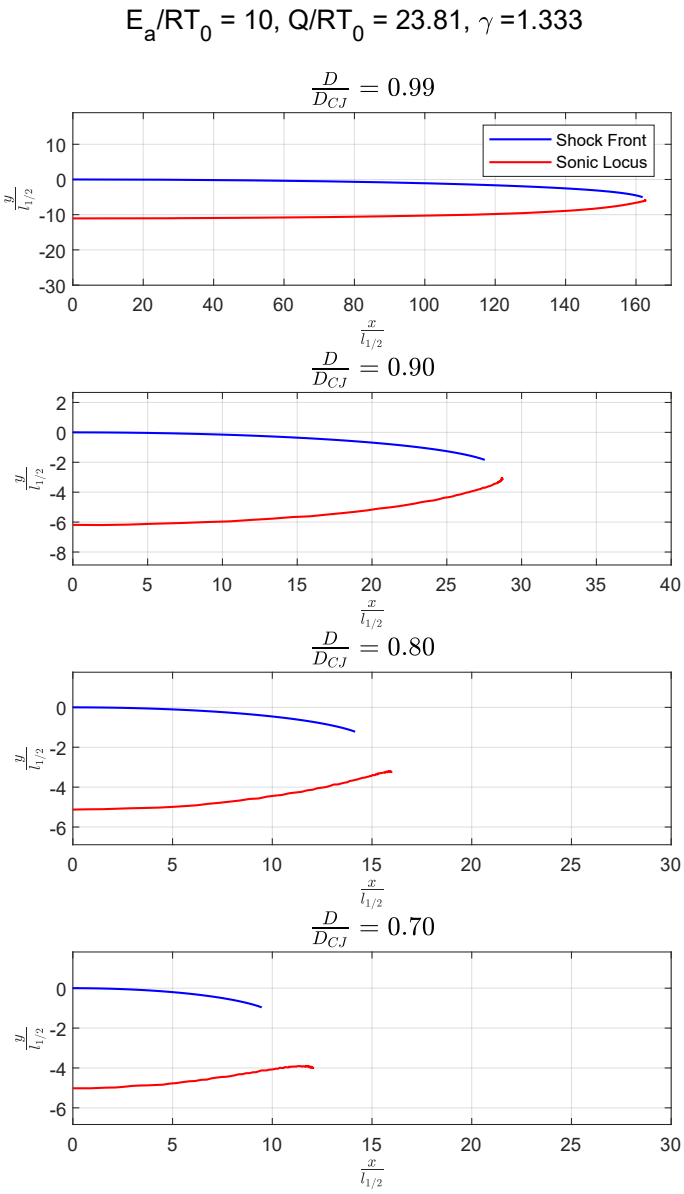

Figure A.1: Shock Front structure for different D/D_{CJ} at given $E_a/RT_0 = 10$, $Q/RT_0 = 23.81$ and $\gamma = 1.333$.

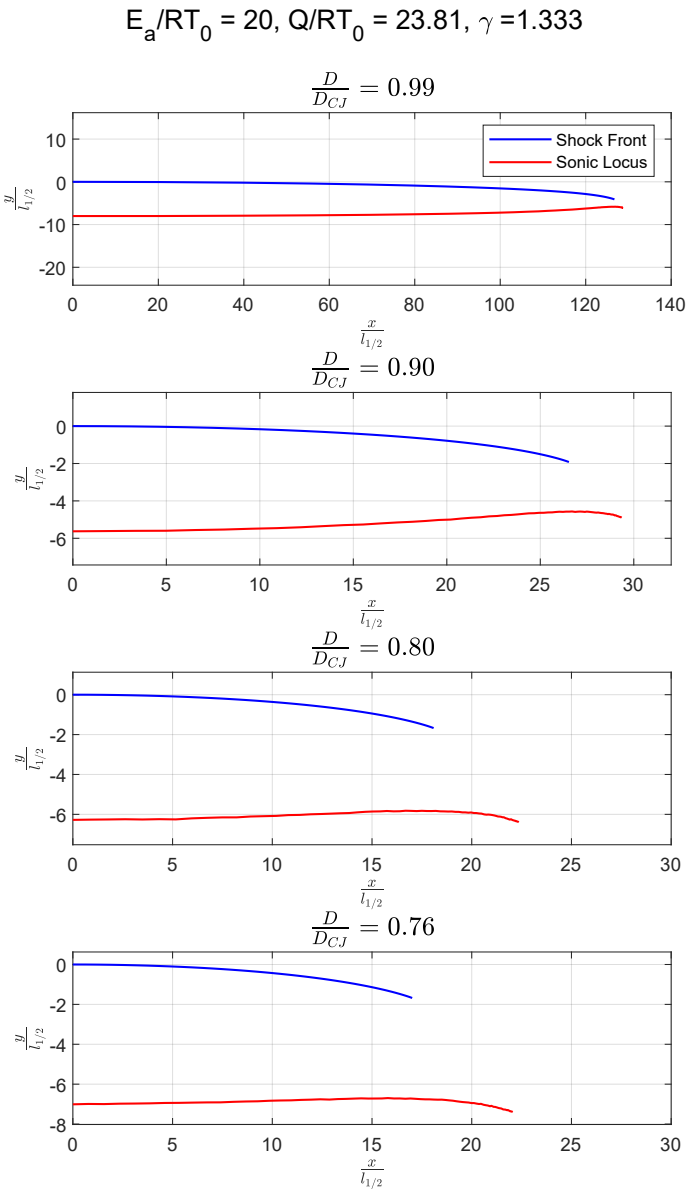

Figure A.2: Shock Front structure for different D/D_{CJ} at given $E_a/RT_0 = 20$, $Q/RT_0 = 23.81$ and $\gamma = 1.333$.

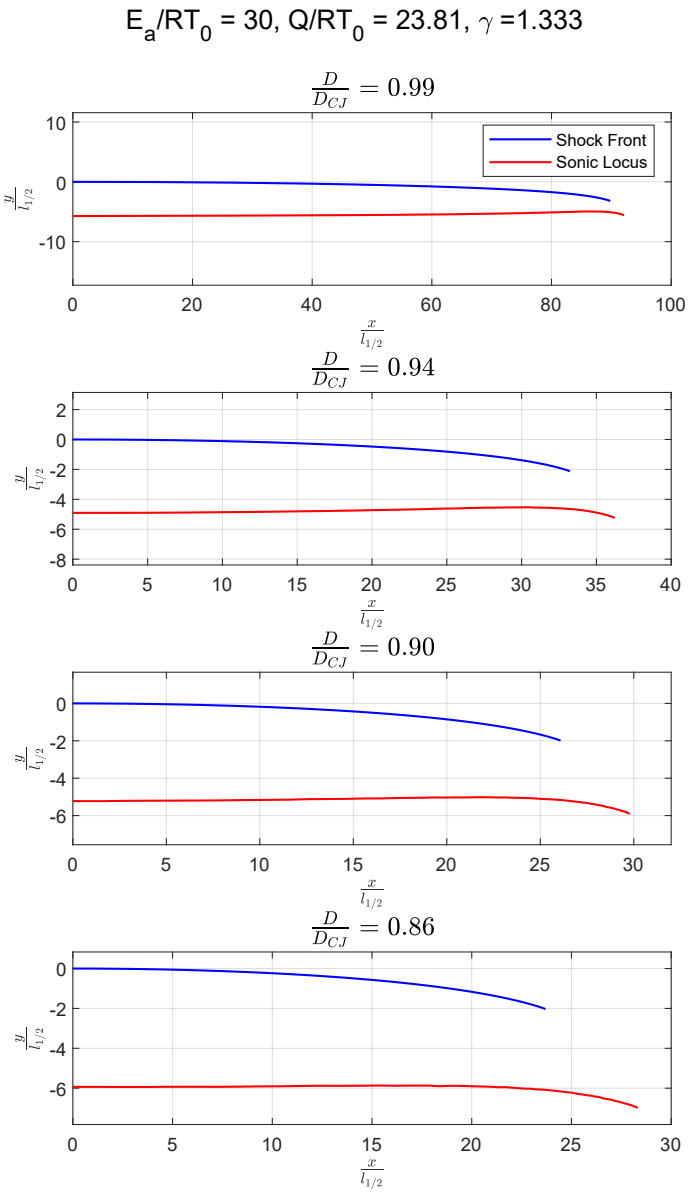

Figure A.3: Shock Front structure for different D/D_{CJ} at given $E_a/RT_0 = 30$, $Q/RT_0 = 23.81$ and $\gamma = 1.333$.

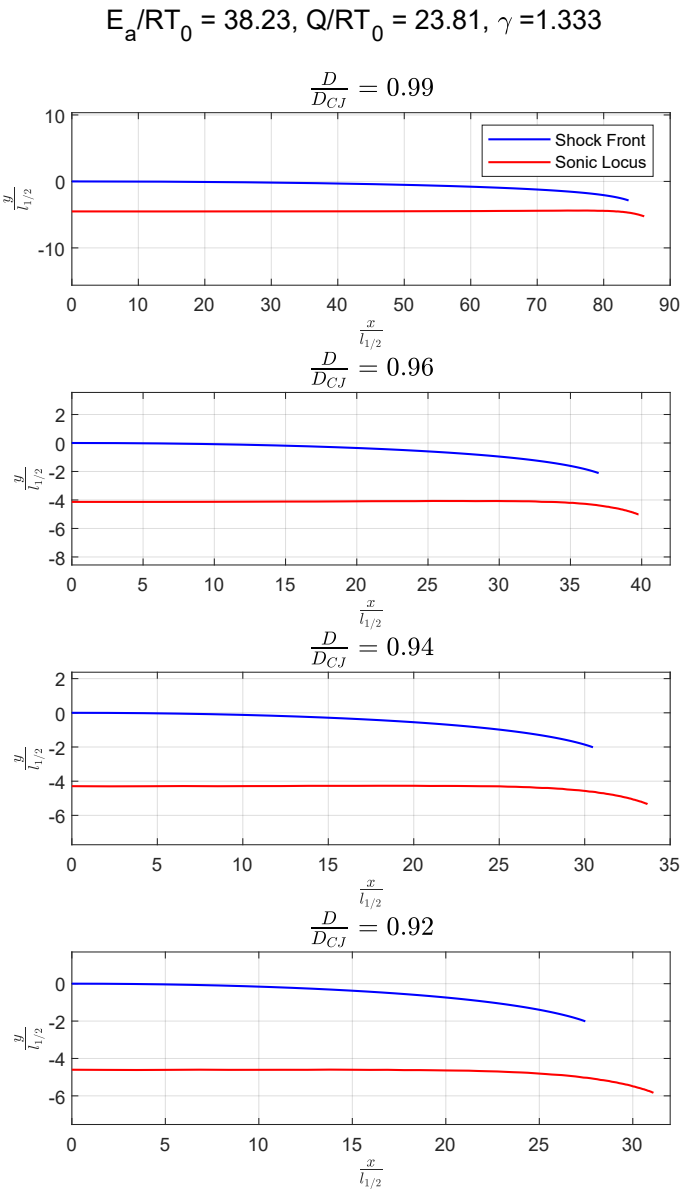

Figure A.4: Shock Front structure for different D/D_{CJ} at given $E_a/RT_0 = 38.23$, $Q/RT_0 = 23.81$ and $\gamma = 1.333$.

A.2 $Q = 50$ and $\gamma = 1.2$

This section is dedicated to show the detonation structure comprising of shock front and sonic locus for all the cases as discussed in Mi's numerical simulation [24].

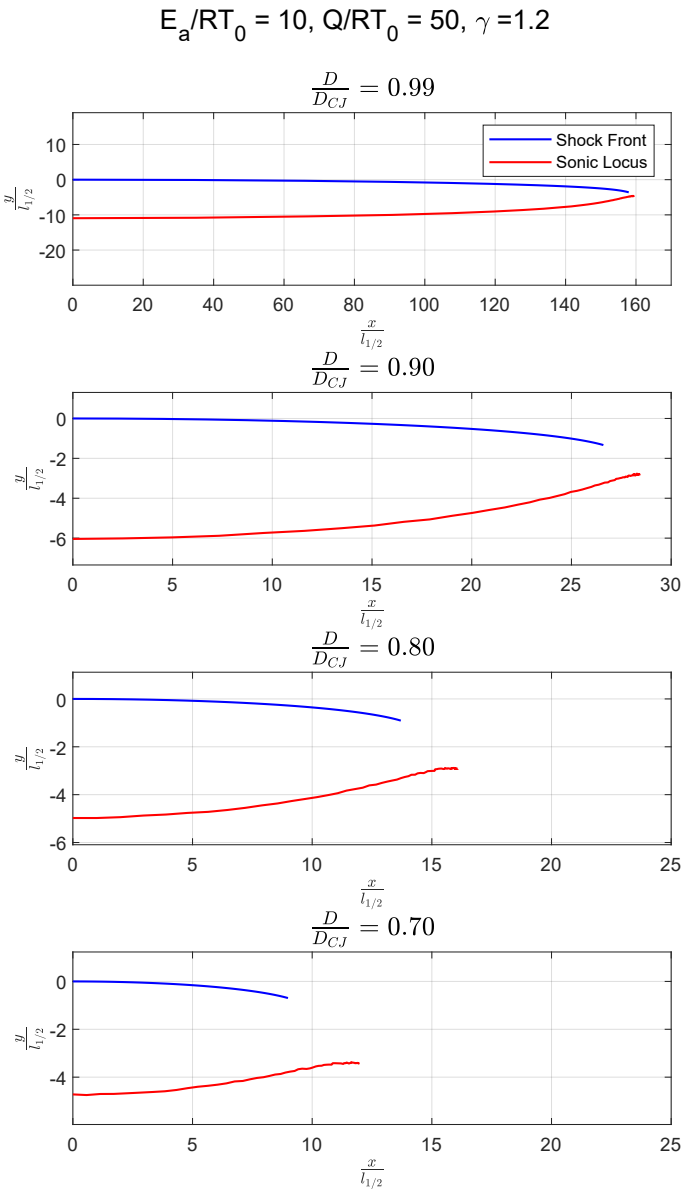

Figure A.5: Shock Front structure for different D/D_{CJ} at given $E_a/RT_0 = 10$, $Q/RT_0 = 50$ and $\gamma = 1.2$.

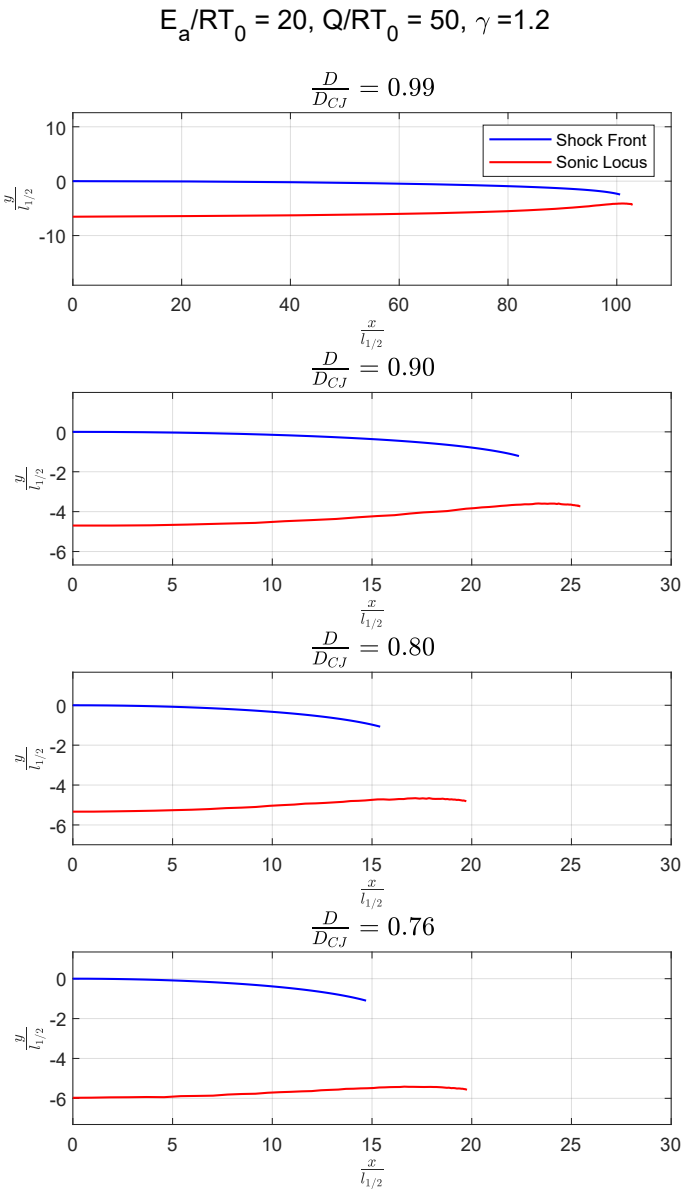

Figure A.6: Shock Front structure for different D/D_{CJ} at given $E_a/RT_0 = 20$, $Q/RT_0 = 50$ and $\gamma = 1.2$.

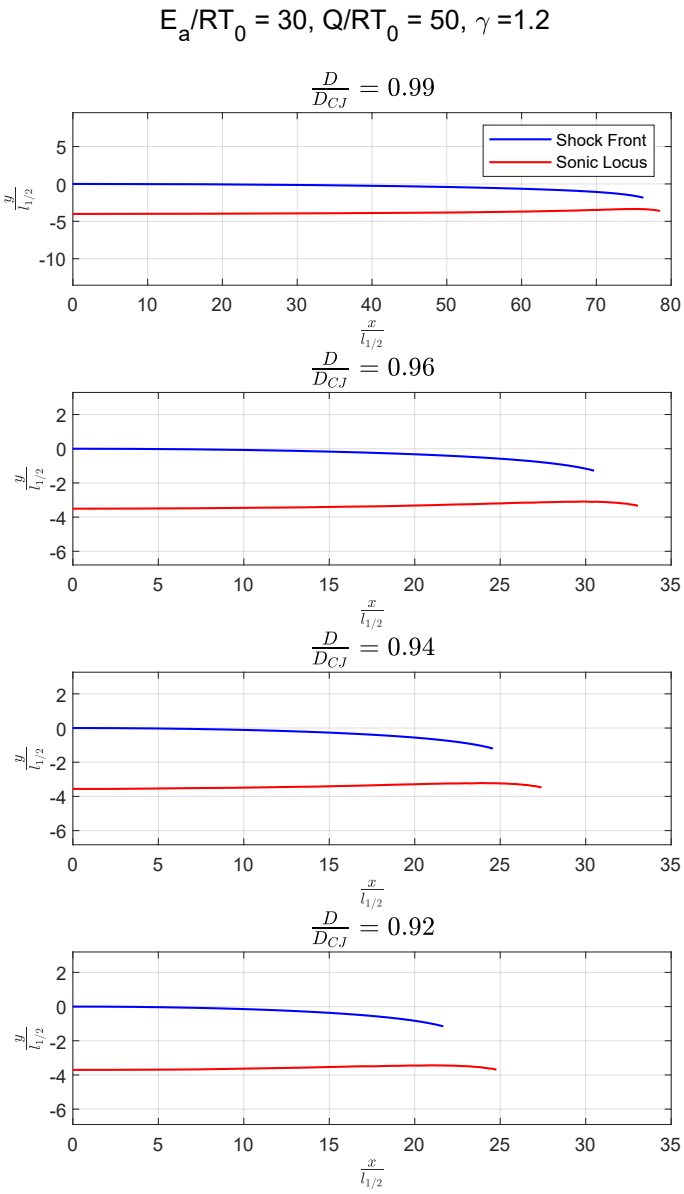

Figure A.7: Shock Front structure for different D/D_{CJ} at given $E_a/RT_0 = 30$, $Q/RT_0 = 50$ and $\gamma = 1.2$.

Appendix B

Ignition Delay Model Results

This Chapter is dedicated for detailed results obtained from Ignition Delay Model.

B.1 Sensitivity Analysis

This section shows the sensitivity of the ignition delay model's scaling parameter in comparision to varying final velocity inside the cell.

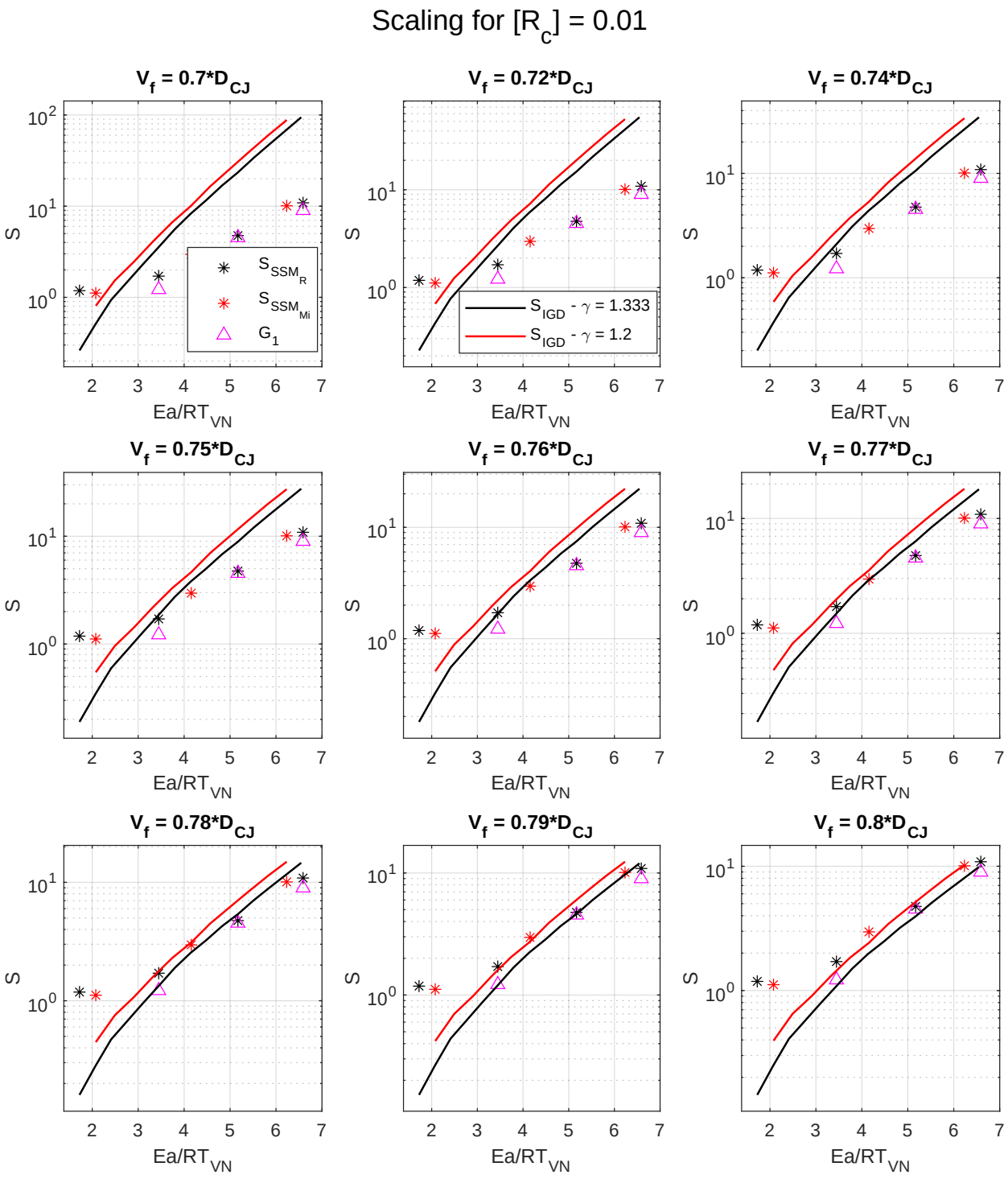

Figure B.1: Scaling of Reaction Zone Length for Ignition Delay Model on the assumption of reaction is complete at 1% of reactants.

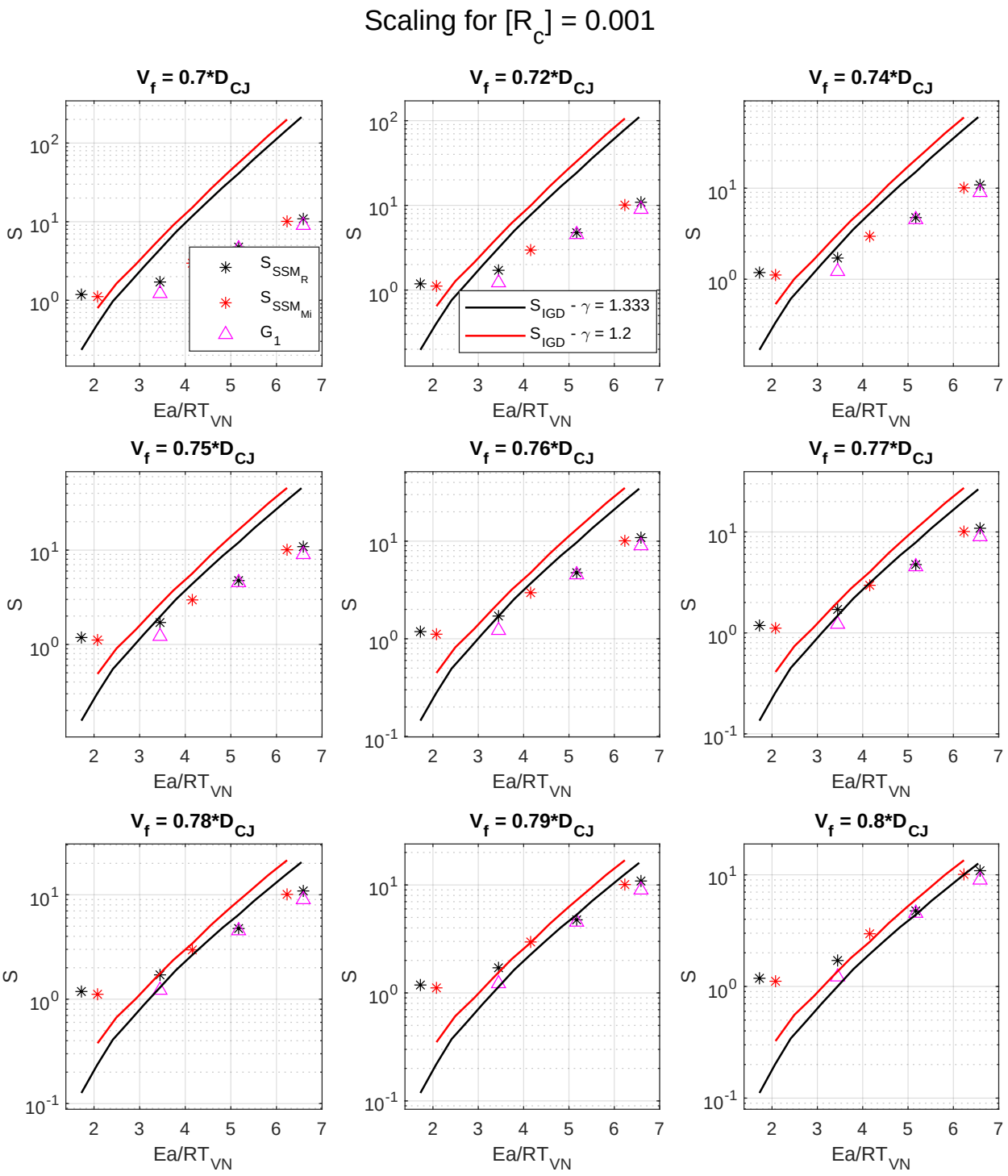

Figure B.2: Scaling of Reaction Zone Length for Ignition Delay Model on the assumption of reaction is complete at 0.1% of reactants.

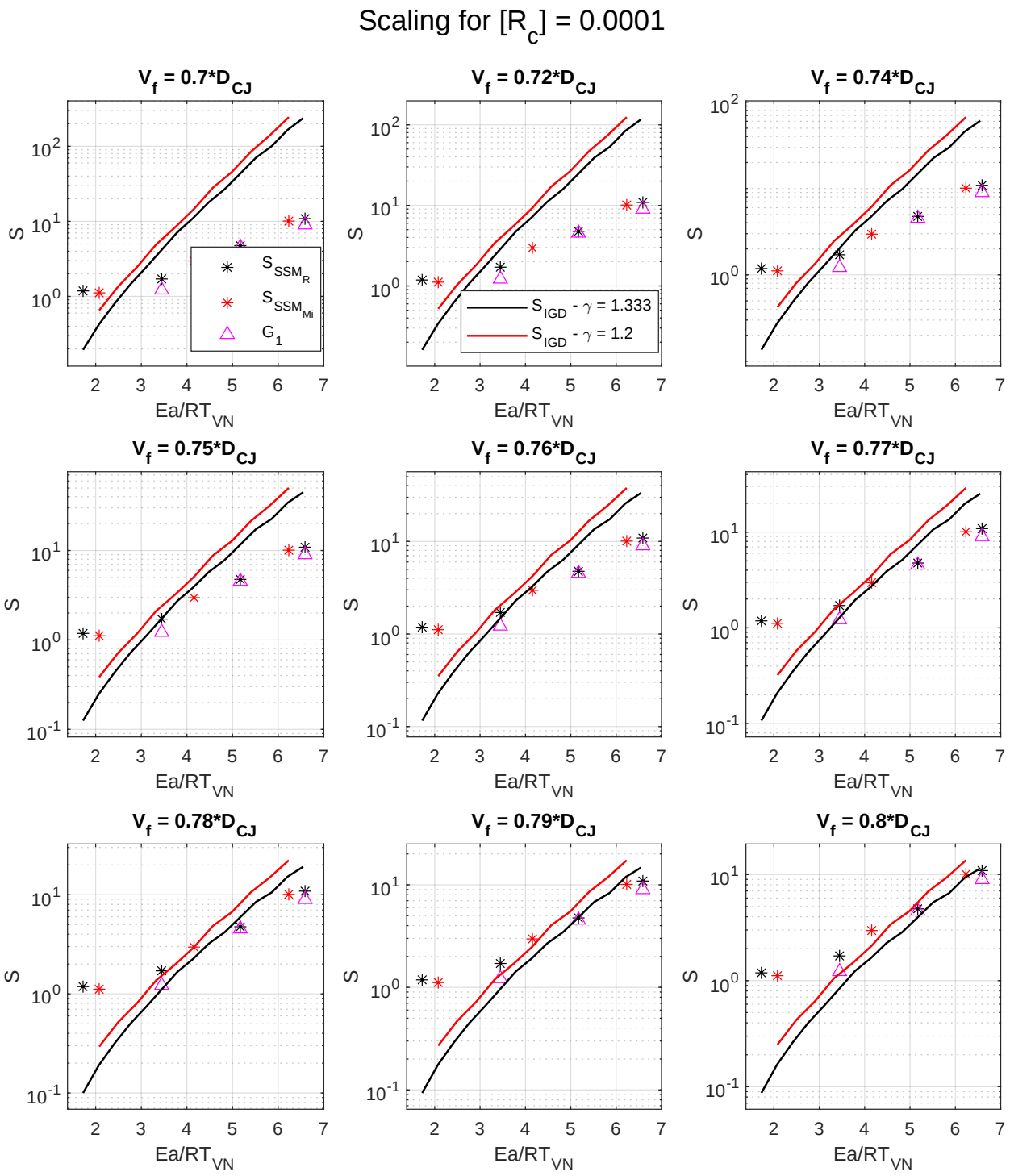

Figure B.3: Scaling of Reaction Zone Length for Ignition Delay Model on the assumption of reaction is complete at 0.01% of reactants.

References

[1] J H S Lee. *The detonation phenomenon*. 2008.

[2] Q Xiao and M I Radulescu. Dynamics of hydrogen–oxygen–argon cellular detonations with a constant mean lateral strain rate. *Combustion and Flame*, 215:437–457, 2020.

[3] M I Radulescu and B Borzou. Dynamics of detonations with a constant mean flow divergence. *Journal of Fluid Mechanics*, 845:346–377, 2018.

[4] J A Fay. Two-dimensional gaseous detonations: Velocity deficit. *The Physics of Fluids*, 2(3):283–289, 1959.

[5] Q Xiao, A Sow, B M Maxwell, and M I Radulescu. Effect of boundary layer losses on 2d detonation cellular structures. *Proceedings of the Combustion Institute*, 38(3):3641–3649, 2021.

[6] K Kawane, S Shimada, J Kasahara, and A Matsuo. The influence of heat transfer and friction on the impulse of a detonation tube. *Combustion and Flame*, 158(10):2023–2036, 2011.

[7] I Brailovsky and G Sivashinsky. Effects of momentum and heat losses on the multiplicity of detonation regimes. *Combustion and flame*, 128(1-2):191–196, 2002.

[8] M I Radulescu and J H S Lee. The failure mechanism of gaseous detonations: experiments in porous wall tubes. *Combustion and Flame*, 131(1-2):29–46, 2002.

[9] K Ishii, K Itoh, and T Tsuboi. A study on velocity deficits of detonation waves in narrow gaps. *Proceedings of the Combustion Institute*, 29(2):2789–2794, 2002.

[10] J E Shepherd. Detonation in gases. *Proceedings of the Combustion Institute*, 32(1):83–98, 2009.

[11] F K Lu and E M Braun. Rotating detonation wave propulsion: experimental challenges, modeling, and engine concepts. *Journal of Propulsion and Power*, 30(5):1125–1142, 2014.

[12] V Anand and E Gutmark. Rotating detonation combustors and their similarities to rocket instabilities. *Progress in Energy and Combustion Science*, 73:182–234, 2019.

[13] D Schwer and K Kailasanath. Numerical study of the effects of engine size n rotating detonation engines. In *49th AIAA aerospace sciences meeting including the new horizons forum and aerospace exposition*, page 581, 2011.

[14] K Kailasanath. Recent developments in the research on pulse detonation engines. *AIAA journal*, 41(2):145–159, 2003.

[15] K Wang and W Fan. Efforts on high-frequency pulse detonation engines. *Journal of Propulsion and Power*, 33(1):17–28, 2017.

[16] G D Roy, S M Frolov, D W Netzer, and A A Borisov. High-speed deflagration and detonation: Fundamentals and control. International Colloquium on Control and Detonation Processes Held in Moscow, Russia on July 4-7, 2000. Technical report, Elex-km Publishers Moscow (Russia), 2001.

[17] H Eyring, R E Powell, G H Duffy, and R B Parlin. The stability of detonation. *Chemical Reviews*, 45(1):69–181, 1949.

[18] W W Wood and J G Kirkwood. Diameter effect in condensed explosives. the relation between velocity and radius of curvature of the detonation wave. *The Journal of Chemical Physics*, 22(11):1920–1924, 1954.

[19] J B Bdzil and D S Stewart. Theory of detonation shock dynamics. In *Shock Waves Science and Technology Library, Vol. 6*, pages 373–453. Springer, 2012.

[20] J Li, X Mi, and A J Higgins. Geometric scaling for a detonation wave governed by a pressure-dependent reaction rate and yielding confinement. *Physics of Fluids*, 27(2):027102, 2015.

[21] W P Sommers and R B Morrison. Simulation of condensed-explosive detonation phenomena with gases. *The Physics of Fluids*, 5(2):241–248, 1962.

[22] S D Watt, G J Sharpe, S A E G Falle, and M Braithwaite. A streamline approach to two-dimensional steady non-ideal detonation: the straight streamline approximation. *Journal of Engineering Mathematics*, 75(1):1–14, 2012.

[23] M Reynaud, F Virot, and A Chinnayya. A computational study of the interaction of gaseous detonations with a compressible layer. *Physics of Fluids*, 29(5):056101, 2017.

[24] X C Mi, A J Higgins, C B Kiyanda, H D Ng, and N Nikiforakis. Effect of spatial inhomogeneities on detonation propagation with yielding confinement. *Shock Waves*, 28(5):993–1009, 2018.

[25] D L Chapman. Vi. on the rate of explosion in gases. *The London, Edinburgh, and Dublin Philosophical Magazine and Journal of Science*, 47(284):90–104, 1899.

[26] E Jouguet. Sur la propagation des réactions chimiques dans les gaz. *J. Maths. Pure Appl.*, 7:347, 1905.

[27] Y B Zeldovich. On the theory of the propagation of detonation in gaseous systems. *Zh. eksp. teoret. fiz.*, 10:542–568, 1940.

[28] J von Neumann. Progress report to the national defense research committee div. *B, OSRD-549*, 1942.

[29] W Döring. Über den detonationsvorgang in gasen. *Annalen der Physik*, 435(6-7):421–436, 1943.

[30] R A Strehlow, R E Maurer, and S Rajan. Transverse waves in detonations. i-spacing in the hydrogen-oxygensystem. *AIAA Journal*, 7(2):323–328, 1969.

[31] S Taki and T Fujiwara. Numerical analysis of two-dimensional nonsteady detonations. *Aiaa Journal*, 16(1):73–77, 1978.

[32] E S Oran, J W Weber Jr, E I Stefaniw, M H Lefebvre, and J D Anderson Jr. A numerical study of a two-dimensional H2-O2-Ar detonation using a detailed chemical reaction model. *Combustion and Flame*, 113(1-2):147–163, 1998.

[33] G J Sharpe. Transverse waves in numerical simulations of cellular detonations. *Journal of Fluid Mechanics*, 447:31–51, 2001.

[34] F Pintgen, C A Eckett, J M Austin, and J E Shepherd. Direct observations of reaction zone structure in propagating detonations. *Combustion and Flame*, 133(3):211–229, 2003.

[35] X Y Hu, B C Khoo, D L Zhang, and Z L Jiang. The cellular structure of a two-dimensional h2/o2/ar detonation wave. *Combustion Theory and Modelling*, 8(2):339, 2004.

[36] M I Radulescu, G J Sharpe, C K Law, and J H S Lee. The hydrodynamic structure of unstable cellular detonations. *Journal of Fluid Mechanics*, 580:31–81, 2007.

[37] B M Maxwell, R R Bhattacharjee, S S M Lau-Chapdelaine, S A E G Falle, G J Sharpe, and M I Radulescu. Influence of turbulent fluctuations on detonation propagation. *Journal of Fluid Mechanics*, 818:646–696, 2017.

[38] C B Kiyanda and A J Higgins. Photographic investigation into the mechanism of combustion in irregular detonation waves. *Shock Waves*, 23(2):115–130, 2013.

[39] E A Lundstrom and A K Oppenheim. On the influence of non-steadiness on the thickness of the detonation wave. *Proceedings of the Royal Society of London. A. Mathematical and Physical Sciences*, 310(1503):463–478, 1969.

[40] W P Sommers. *The interaction of a detonation wave with an inert boundary*. PhD thesis, 1961.

[41] E K Dabora, J A Nicholls, and R B Morrison. The influence of a compressible boundary on the propagation of gaseous detonations. In *Symposium (International) on Combustion*, volume 10, pages 817–830. Elsevier, 1965.

[42] E K Dabora. The influence of a compressible boundary on the propagation of gaseous detonations. rept. *No. TR-05170-1-T (AROD-3559-1), Univ. Mich*, 1963.

[43] T G Adams. Do weak detonation waves exist? *AIAA Journal*, 16(10):1035–1040, 1978.

[44] A A Vasil'ev. Critical diameter of gas-mixture detonation. *Combustion, Explosion and Shock Waves*, 18(3):349–355, 1982.

[45] A A Vasil'ev and D V Zak. Detonation of gas jets. *Combust., Explos. Shock Waves (Engl. Transl.);(United States)*, 22(4), 1987.

[46] M F Ivanov, V E Fortov, and A A Borisov. Numerical simulation of the development of a detonation in gas volumes of finite thickness. *Combustion, Explosion and Shock Waves*, 17(3):332–338, 1981.

[47] M F Ivanov, Y N Shebeko, and A Y Korol'chenko. Numerical modeling of the propagation of detonation in a gas layer of a detonating mixture diluted by nitrogen. *Combustion, Explosion and Shock Waves*, 20(2):233–236, 1984.

[48] R W Houim and R T Fievisohn. The influence of acoustic impedance on gaseous layered detonations bounded by an inert gas. *Combustion and Flame*, 179:185–198, 2017.

[49] C Chiquete, M Short, and J J Quirk. The effect of curvature and confinement on gas-phase detonation cellular stability. *Proceedings of the Combustion Institute*, 37(3):3565–3573, 2019.

[50] M Reynaud, S Taileb, and A Chinnayya. Computation of the mean hydrodynamic structure of gaseous detonations with losses. *Shock Waves*, 30(6):645–669, 2020.

[51] M Cartwright. *Modelling of non-ideal steady detonations*. PhD thesis, University of Leeds, 2016.

[52] J B Bdzil. Steady-state two-dimensional detonation. *Journal of Fluid Mechanics*, 108:195–226, 1981.

[53] G J Sharpe and J B Bdzil. Interactions of inert confiners with explosives. *Journal of engineering mathematics*, 54(3):273–298, 2006.

[54] K Cheevers and M Radulescu. Ignition behind decaying shock waves: Detonation cells. *arXiv preprint arXiv:2211.05216*, 2022.

[55] W Fickett and W Davis. Detonation: theory and experiment. 2000.

[56] F A Williams. *Combustion theory*. CRC Press, 2018.

[57] M I Radulescu, G J Sharpe, J H S Lee, C B Kiyanda, A J Higgins, and R K Hanson. The ignition mechanism in irregular structure gaseous detonations. *Proceedings of the Combustion Institute*, 30(2):1859–1867, 2005.

[58] M Cartwright and S A E G Falle. Numerical modelling of steady detonations with a variational streamline approach. *Journal of Engineering Mathematics*, 129(1):1–19, 2021.